^{75}As and ^{59}Co NMR STUDY of the ELECTRON DOPED $Ba(Fe_{1-x}Co_x)_2As_2$

^{75}As and ^{59}Co NMR STUDY of the ELECTRON DOPED $Ba(Fe_{1-x}Co_x)_2As_2$

By

FANLONG NING, M. Sc.

A Thesis
Submitted to the School of Graduate Studies
in Partial Fulfilment of the Requirements
for the Degree
Doctor of Philosophy

McMaster University

DOCTOR OF PHILOSOPHY (2009)	McMaster University
(Physics and Astronomy)	Hamilton, Ontario

TITLE:	^{75}As and ^{59}Co NMR STUDY of the ELECTRON DOPED Ba(Fe$_{1-x}$Co$_x$)$_2$As$_2$
AUTHOR:	Fanlong Ning B. Sc., 2000 (Jilin University, China) M. Sc., 2003 (Jilin University, China) M. Sc., 2005 (McMaster University, Canada) Hamilton, Canada, 2009
SUPERVISOR:	Prof. Takashi Imai
NUMBER OF PAGES:	xv, 116

Abstract

We report a systematic investigation of the local electronic, magnetic, and superconducting properties of the new iron-based high temperature superconductor $Ba(Fe_{1-x}Co_x)_2As_2$ (x = 0, 0.02, 0.04, 0.082) through the measurement of ^{75}As and ^{59}Co NMR (Nuclear Magnetic Resonance) lineshapes, Knight shift (K), and spin-lattice relaxation rate ($1/T_1$). The ^{75}As NMR lineshape of the undoped parent compound splits into two sets due to discrete values of hyperfine magnetic field $B^c_{hf} = \pm$ 1.32 Tesla below the magnetic ordering temperature to the SDW (Spin Density Wave) state, T_{SDW}. In contrast, for lightly Co doped samples with $x = 0.02$ and 0.04, the ^{75}As and ^{59}Co lineshapes become broad and featureless below T_{SDW}, indicating that the ground state is no longer the commensurate SDW ordered state. The observed lineshape is consistent with an incommensurate SDW ordered state, or a commensurate state with large distribution of hyperfine field B_{hf}. In the optimally doped superconductor with $x = 0.082$ (T_c = 22 K), we observe two types of As sites and three types of Co sites, respectively, as expected from a binomial distribution of Co dopants. We found no evidence for induced localized moments in the vicinity of Co dopants. This finding is in remarkable contrast with the case of Zn or Ni doped high T_c cuprates, and suggests that the fundamental physics of iron-based superconductors is different from that of cuprates. The temperature dependences of $^{75,59}K$ and $^{75,59}(1/T_1T)$ at both ^{75}As and ^{59}Co sites show that $Ba(Fe_{1-x}Co_x)_2As_2$ exhibits spin pseudo-gap like behavior down to $\sim$ 100 K for a broad Co concentration range. Below $\sim$ 100 K, we observe the enhancement of residual antiferromagnetic spin fluctuations associated with inter-band spin excitations between the hole and electron Fermi surfaces even for $x = 0.082$. This effect is suppressed in the overdoped sample with x

= 0.099, and T_c decreases. Therefore, we suggest that antiferromagnetic spin fluctuations play a crucial role in the superconducting mechanism of $\mathrm{Ba(Fe_{1-x}Co_x)_2As_2}$. We also demonstrate that the superconductivity arises from a novel electronic state with spin susceptibility $\chi_s \sim$ constant and in-plane resistivity $\rho_{ab} \sim$ T, which is not consistent with canonical Fermi-liquid behavior.

Acknowledgements

I would like to give special thanks to my thesis supervisor, Prof. Takashi Imai, for his guidance, support and patience over the past five and half years. Takashi is the person who brought me into real academic research, and pushed me deep into the world of physics. His presence in the lab always gave me confidence and encouragement for continuing some challenging experiments. He taught me the value of hard work during late nights and weekends when we were working together through his own example, which helped to make my years as a graduate student fruitful and meaningful. In academic, his high research standards helped to make my work recognized by the community. When I was working on my thesis, he helped me enormously by reading a number of my drafts and providing me with immediate and valuable feedback.

I want to thank Dr. Athena Sefat and her colleagues at Oak Ridge National Laboratory. They provided us with high quality $Ba(Fe_{1-x}Co_x)_2As_2$ single crystals, which made my research and thesis possible. Thanks also go to Dr. Fangcheng Chou at M.I.T., who provided us with Na_xCoO_2 single crystals in the early stage of my Ph.D study.

I also want to thank Prof. An-Chang Shi and Prof. Graeme Luke who are in my supervisory committee, for their time and suggestions. Thanks also go to my labmates, Dr. Kanagasingham Ahilan, Dr. Shanta Ranjan Saha, Ms. Sarah Golin and Mr. Matthew Van Dyken for their collaborations. I also appreciated help from Dr. Paul Dube, who provided us with enough helium for experiments.

Many thanks go to the people working in the general office, Ms. Daphne Kilgour, Ms. Mara Esposto, Ms. Cheryl Johnston and Ms. Liz Penney who helped me

so many times for all kinds of administrative things. Their assistance made my life in Canada much easier.

I also want to thank my friends in the physics department, Zhou Jiajia, Zhao Yang, Pat Clancy, Jacob Ruff, Adam Aczel, Dr. Jungseek Hwang, Yang Jing, Chen Jun, Ran Wenqi, Wu Meng, Jose Rodriguez, Travis Williams, Katharina Fritsch and Kathryn Ross, among others. In particular, I would like to thank Pat Clancy and Adam Aczel, who proofread our manuscripts many times, and helped us correct typos and grammatical errors before we proceeded to submit the works to journals. All in all, I was so lucky to work with such a great group of people at McMaster.

Last but not least, I would like to thank my wife Zhou Yi and all my family members for their love, care, support and encouragement to me all along my Ph.D journey.

Hamilton, Ontario
August, 2009 Fanlong Ning

Publications

1, T. Aharen, J.E. Greedan, **F.L. Ning**, T. Imai, V. Michaelis, S. Kroeker, H.D. Zhou, C.R. Wiebe and L. Cranswick. *Magnetic Properties of S = 3/2 Geometrically Frustrated Double Perovskites, La2LiRuO6 and Ba2YRuO6*, Physical Review B 80, 134423 (2009).

2, **F.L. Ning**, K. Ahilan, T. Imai, A.S. Sefat, M.A. McGuire, B.C. Sales, D. Mandrus, P. Cheng, B. Shen and H.-H. Wen. *Contrasting Spin Dynamics Between Underdoped and Overdoped* $Ba(Fe_{1-x}Co_x)_2As_2$, Physical Review Letters (submitted).

3, K. Ahilan, **F.L. Ning**, T. Imai, A.S. Sefat, R. Jin, M.A. McGuire, B.C. Sales and D. Mandrus. *The Electronic Phase Diagram of the Iron-based High Tc Superconductor* $Ba(Fe_{1-x}Co_x)_2As_2$ *Under Hydrostatic Pressure* $(0 < x < 0.099)$, Physical Review B 79, 214520 (2009).

4, **F.L. Ning**, K. Ahilan, T. Imai, A.S. Sefat, R. Jin, M.A. McGuire, B.C. Sales and D. Mandrus. ^{75}*As NMR Observation of Anisotropic Spin Fluctuations in the* $Ba(Fe_{0.92}Co_{0.08})_2As_2$ *Superconductor* $(T_c = 22\ K)$, Journal of the Physical Society of Japan (submitted).

5, T. Imai, K. Ahilan, **F.L. Ning**, T.M. McQueen and R.J. Cava. *Why Does Undoped FeSe Become A High* T_c *Superconductor Under Pressure?*, Physical Review Letters 102, 177005 (2009).

6, **F.L. Ning**, K. Ahilan, T. Imai, A.S. Sefat, R. Jin, M.A. McGuire, B.C. Sales and D. Mandrus. ^{59}*Co NMR and* ^{75}*As Investigation of Lightly Doped* $Ba(Fe_{1-x}Co_x)_2As_2$ $(x = 0.02, 0.04)$, Physical Review B 79, 140506(R) (2009).

7, **F.L. Ning**, K. Ahilan, T. Imai, A.S. Sefat, R. Jin, M.A. McGuire, B.C. Sales and D. Mandrus. *Spin Susceptibility, Phase Diagram, and Quantum Criticality in Electron-Doped High* T_c *Superconductor* $Ba(Fe_{1-x}Co_x)_2As_2$, Journal of the Physical Society of Japan 78, 013711 (2009). **Note: this paper is**

featured in Physics Today, August, 36 (2009).

8, K. Ahilan, J. Balasubramaniam, **F.L. Ning**, T. Imai, A.S. Sefat, R. Jin, M.A. McGuire, B.C. Sales and D. Mandrus. *High pressure effects on the electron-doped high* T_c *superconductor* $BaFe_{2-x}Co_xAs_2$, Journal of Physics: Condensed Matter 20, 472201 (2008).

9, T. Imai, K. Ahilan, **F.L. Ning**, M.A. McGuire, A.S. Sefat, R. Jin, B.C. Sales and D. Mandrus. *NMR investigation of intrinsic spin susceptibility in* $LaFeAsO_{0.9}F_{0.1}$, Invited paper to the Proceedings of the International Symposium on Iron-oxypnictide Superconductors, Journal of the Physical Society of Japan 77, Supplement C, p47-53 (2008).

10, **F.L. Ning**, K. Ahilan, T. Imai, A.S. Sefat, R. Jin, M.A. McGuire, B.C. Sales and D. Mandrus. ^{59}*Co and* ^{75}*As NMR investigation of electron-doped high Tc superconductor* $BaFe_{1.8}Co_{0.2}As_2$ *(*T_c *= 22K)*, Journal of the Physical Society of Japan 77, 103705 (2008). **Note: this paper has been chosen as "Papers of Editors' Choice" for the year of 2008**.

11, K. Ahilan, **F.L. Ning**, T. Imai, A.S. Sefat, R. Jin, M.A. McGuire, B.C. Sales and D. Mandrus. ^{19}*F NMR investigation of the iron-pnictide superconductor* $LaFeAsO_{0.89}F_{0.11}$, Physical Review B 78, 100501(R) (2008).

12, **F.L. Ning**, S. Golin, K. Ahilan, G.J. Shu and F.C. Chou. ^{59}*Co NMR evidence for charge ordering below* $T_{CO}$$\sim$*51K in* $Na_{0.5}CoO_2$, Physical Review Letters 100, 086405 (2008).

13, **F.L. Ning**, and T. Imai. ^{17}*O NMR Studies of a Triangular-Lattice Superconductor* Na_xCoO_2- yH_2O, Physical Review Letters 94, 227204 (2005).

14, **F.L. Ning**, T. Imai, B.W. Statt, and F.C. Chou. *Spin dynamics in the carrier-doped S = 1/2 triangular lattice of* Na_xCoO_2- yH_2O, Physical Review Letters 93, 237201 (2004).

Contents

List of Figures

List of Tables

Chapter 1

INTRODUCTION

1.1 Discovery of Iron-Based High T_c Superconductors

Research on the mechanism of high transition temperature (high-T_c) superconductivity has been an important topic in condensed matter physics for more than 20 years since the initial discovery of the high-T_c copper oxide superconductor $La_{2-x}Ba_xCuO_4$ in 1986 (Bednorz and Müller, 1986). Many cuprates show a very high transition temperature compared with conventional metal or alloy superconductors which can be described well by the Bardeen-Cooper-Schrieffer (BCS) theory (Bardeen et al., 1957). Over the past 23 years, considerable progress has been made in understanding the physical properties of the CuO_2 planes of high T_c cuprates where the high T_c superconductivity takes place. However, existing theoretical models still face difficulties in explaining the mechanism of high T_c superconductivity in part because it is inherently difficult to describe the many-body physics of strongly correlated electrons in the CuO_2 plane. Persistent efforts are underway to advance our understanding of both theoretical and experimental aspects of cuprates.

One line of research is to search for new types of superconductors, which may share common aspects with the cuprates, and hence provide valuable clues for understanding the high T_c superconducting mechanism. Over the past 22 years, many new families of unusual superconductors were discovered, including Sr_2RuO_4 ($T_c = 1.5$ K) (Maeno et al., 1994), MgB_2 ($T_c = 39$ K) (Nagamatsu et al., 2001), $Na_xCoO_2 - yH_2O$ ($T_c \sim 5$ K) (Takada et al., 2003) and $PuCoGa_5$ ($T_c = 18.5$ K) (Sarrao et al., 2002). Each of these systems shares some similarities with the high T_c cuprates. For example, both Sr_2RuO_4 and $Na_xCoO_2 - yH_2O$ have layered structures, and the electronic properties are nearly two dimensional and anisotropic; both Ru and Co are transition metals, and electrons in d orbitals play important roles in their physical properties. Furthermore, some theoretical models (Baskaran, 2003) consider the ground state of the parent compound CoO_2 of $Na_xCoO_2- yH_2O$ as a Mott insulator; doping electrons through substitution of Na^+ ions into CoO_2 induces superconductivity. This is very similar to the high T_c superconductivity in cuprates, which is achieved by doping either electrons or holes into the parent Mott insulators through, e.g. doping Sr^{2+} into La^{3+} sites in La_2CuO_4. On the other hand, MgB_2 has a rather high transition temperature, $T_c = 39$ K, yet the conventional Cooper pairing by phonons is believed to account for the superconducting mechanism (Singer et al., 2001). Through persistent studies on these novel superconductors, it has become clear that these systems have their own unique properties and interesting underlying physics, yet none of them may provide very decisive clues to pinpoint the superconducting mechanism of the high-T_c cuprates. Until very recently, the cuprate monopoly in the physics of high T_c superconductors had not been broken.

The endeavor to search for new superconductors recently led to the discovery of new Fe-based superconductors by Hosono and co-workers at the Tokyo Institute of

Technology. In February 2008, they reported in the Journal of the American Chemical Society (JACS) that an oxypnictide, $LaO_{1-x}F_xFeAs$, exhibits superconductivity with T_c as high as 26 K (Kamihara et al., 2008). Their discovery caused an instant worldwide sensation. Within a month, Chen's group at the University of Science and Technology of China raised T_c to $\sim$ 43 K in $SmO_{1-x}F_xFeAs$ by replacing La^{3+} with Sm^{3+} (Chen et al., 2008). Three days later, Zhao's group in the Chinese Academy of Science reported that they found $PrO_{1-x}F_xFeAs$ with $T_c = 52$ K (Ren et al., 2008c). Within a few weeks, they also discovered that the highest $T_c = 55$ K of this class of superconuductors can be achieved for $SmO_{1-x}F_xFeAs$ under high pressure (Ren et al., 2008a). This was the birth of a new family of Fe-based high T_c superconductors, and the monopoly of high T_c cuprates has been broken down.

The global competition on investigation into Fe-based superconductors immediately ensued. Hundreds of publications appeared in less than one year. Many new Fe-based superconductors in combination with different elements were discovered. The superconductors can be obtained by doping either electrons or holes, or even isovalent phosphorous into the parent compounds. More interestingly, doping transition metals such as Co, Ni, Ru, Rh, Pd, Ir etc. into the FeAs layers can also induce superconductivity; this is in remarkable contrast with the widely known phenomena in high T_c cuprates, in which transition metal atoms doped into the CuO_2 plane are detrimental to the superconductivity (Fukuzumi et al., 1996). As of today, the highest record of T_c is $\sim$ 57.3 K in $Ca_{1-x}Nd_xFFeAs$ (Cheng et al., 2009), exceeding the previous records of 55 K in $SmO_{1-x}F_xFeAs$ (Ren et al., 2008a,b) and 56.3 K in $Gd_{1-x}Th_xOFeAs$ (Wang et al., 2008).

Depending on the crystal structure and the number of elements in one unit cell, scientists commonly group all these homologous superconductors into five systems: they are 1111 (i.e. LaOFeAs), 122 (i.e. $BaFe_2As_2$), 111 (i.e. LiFeAs), 11 (i.e. FeSe) and 42622 (i.e. $Sr_4Sc_2O_6Fe_2P_2$) systems. In the following, I will briefly introduce and summarize the key physical properties of the Fe-based high T_c superconductors with primary focus on the 122 compound $Ba(Fe_{1-x}Co_x)_2As_2$ as a representative example.

1.2 Basic Physical Properties of $Ba(Fe_{1-x}Co_x)_2As_2$

1.2.1 Layered Crystal Structure of $Ba(Fe_{1-x}Co_x)_2As_2$

The parent compound $BaFe_2As_2$ ($x = 0$) has a tetragonal $ThCr_2Si_2$ structure with space group I4/mmm at room temperature (Rotter et al., 2008), as shown in Fig. 1.1 (Huang et al., 2008). Fe atoms form a square-lattice, and each Fe atom is coordinated by four As atoms to form a $FeAs_4$ tetrahedra. The FeAs layers are separated by Ba layers along the c-axis within the layered structure. The lattice constants are $a = b = 3.9625(1)$Å and $c = 13.0168(3)$ Å at room temperature. Below $T_S \sim 135$ K, the tetragonal structure transforms to an orthorhombic phase, and the unit cell doubles (Rotter et al., 2008).

The FeAs layers are the crucial components responsible for the rich physical properties of $BaFe_2As_2$ and other Fe-based superconductors (Singh and Du, 2008). In a close inspection of the FeAs layer, we find that As atoms are located perpendicularly above or underneath the center of the square-lattice formed by Fe atoms alternatively along the crystal a and b-axis. We show a single FeAs unit in Fig. 1.2, and define the As atom underneath (above) the Fe-plane as As1 (As2). The bond angles for As1-Fe-As1 and As1-Fe-As2 are 108.7° and 111.1°, respectively. We tabulate the crystallographic data at T = 297 K and 20 K in Table. 1.1. We note that the lattice constants a and b change by a factor of $\sim \sqrt{2}$ between 297 K and 20 K, simply because the unit cell is doubled in the orthorhombic structure; the bond lengths and the bond angles change

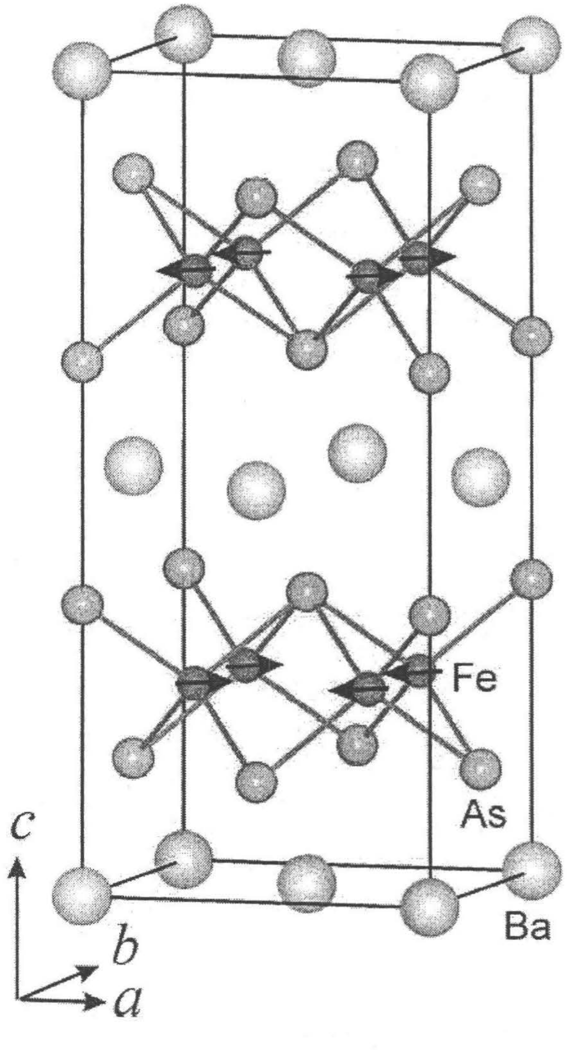

Figure 1.1 Magnetic and crystal structures of $BaFe_2As_2$ (Huang et al., 2008). Arrows indicate the orientation of magnetic moments at Fe sites below the SDW (Spin Density Wave) ordering temperature.

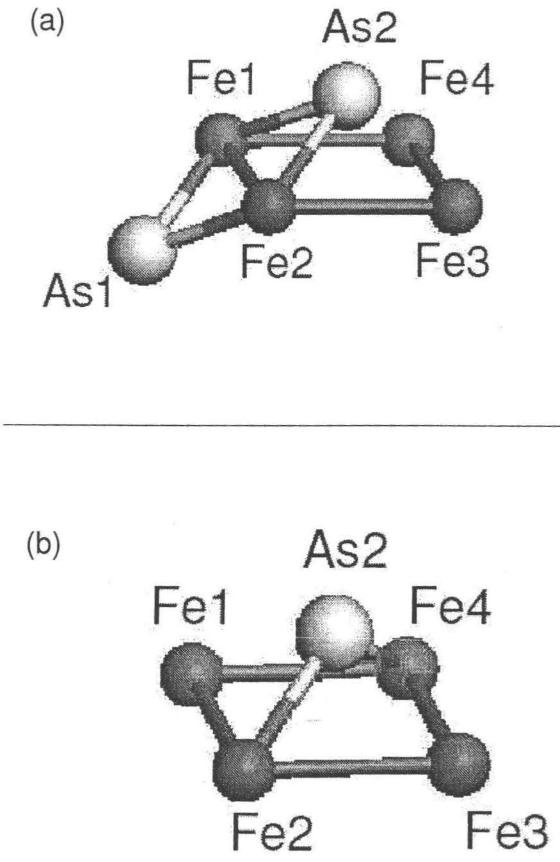

Figure 1.2 Single FeAs unit in Ba$(Fe_{1-x}Co_x)_2As_2$ adapted from reference (Yildirim, 2008). As atoms are located perpendicularly underneath (As1) or above (As2) the center of the square-lattice formed by Fe atoms alternatively along the crystalline a and b-axis. Note that in (a), As1-Fe1-As2-Fe2 forms a parallelogram, which intercepts with the Fe1-Fe2-Fe3-Fe4 plane.

Table 1.1 Crystallographic data for $Ba(Fe_1)_2As_2$ (Rotter et al., 2008).

	297 K	20 K
a (Å)	3.9625(1)	5.6146
b (Å)	3.9625(1)	5.5742
c (Å)	13.0168(3)	12.9453
V (Å^3)	204.38(1)	405.14(2)
Atomic site	(x,y,z)	(x,y,z)
Ba	2a(0,0,0)	4a(0,0,0)
Fe	4d($\frac{1}{2}$,0,$\frac{1}{8}$)	8f($\frac{1}{4}$,$\frac{1}{4}$,$\frac{1}{4}$)
As	4e(0,0,3.545)	8i(0,0,3.538)
Bond lengths (Å)	$l \times$ number of coordinates	$l \times$ number of coordinates
Ba-As	3.382(1)×8	3.3691×4, 3.385(1)×4
Fe-As	2.403(1)×4	2.3921(1)×4
Fe-Fe	2.802(1)×4	2.8071(1)×2, 2.787(1)×2
Bond angles(°)	$\theta \times$ number of coordinates	$\theta \times$ number of coordinates
As1–Fe–As1	108.7(1)×4	108.7(1)×2,108.1(1)×2
As1–Fe–As2	111.1(1)×2	111.6(1)×2

very little.

When we dope Co atoms into the FeAs layers, Co atoms randomly replace Fe atoms, and suppress the structural transition temperature, T_S, progressively with increasing Co doping. When the Co concentration reaches $x \sim 0.06$, the structural transition is completely suppressed, and the $Ba(Fe_{1-x}Co_x)_2As_2$ compound has only the tetragonal phase below 300 K for $x \gtrsim 0.06$ (Chu et al., 2009). In the tetragonal phase, the c-axis lattice constant decreases strongly with increasing Co concentration, while the a-axis lattice constant decreases only slightly (Wang et al., 2009b).

1.2.2 Fe 3d Electron Levels

The electronic configuration for neutral Ba, Fe, and As atom is [Xe]$(6s)^2$, [Ar]$(3d)^6(4s)^2$ and [Ar]$(3d)^{10}(4s)^2(4p)^3$, respectively. We expect the ionic valence is Ba^{2+} in the parent compound $BaFe_2As_2$. Since the ionic valence for all ions should sum up to zero, the ionic state of FeAs layers should be $[FeAs]^-$ in $BaFe_2As_2$. This implies that each Ba and Fe atom donates one (6s) and two (4s) electrons respectively to fill the 4p orbitals of each As atom, to form an $[Fe^{2+}As^{3-}]$ state. Thus 6 electrons remain in the Fe 3d orbitals. Furthermore, since Fe ions are tetrahedrally-coordinated with As^{3-} ions, the crystal field at a given Fe site will lift the degeneracy of electron levels, and splits the 3d orbitals into e and t_2 states. By taking into account the Coulomb interaction U (~4-5 eV), and the Hund's coupling (~0.7 eV), Si and Abrahams present one possible orbital occupation scheme of the Fe 3d levels, as shown in Fig. 1.3 (Si and Abrahams, 2008, Jishi and Alyahyaei, 2008). In this scheme, two electrons with

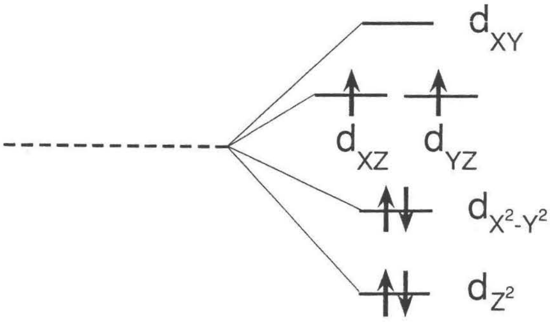

Figure 1.3 One possible electrons occupation scheme in 3d orbitals of Fe^{2+} ions in a tetrahedral crystal field (Si and Abrahams, 2008, Jishi and Alyahyaei, 2008).

antiparallel spin occupy $d_{X^2-Y^2}$ and d_{Z^2} orbital, and a single electron occupies the d_{XZ} and d_{YZ} orbital, but no electrons are in the d_{XY} orbital. If all electrons are localized, we would expect the total spin $S = 1$, and therefore the magnitude of the ordered Fe magnetic moment, μ, is 2 μ_B. However, neutron diffraction measurements (Huang et al., 2008) indicate that μ is as small as ~ 0.87 μ_B in the parent compound. The disagreement suggests that such a simple local moment picture fails and the electrons are more itinerant, and the five 3d orbitals are heavily mixed with each other as the theoretical calculations suggested (Aoki, 2008).

1.2.3 Fermi Surface and Its Modification with Co Doping

Local density approximation (LDA) calculations for the parent compound $BaFe_2As_2$ predict that the Fe 3d orbitals contribute the most to the density of states (DOS) at the Fermi surface, and there are five sheets of Fermi surface (Singh, 2008, Shein and Ivanovskii, 2008, Ma et al., 2008, Nekrasov et al., 2008). These five sheets include three concentric hole pockets centered around the Γ point ($(k_x, k_y) = (0, 0)$) in the folded first Brillouin zone (B.Z.), and two electron pockets centered around the X point at the zone corners ($(k_x, k_y) = (\pi/a, \pi/a)$), as shown in Fig. 1.4. These calculations also demonstrate that the hole pockets have mainly d_{XZ} and d_{YZ} characters, while the electron pockets have mainly $d_{X^2-Y^2}$ character (Aoki, 2008).

The direct measurements of the Fermi surface of the parent compound $BaFe_2As_2$ by ARPES (angle-resolved photoemission spectroscopy) have been reported by many groups (Yi et al., 2009, Yang et al., 2009, Liu et al., 2009b, Terashima et al., 2008, Sekiba et al., 2009, Malaeb et al., 2009). They observed the hole (electron) pockets at the center (corner) of the B.Z., which are qualitatively similar to what LDA calculations predicted. In addition, they also demonstrated that the modulation of dispersion along the k_z direction is weak for the cylindrical electron pockets around the X point than the hole pockets around the Γ point, i.e., the Fermi surface around the Γ point exhibits three dimensionality (Vilmercati et al., 2009, Liu et al., 2009a, Malaeb et al., 2009). This finding is consistent with the weak anisotropy of the upper critical field H_{c2} in the superconducting samples $Ba(Fe_{0.926}Co_{0.074})_2As_2$ (Tanatar et al., 2009) and $Ba(Fe_{0.92}Co_{0.08})_2As_2$ (Kano et al., 2009).

In the case of $Ba(Fe_{1-x}Co_x)_2As_2$, each Co^{2+} ion doped into an FeAs layer adds an extra electron into a Fe 3d orbital, i.e. electron doping. A natural expectation is that doped electrons would modify the Fermi surfaces; the hole pockets shrink while the electron pockets expand. In fact, ARPES measurements do observe such doping effects on Fermi surfaces. They showed that the hole pockets at the zone center become smaller with electron doping (Yi et al., 2009, Malaeb et al., 2009), and nearly disappear for a heavily electron-doped sample with $x = 0.15$ (Sekiba et al., 2009). On the other hand, the change of electron pockets at the X point with Co doping is very complex and more dramatic due to complicated hybridization of many bands at the zone corner. The anisotropic Fermi surfaces within the k_x and k_y plane in the parent compound become nearly circular with Co doping $x \sim 0.07$ (Malaeb et al., 2009).

1.2.4 Commensurate SDW – Ground State of $BaFe_2As_2$

Arrows in Fig. 1.1 represent the orientation of the ordered magnetic moment μ in the parent compound $BaFe_2As_2$ as determined by neutron powder diffraction. The magnetically ordered ground state has been suggested as SDW (Spin Density Wave) ordered (Dong et al., 2008, de la Cruz et al., 2008), which arises from the nesting of the Fermi surfaces of the hole pockets and electron pockets separated by a wave vector $\vec{Q} = (\pi/a, 0)$ or $(0, \pi/a)$ as marked by arrows in Fig. 1.4(b), and the interaction between electrons. The ordered ground state of $BaFe_2As_2$ has itinerant electrons, and the in-plane resistivity remains finite below $T_{SDW} \sim 135$ K (Rotter et al., 2008). The

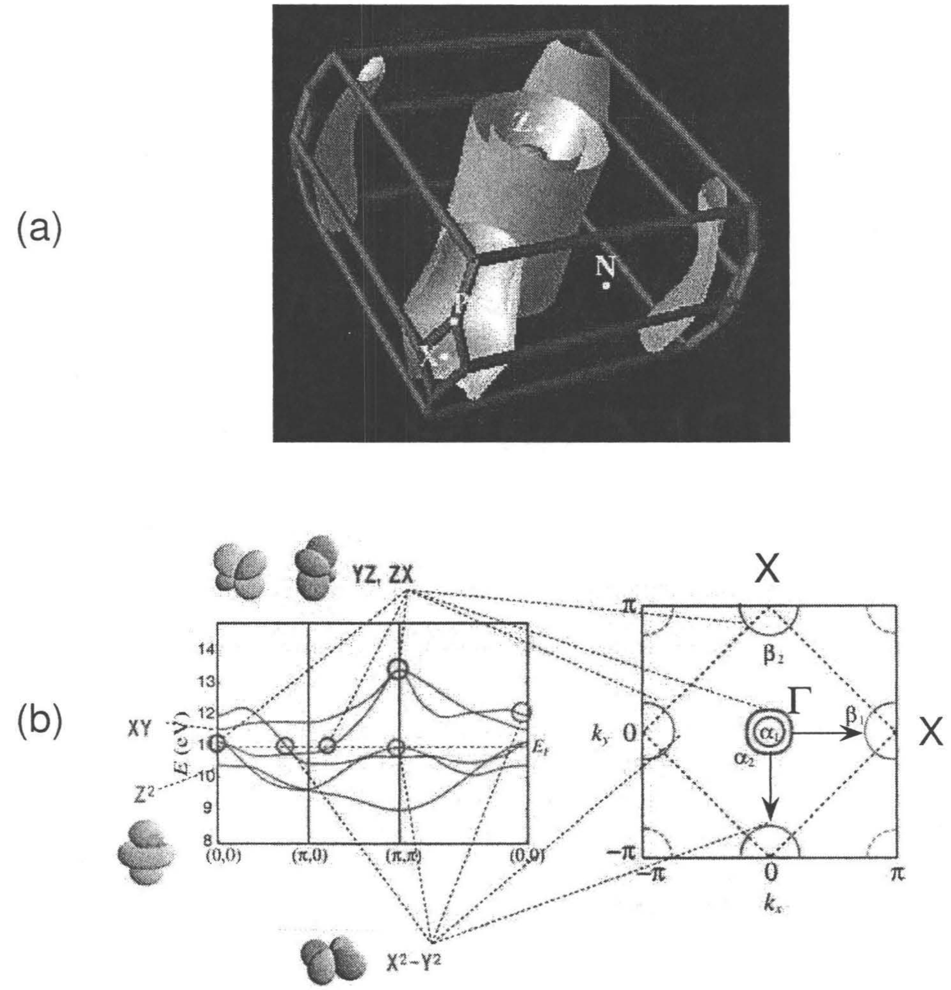

Figure 1.4 (a) LDA calculated Fermi surface of $BaFe_2As_2$ in the folded first Brillouin zone centered at Γ point (Nekrasov et al., 2008). (b) The band structure of $BaFe_2As_2$ in the unfolded B.Z. (left panel). A top view of the Fermi surface (right panel), with the folded (dashed line, same as in (a)) and the unfolded (solid) B.Z.. Orbital character is indicated for the bands and Fermi surfaces. Arrows depict nesting vectors (π/a, 0) and (0, π/a) which induce the commensurate SDW (Aoki, 2008).

ordered magnetic moments are within the *ab*-plane, and the magnitude is estimated to be $\sim 0.87\ \mu_B$ (Huang et al., 2008). No moments are detected along the crystalline *c*-axis. The ferromagnetic rows of Fe magnetic moments are along the shorter *b*-axis, and these rows of Fe moments align antiferromagnetically along the longer *a*-axis, as well as along the *c*-axis. The commensurate SDW ground state is the common feature shared by all the parent compounds of the FeAs-based systems, such as the well studied LaFeOAs (de la Cruz et al., 2008) and $SrFe_2As_2$ (Jesche et al., 2008).

The commensurate SDW ground state of $BaFe_2As_2$ was also confirmed by a ^{75}As NMR lineshape measurement on a single crystal (Kitagawa et al., 2008). They showed that the hyperfine field B^c_{hf} at ^{75}As sites $\sim \pm 1.4$ Tesla at 4.2 K. The well defined, discrete values of B^c_{hf} are characteristic of a commensurate SDW state. Furthermore, they showed that the spin-lattice relaxation rate, $1/T_1T \sim 0.04\ \text{sec}^{-1}\text{K}^{-1}$ at ^{75}As site, is constant and finite near 4.2 K. This Korringa behavior indicates that some electrons of $BaFe_2As_2$ are itinerant even at 4.2 K as explained in section 2.4.

1.3 Why Do We Investigate $Ba(Fe_{1-x}Co_x)_2As_2$ with NMR?

Soon after the discovery of Fe-based superconductors, our group quickly started microscopic investigation of them by NMR, and made significant contributions to the development of the research field through the investigation of $LaO_{0.9}F_{0.1}FeAs$ (Ahilan et al., 2008b, Imai et al., 2008), $Ba(Fe_{1-x}Co_x)_2As_2$ (Ning et al., 2008, 2009a,b,c, Ahilan et al., 2008a, 2009), and β-FeSe (Imai et al., 2009). In this thesis, we will mainly focus our attention on the results of $Ba(Fe_{1-x}Co_x)_2As_2$, since this system has many advantages over other systems: (1) Sizable single crystals became available soon after the discovery of superconductivity in the 122 system. (2) The compounds are synthesized in ambient pressure, and the homogeneity of the crystals is much better than the fluorine doped 1111 system and the potassium doped 122 system. (3) The Co doping concentration is relatively easy to control, and one can calibrate the actual concentration by EDS (Energy Dispersive X-ray spectroscopy). (4) Transition metals such as Co and Ni doped into FeAs layers induce superconductivity in Fe-based systems. This is in contrary to the widely known phenomenon in high T_c cuprates, in which transition metal atoms doped into CuO_2 plane are detrimental to the superconductivity (Fukuzumi et al., 1996). Understanding the physics of $Ba(Fe_{1-x}Co_x)_2As_2$ may provide some key clues for the superconducting mechanism in Fe-based superconductors. (5) We can probe the electronic properties in $Ba(Fe_{1-x}Co_x)_2As_2$ through both ^{75}As and ^{59}Co NMR. In the case of 1111 or 11 systems, ^{57}Fe isotope enrichment is necessary to probe the Fe layers directly. In our case, ^{59}Co NMR allow us to probe the $(Fe_{1-x}Co_x)$ layers directly.

1.4 Samples

1.4.1 Sample Preparation

All single crystals used in this thesis were grown by Dr. Athena Sefat and her collaborators in Oak Ridge National Laboratory. They were the first in the world to discover that doping Co into LaOFeAs (Sefat et al., 2008a) and $BaFe_2As_2$ (Sefat et al., 2008b) induces superconductivity. They grew all single crystals using FeAs flux to avoid contamination by flux residues. We note that crystals grown in Sn flux in early stages were contaminated by ~ 1 % Sn impurity, which significantly affect the physical properties (Baek et al., 2008, Kitagawa et al., 2008). All starting elements are from Alfa Aesar and of high purity (> 99.9 %). They first placed mixtures of As, Co powder and/or Fe piece in a silica tube, and then slowly heated the mixture up to 700 °C for 6 hours to prepare FeAs or CoAs binaries. The mixtures were further annealed at 1065 °C for 10 hours. For the $BaFe_2As_2$ crystal, a ratio of Ba:FeAs = 1:5 was heated at 1180 °C for 8 hours under an argon atmosphere. For Co doped samples, a nominal ratio of Ba:FeAs:CoAs was heated up to 1180 °C and kept for 10 hours. The melt was slowly cooled down at a rate of 3 - 4 °C /hour. The resulting crystals were carefully separated from the flux. The crystals are brittle. The surface of the plate-like crystal is orthogonal to the [001] direction.

1.4.2 Sample Characterizated by EDS, X-ray Diffraction and SQUID

The physical properties of the single crystals was further characterized by various techniques including EDS (Energy Dispersive X-ray Spectroscopy), X-ray diffraction, SQUID (Superconducting Quantum Interference Devices) and resistivity. EDS showed that the actual Co concentrations are 0.082 and 0.099 for the nominal concentration of x = 0.10 and 0.105, as summarized in the 2nd row of Table 1.2. X-ray diffraction showed that the crystal of x = 0.082 has a tetragonal $ThCr_2Si_2$ structure with space group I4/mmm at room temperature (Sefat et al., 2008b). We also confirmed the diamagnetic susceptibility arising from the superconductivity for x = 0.04, 0.082 and 0.099 by SQUID, as shown in Fig. 1.5. We also measured the in-plane resistivity ρ_{ab} for these crystals, as discussed in the next section.

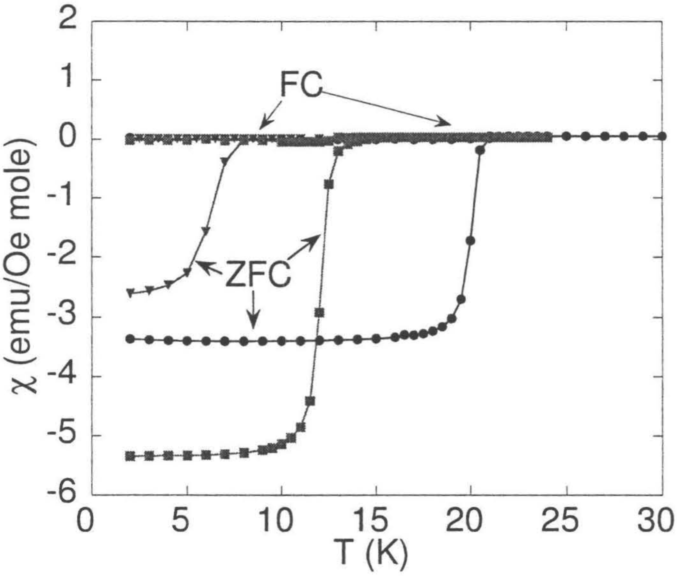

Figure 1.5 The temperature dependence of the magnetic susceptibility χ measured by zero field cooling (ZFC) and field cooling (FC) below 30 K for Ba(Fe$_{1-x}$Co$_x$)$_2$As$_2$ (x = 0.04 (▼), 0.082 (•) and 0.099 (■)) crystals with B_{ext} = 20 Oe applied within the *ab*-plane .

1.4.3 Resistivity of Ba(Fe$_{1-x}$Co$_x$)$_2$As$_2$ Crystals

At least 4 groups have reported comprehensive resistivity measurements of the Co doped 122 system to date (Ning et al., 2009a, Ni et al., 2008, Chu et al., 2009, Wang et al., 2009b). Highly consistent results between different groups assure us that our Ba(Fe$_{1-x}$Co$_x$)$_2$As$_2$ crystals are of high quality. We show the in-plane resistivity ρ_{ab} measurements by our group (Ahilan et al., 2009) in Fig. 1.6. In the parent compound BaFe$_2$As$_2$ (x =0), we observe a sharp drop of ρ_{ab} at $T_{SDW} = T_S$ = 135 K due to the simultaneous structural and magnetic phase transitions. However, this sharp drop changes to an abrupt upturn for lightly Co doped samples with x = 0.02 and 0.04. We define the SDW phase transition temperature T_{SDW} as the minimum or maximum slope of ρ_{ab}. The justification of this procedure will be explained in chapter 3 (see Fig. 3.10). Larger Co doping continuously suppresses the onset temperature of the upturn of ρ_{ab}. The upturn becomes very small for $x = 0.051$, and eventually disappears at $x = 0.082$. The origin of the significantly different behavior of ρ_{ab} near the SDW transition between the parent compound and the Co-doped samples are still under debate. It could be from the modification of the Fermi surface with Co doping, as we have discussed in section 1.2.4, or the suppression of the tetragonal to orthorhombic structural phase transition temperature. In Co doped samples, the tetragonal to orthorhombic structural transition precedes the SDW transition, i.e., $T_{SDW} < T_S$ (Chu et al., 2009).

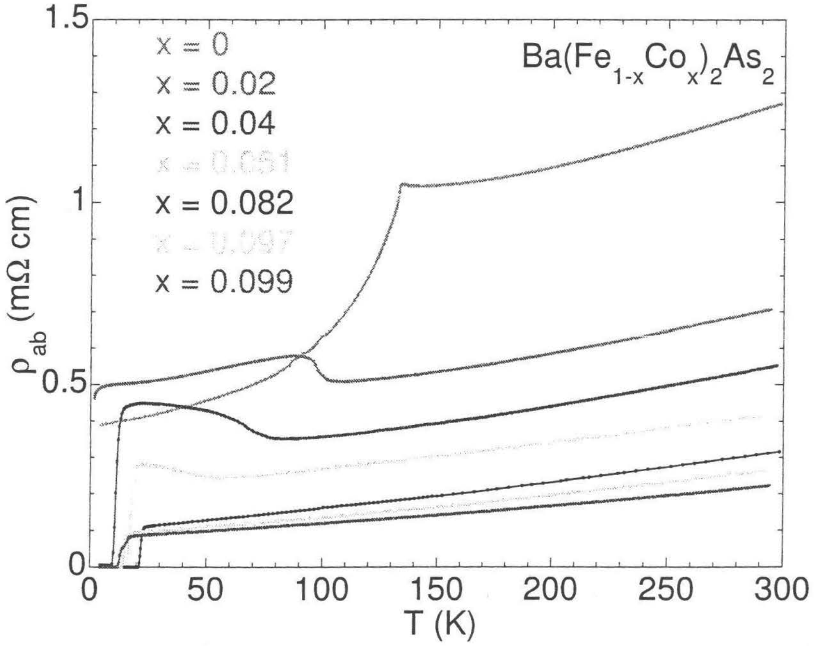

Figure 1.6 The temperature dependence of the in-plane resistivity ρ_{ab} of $Ba(Fe_{1-x}Co_x)_2As_2$ single crystals.

We also notice that for $x = 0.02$, ρ_{ab} decreases slightly near the base temperature. This hints at the on-set of superconductivity, but ρ_{ab} does not decrease to zero. For $x = 0.04$, ρ_{ab} drops to zero below $\sim$ 11 K due to superconductivity. We define the onset temperature of superconductivity, T_c, as the temperature where ρ_{ab} decreases by 10 % from the extrapolated linear behavior of ρ_{ab} at higher temperatures. Although T_c is as high as 11 K for $x = 0.04$ crystal, the anomaly associated with the magnetic phase transition is still evident at $T_{SDW} = 66$ K. T_c increases with increasing Co doping, and reaches the highest value of 22 K for $x = 0.082$, then starts to decrease. $T_c = 15$ K for $x = 0.099$. We tabulate T_{SDW} and T_c of our samples in Table 1.2.

Table 1.2 Parameters for $Ba(Fe_{1-x}Co_x)_2As_2$ determined by various techniques.

Nominal x	0	0.020	0.040	0.10	0.105
x by EDS	0	N/A	N/A	0.082 ± 0.005	0.099 ± 0.005
T_c (K)	0	4 ± 1	11.0 ± 0.5	22.0 ± 0.5	15.0 ± 0.5
T_{SDW} (K)	135 ± 1	100 ± 1	66 ± 1	N/A	N/A

We show the temperature dependence of ρ_{ab} for three superconducting samples with $x = 0.082, 0.097, 0.099$ in a magnified scale in Fig. 1.7(a). These samples do not show the signature of a SDW transition. ρ_{ab} depends linearly on temperature from T_c up to ~100 K, as shown by the straight dotted lines in the figure. We also show the temperature dependence of the derivative of ρ_{ab}, $d\rho_{ab}/dT$ in Fig. 1.7(b). Notice that upon cooling, $d\rho_{ab}/dT$ levels off toward a constant value near ~ 100 K for all three Co dopings. This finding indeed implies that $\rho_{ab} \propto T$. This T-linear behavior just above T_c is not consistent with the canonical Fermi liquid behavior, $\rho \sim T^2$. In chapter 5, we will demonstrate that spin fluctuations are highly enhanced near T_c from the measurement of the nuclear spin-lattice relaxation rate $1/T_1$. In fact, $1/T_1$ violates the Korringa law expected for a Fermi liquid. These results indicate that the high T_c superconductivity of iron pnictides arises from a novel electronic state with $\rho_{ab} \propto T$. It is interesting to recall that $\rho_{ab} \propto T$ was also observed for high T_c cuprates (Allen, 1989, Ong, 1990).

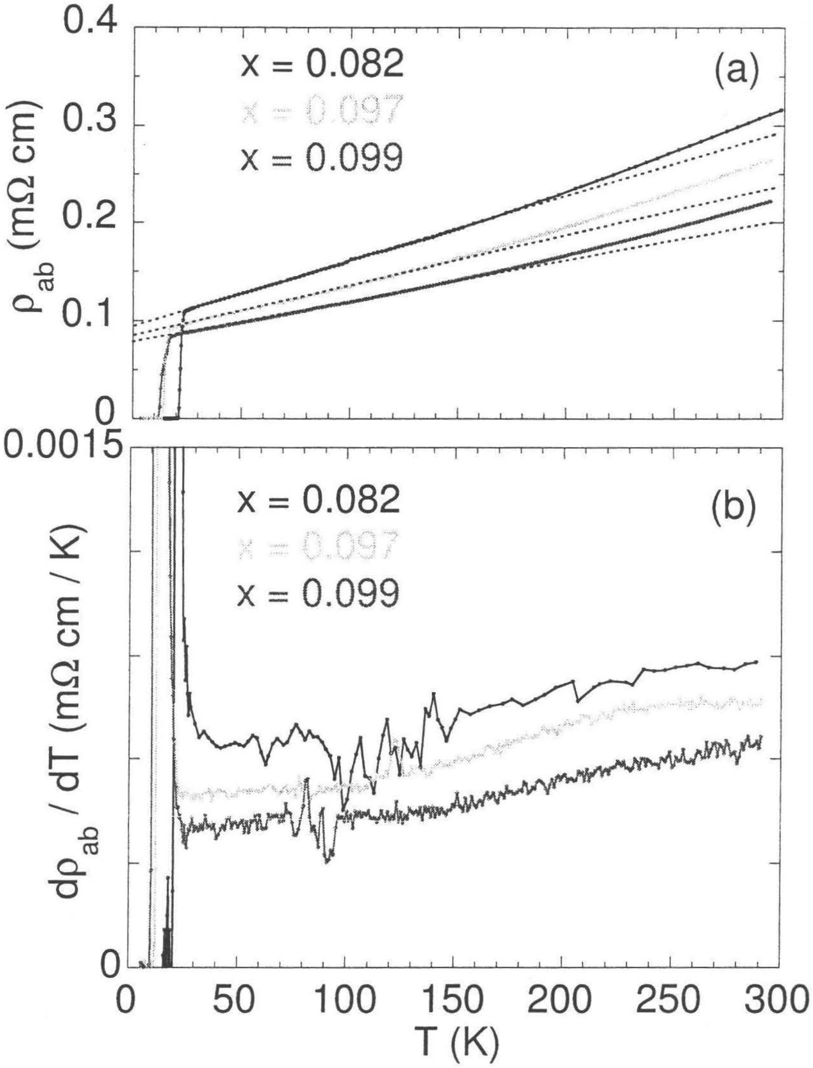

Figure 1.7 (a) The temperature dependence of the in-plane resistivity ρ_{ab} of $Ba(Fe_{1-x}Co_x)_2As_2$ single crystals for the optimal ($x = 0.082$) and overdoped ($x = 0.097$, 0.099) regimes shown with a magnified scale. Straight dotted lines are drawn above T_c to show the T-linear behavior up to ~100 K. (b) The temperature dependence of the derivative of ρ_{ab}, $d\rho_{ab}/dT$. Notice that upon cooling, $d\rho_{ab}/dT$ levels off toward a constant value near ~ 100 K, implying that $\rho_{ab} \propto T$.

1.5 Phase Diagram of $Ba(Fe_{1-x}Co_x)_2As_2$

We construct a composition-temperature ($x - T$) phase diagram of compounds $Ba(Fe_{1-x}Co_x)_2As_2$ from Fig. 1.6. We emphasize that our group was the first in the world to map out the electronic phase diagram (Ning et al., 2009a). In Fig. 1.8, we show an updated phase diagram with accurate calibration of the Co concentration by EDS as summerized in Table 1.2. Our phase diagram is quantitatively the same as those reported subsequently by other groups (Ni et al., 2008, Chu et al., 2009). On the

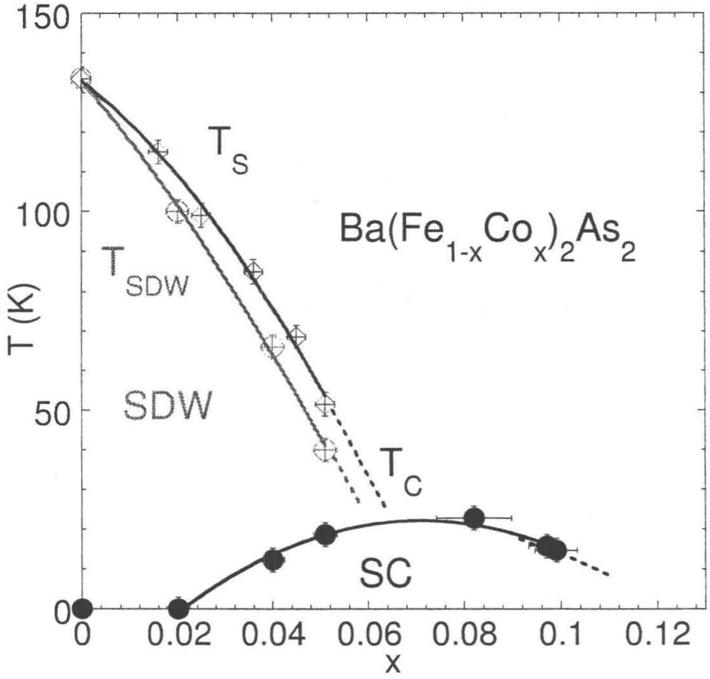

Figure 1.8 The composition-temperature phase diagram of $Ba(Fe_{1-x}Co_x)_2As_2$. T_s (◇), adapted from Fisher's reports (Chu et al., 2009), denotes the structural phase transition. T_{SDW} (○) denotes the SDW magnetic phase transition. T_c (●) denotes the superconducting transition. Solid and dashed lines are guides to eyes.

other hand, the phase diagram reported by some other research groups (Wang et al., 2009b) has the superconducting dome extending to larger x. In view of the fact that actual values of x tend to be significantly smaller than the nominal compositions, the discrepancy should be attributed to inaccurate calibration of x by those groups' EDS measurements.

In Fig. 1.8, we can clearly see that doping Co gradually suppresses T_S and T_{SDW}, and induces superconductivity at $0.02 < x \leq 0.06$ (underdoped region). Then as the level of Co doping increases to $x \sim 0.06 - 0.08$ (optimum doping), the highest $T_c \sim 22$ K is achieved. With $x > 0.08$ (overdoped region), increasing Co concentrations suppresses T_c, and superconductivity disappears for $x \gtrsim 0.12$. For 1111 system, Luetkens et al. presented the electronic phase diagram of $LaO_{1-x}F_xFeAs$ determined by μSR, X-ray diffraction, and magnetic susceptibility measurements (Luetkens et al., 2009), and claimed that the SDW phase does not coexist with superconductivity. The boundary between two phases is at fluorine concentration $x \sim 0.042$. Whether the magnetically ordered phase coexists with the superconducting phase at a microscopic level or not is still an open question in the FeAs-based compounds.

1.6 Organization of Thesis

A large number of researchers around the world placed enormous efforts on research into $Ba(Fe_{1-x}Co_x)_2As_2$ over the last year and a half. The results presented in this thesis are a part of the massive research work over the last year. Our primary focus will be on the Nuclear Magnetic Resonance (NMR) measurements conducted by our group since the discovery of the Fe-based superconductor. This thesis includes four additional chapters: Chapter 2 presents a brief introduction to experimental method and the theoretical background of NMR. In chapter 3, we will present the ^{75}As and

^{59}Co NMR lineshapes for x =0, 0.02, 0.04, 0.082. In chapter 4, we will discuss the intrinsic static magnetic susceptibilities deduced from NMR Knight shifts. In chapter 5, we will discuss the dynamic magnetic susceptibility as measured by $1/T_1T$, followed by conclusions in chapter 6.

Chapter 2

Fundamentals of NMR

Nuclear Magnetic Resonance (NMR) is an experimental technique that is used to manipulate and study the behavior of nuclear spins at atomic sites. We can use NMR to measure the magnetic field, the electric field gradient (EFG) and their fluctuations, at the position of nuclei of interest. A major thrust of NMR is that it is a local probe of electronic properties of solids, because nuclear spins are under the influence of electrons in their vicinity. In the study of strongly correlated electrons systems such as high T_c cuprate superconductors, NMR played a pivotal role in elucidating the local properties of electrons.

In this thesis, we describe NMR experiments performed on ^{75}As and ^{59}Co nuclei in $\mathrm{Ba(Fe}_{1-x}\mathrm{Co}_x)_2\mathrm{As}_2$ compounds. NMR frequency (lineshape) measurements provide information on the static magnetic properties at the position of the ^{75}As and ^{59}Co nuclei, which are averaged over the timescale of the NMR measurements ($\gtrsim$ μsec). The measurements of spin-lattice relaxation rate $1/T_1$, which is the timescale for the nuclear magnetization M to recover to its thermal equilibrium M_0 after saturation, provide information on dynamic magnetic properties, i.e., the density of low energy excitations of the electronic system, or equivalently, low frequency fluctuations. In the following, we will describe more details on the basic theories and techniques of NMR.

2.1 NMR/NQR Frequency and Knight Shift

The effective nuclear spin Hamiltonian $\mathcal{H}$ for calculating energy levels and NMR frequencies can be expressed as,

$$\mathcal{H} = -\gamma_n \hbar \vec{B}_{eff} \cdot \vec{I} + \mathcal{H}_Q, \tag{2.1}$$

where γ_n is the nuclear gyromagnetic ratio, $\hbar$ is the Planck's constant divided by 2π, $\vec{I}$ is the nuclear spin vector, and $\mathcal{H}_Q$ is the Hamiltonian describing the interaction of the nuclear quadrupole moment with the local electric field gradient (EFG). $\vec{B}_{eff} = \vec{B}_{ext}(1+K)$, is the effective magnetic field at the site of the nuclei, where $\vec{B}_{ext}$ is the applied external field, and K is the Knight shift. We list the values of γ_n, I and the natural abundance of ^{75}As and ^{59}Co nuclei in Table. 2.1.

Table 2.1 Nuclear gyromagnetic ratio γ_n, nuclear spin I and the natural abundance of ^{75}As and ^{59}Co nuclei.

Nuclei	γ_n(MHz/Tesla)	I	Natural abundance (%)
^{75}As	7.2919	3/2	100
^{59}Co	10.054	7/2	100

In Fig. 2.1, we show the schematic energy levels and NMR frequencies of the nuclear spin $I = 3/2$ for the ^{75}As nucleus. In the presence of a static magnetic field B alone, the Zeeman effect splits the energy levels with an equal spacing of $\gamma_n \hbar B$. In this case, there is only one resonance frequency, $f_0 = \gamma_n B$. However, the presence of a nuclear quadrupole interaction $\mathcal{H}_Q$ shifts all energy levels. The NMR frequencies then have three transitions from $I_z = (2m-1)/2$ to $(2m+1)/2$ (where m= -1,0,1) with the separation $\sim \nu_Q^z$ in the high field limit (for simplicity, we assume B is along the z-axis, and the main principal axis of the EFG tensor is also along the z-axis). The magnitude of ν_Q^z describes the strength of the nuclear quadrupole interaction between the nuclear quadrupole moment and the EFG at the nuclear site of interest, which will be discussed in details in section 2.3. In Fig. 2.1(b), we can see that the first order perturbation effect does not shift the central resonance frequency f_0, but the second order perturbation shifts the central resonance frequency by $\nu_Q^z(2)$. In principle, the second order effect may also result in small changes in the resonance frequency of the satellite transitions, but these effects are generally much smaller than the first order effect, ν_Q^z.

In Fig. 2.1, we have ignored the shift of transitions by the Knight shift, K. K is defined as a fractional shift of the resonance frequency f of the central transition (m = 0), relative to the NMR frequency of the bare nuclei, $f_0 = \gamma_n B$. Thus $K = (f - f_0)/f_0$, or alternatively $f = \gamma_n B(1+K)$. If we take into account the nuclear quadrupole interaction as well, the central frequency ($m = 0$) is given by,

$$f = \gamma_n B(1+K) + \nu_Q^z(2). \tag{2.2}$$

The effect of $\nu_Q^z(2)$ in not necessarily negligible, and can be positive or negative depending on the relative orientation of the applied field B_{ext} with respect to the EFG tensor. $\nu_Q^z(2)$ could shift the central transition frequency much more than the Knight shift does, thus it is extremely important to subtract the effect of $\nu_Q^z(2)$ to obtain the intrinsic Knight shift. We will utilize the fact that the first term in Eq. 2.2 is $\propto B$, while $\nu_Q^z(2) \propto 1/B$, to separate the two contributions and obtain the intrinsic ^{75}K for $Ba(Fe_{1-x}Co_x)_2As_2$ in chapter 4.

(a) NMR energy levels

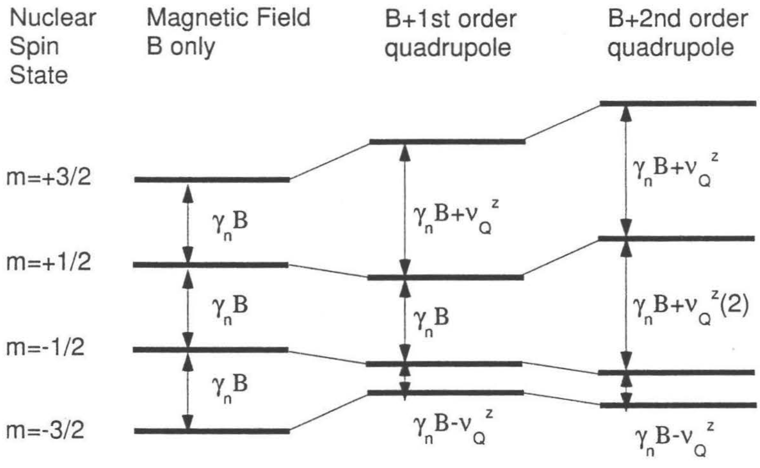

(b) NMR frequencies

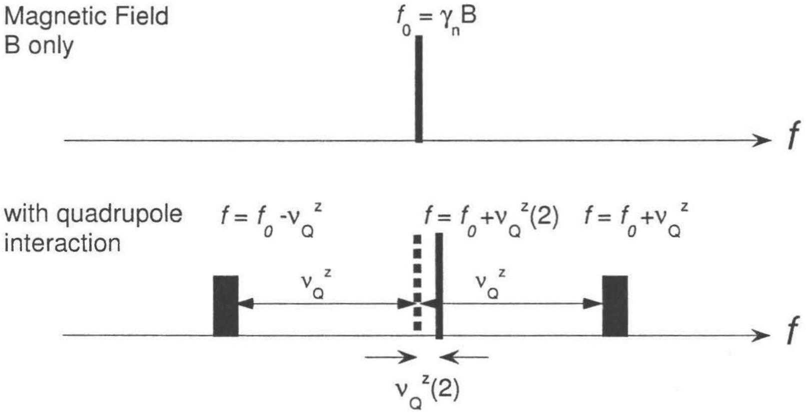

Figure 2.1 (a) Energy levels for nuclear spin $I = 3/2$. The magnitude of ν_Q^z represents the strength of the nuclear quadrupole interaction between the nuclear quadrupole moment and the EFG at the nuclear site. $\nu_Q^z(2)$ arises from the second order perturbation to the frequency of the central transition. (b) Schematic NMR frequencies for nuclear spin $I = 3/2$. For simplicity, we assume $K = 0$.

2.2 Origin of K (K_{chem}, K_s)

The Knight shift K includes the chemical shift K_{chem} and the electron spin shift K_s, so $K = K_s + K_{chem}$. The chemical shift K_{chem} arises from the coupling between the nuclear spin and two types of magnetic fields induced by orbital motion of electrons: one is the diamagnetic shielding currents of electrons associated with the diamagnetic susceptibility, χ_{dia}; the other is associated with the Van Vleck or orbital paramagnetic susceptibility, $\chi_{orbital}$. χ_{dia} is caused by a quantum mechanical effect that arises from the diamagnetic shielding current of the electrons, and does not have any temperature dependence. $\chi_{orbital}$ arises from the mixing of the atomic energy levels in the presence of the magnetic field. From perturbation theory (Ashcroft and Mermin, 1976), $\chi^z_{orbital} \propto \sum_n \frac{<0|(L_z)|n>^2}{E_n - E_0}$, where L_z is the electron orbital angular momentum. $E_n - E_0$ is the energy separation caused by the crystal field, and is ~ 1 eV $= 11,600$ K, and is much larger than the temperature for our NMR experiments ($\lesssim 300$ K). Accordingly, $\chi_{orbital}$ does not have significant temperature dependence, and may be considered as temperature independent in our data analysis. Another important fact is that K_{chem} in principle can be anisotropic. For example, the chemical shift tensor $(K^x_{chem}, K^y_{chem}, K^z_{chem}) = (220,186,25)$ parts per million for the ^{13}C nucleus in the famous soccer-ball-shape fullerene C_{60} (Yannoni et al., 1991).

The electron spin shift K_s arises from the hyperfine coupling between the nuclear spin and the electron spin polarized by the static applied magnetic field B, and therefore $K_s \propto \chi_s$. χ_s can be temperature dependent in strongly correlated electron systems. More specifically, K_s may result from two types of hyperfine interactions: one is the Fermi contact interaction between the nuclear spin and s-electrons, the other is the dipole-dipole interaction between the nuclear spin and the non-s-electron spins. In what follows, we summarize the origin of these effects.

2.2.1 The Fermi Contact Interaction

The Fermi contact hyperfine Hamiltonian can be expressed as,

$$\mathcal{H}_{contact} = \frac{8\pi}{3}\gamma_e\gamma_n\hbar^2\vec{I}\cdot\vec{S}\delta(\vec{r}), \tag{2.3}$$

where $\vec{S}$ is the spin density operator, $\hbar = h/2\pi$, h is Planck's constant, $\vec{r}$ is the position vector of the electron, γ_e and γ_n are the gyromagnetic ratios of electron and nucleus, respectively, and the nucleus is taken to be at the origin. For metals with spin susceptibility χ_s, this term leads to a Knight shift given by,

$$K_s = \frac{8\pi}{3} < |\psi(0)|^2 >_{E_F} \chi_s, \tag{2.4}$$

where $< |\psi(0)|^2 >_{E_F}$ is the square magnitude of the electronic wave function averaged over the Fermi surface and evaluated at the site of the nucleus. Note that non-s electrons have no contact term, since their wave functions vanish at the origin. The Fermi contact interaction in Eq. (2.3) is isotropic due to the isotropic nature of the s-electron wave function. Thus the Fermi contact interaction only contributes to the isotropic parts of the Knight shift.

Unless s-orbitals contribute to conduction electrons, the Fermi contact interaction does not contribute directly to K_s. However, there is another process called "inner core polarization". For example, $3d$ electron spins at Co sites have a direct exchange interaction with $1s$, $2s$ and $3s$ orbitals, hence the polarization of Co $3d$ electron spins in an applied magnetic field results in that of these s-electrons. The polarized s-electrons in turn have a Fermi contact interaction with ^{59}Co nuclear spins. Generally, for transition metals, inner s-shells are polarized anti-parallel with $3d$ shells, hence this process results in a negative value of hyperfine coupling (i.e. negative contribution to K_s).

2.2.2 Dipole-dipole Interaction

Nuclear spin I and non-s-electron spin S interact with each other via the dipole-dipole interaction. The dipole-dipole interaction may be expressed as,

$$\mathcal{H}_{dip-dip} = \frac{\gamma_e \gamma_n \hbar^2}{r^3}[3\frac{(\vec{I}\cdot\vec{r})(\vec{S}\cdot\vec{r})}{r^2} - \vec{I}\cdot\vec{S}], \tag{2.5}$$

and gives rise to an anisotropic hyperfine coupling for partially filled p and d orbitals. For example, the $2p_z$ orbitals give rise to an anisotropic Knight shift tensor as (Abragam, 1961, Slichter, 1990),

$$K_{\parallel} = \frac{4}{5} < \frac{1}{r^3} > \chi^s; K_{\perp} = -\frac{2}{5} < \frac{1}{r^3} > \chi^s, \tag{2.6}$$

where the subscript defines the direction of the magnetic field applied; "$\|$" is B $\|$ z (i.e. along the direction of the lobe of the p_z orbital), while "$\perp$" is the direction perpendicular to the z-direction. $< \frac{1}{r^3} >$ is the average radial electron distribution which is generally determined by electron spin resonance experiments.

2.2.3 Hyperfine Coupling A_{hf}

The nuclear spins couple with the electron spins by a Fermi contact or dipole-dipole interaction via hyperfine coupling A_{hf}. The Hamiltonian of the hyperfine coupling between the nuclear spin and the electron spin can be expressed as,

$$\mathcal{H}_{hf} = \vec{I} A_{hf} \vec{S}. \tag{2.7}$$

In principle, A_{hf} is a tensor quantity, but for simplicity, we approximate it as a scalar below. The hyperfine coupling A_{hf} quantifies how large the hyperfine interaction energy is, or alternatively, how much magnetic field is produced at the location of the nucleus by electron spins.

We will assume in Chapter 4 that a combination of various hyperfine interactions gives rise to a negative on-site hyperfine coupling, $A_{on-site} < 0$, at the site of a ^{59}Co nucleus. In Ba(Fe$_{1-x}$Co$_x$)$_2$As$_2$ compounds, the Fe^{2+} electron spins at four nearest neighbor (N.N.) sites also exert sizable hyperfine fields to the ^{59}Co nuclear spins for the following reason. Co^{2+} ions are in the square lattice formed by Fe^{2+} ions, and Fe $3d$ spins enter the $4s$ orbital of Co^{2+} ions through Fe-Co hybridization. The polarized $4s$ electrons in turn interact with Co nuclear spins via Fermi's contact interaction. This hyperfine interaction contributes to the so-called transferred hyperfine coupling, $B_{transfer}$.

Similarly, ^{75}As nuclear spins experience the transferred hyperfine coupling from Fe^{2+} spins at N.N. sites as well. To distinguish from $B_{transfer}$, we name it $C_{transfer}$. We schematically show the hyperfine couplings for Co^{2+} and As^{3-} ions in Fig. 2.2 (a) and (b). Experimentally, we can determine the hyperfine coupling A_{hf} from the K versus χ plot analysis (Jaccarino, 1966). Because the electron spin shift K_s is related with the electron spin susceptibility χ_s by,

$$K_s = \frac{A_{hf}(q=0)}{N_A \mu_B} \chi_s, \tag{2.8}$$

where N_A is Avogadro's constant and μ_B is the Bohr magneton, we can plot the Knight shift as a function of the bulk uniform susceptibility χ with temperature as the implicit parameter. If the temperature dependence of K and χ arises from only one source, we expect to observe a linear relation in the K vs. χ plot. The derivative

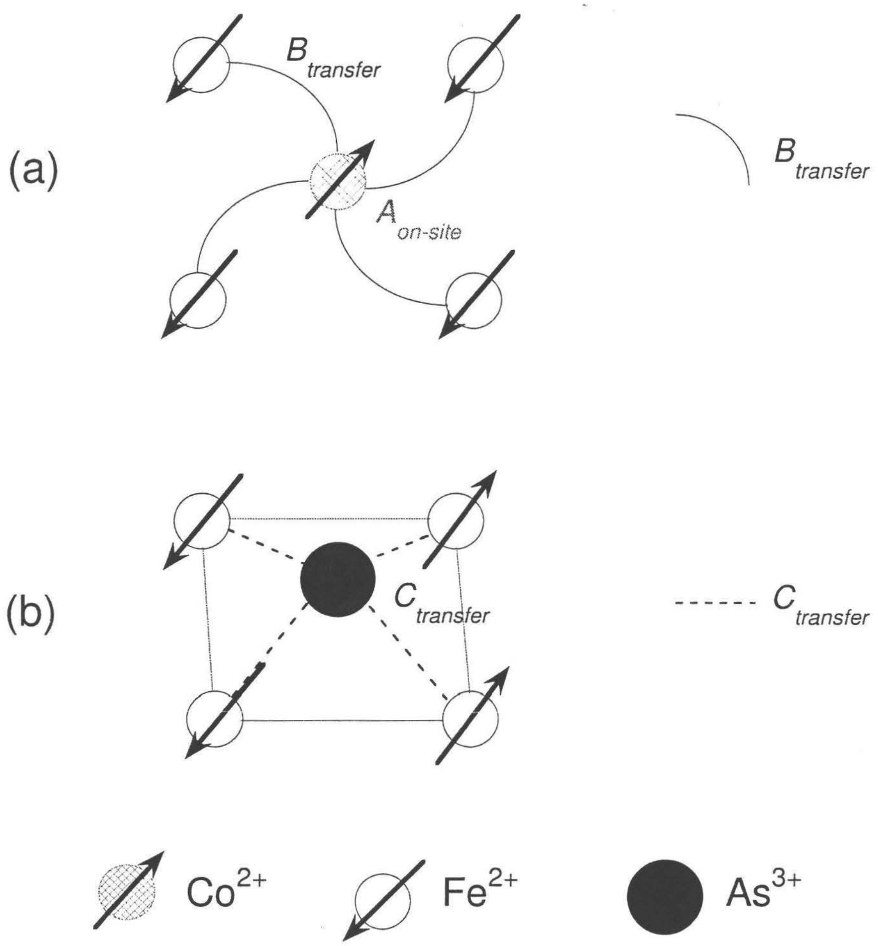

Figure 2.2 (a) A schematic representation of the on-site ($A_{on-site}$) and transferred ($B_{transfer}$) hyperfine couplings for the Co^{2+} ions in the plane of the antiferromagnetically aligned Fe^{2+} square lattice. (b) A schematic representation of the transferred ($C_{transfer}$) hyperfine coupling for As^{3-} ions which are located above or below the center of the Fe^{2+} square lattice.

of Eq. (2.8) gives,

$$A_{hf}(q=0) = N_A \mu_B \frac{\Delta K}{\Delta \chi}. \tag{2.9}$$

We utilize this property in section 4.2.

2.3 Nuclear Quadrupole Interaction

In Eq. (2.1), we included the nuclear quadrupole interaction Hamiltonian, $\mathcal{H}_Q$ which describes the interaction between the nuclear quadrupole moment Q and the electric field gradient (EFG) at the position of the nucleus. Therefore, $\mathcal{H}_Q$ probes the local charge and lattice environment through the second derivative of the total Coulomb potential at the position of nuclear spins. Spin $I = 1/2$ nuclei do not experience nuclear quadrupole interaction because Q = 0, and only the nuclear spins with $I \geq 1$ interact with the charge environment via nuclear quadrupole interaction.

Nuclear quadrupole moment Q is calculated from the expansion of the nuclear charge distribution in spherical harmonics of order $l = 2$. The order of $l = 0$ (its charge Ze, monopole moment) does exist, which interacts with an electric field. However, this interaction is independent of the direction of the spin of the nucleus, so it does not affect the transitions between energy levels which are of interest here. The order of $l = 1$ (the electric dipole moment) is prohibited by the fact that nuclear states have well defined parity. In fact parity prohibits any charge multipoles with odd l. Next order is of $l = 2$, namely the quadrupole moment Q, is defined by

$$Q = \frac{1}{2e} \int (3z^2 - r^2)\rho(\vec{r}) d^3x, \tag{2.10}$$

where $\rho(\vec{r})$ is the charge distribution of the nucleus for the $I_z = I$ state and e = $|e|$ is the electron charge. The unit of $\rho(\vec{r})$ is that of charge divided by volume, therefore the quadrupole moment Q has units of area. Obviously, the distribution of $\rho(\vec{r})$ affects the sign and size of the quadrupole moment Q. If $\rho(\vec{r})$ is spherically symmetric, then Q will disappear. If the charge distribution is extended along the z-axis, the quadrupole moment will be positive; if $\rho(\vec{r})$ is flattened within the xy-plane, the quadrupole moment will be negative.

Higher order moments of the charge distribution such as hexapole and octupole do exist, but the interaction effects are expected to be much smaller. The interaction strength is expected to fall off as (Abragam, 1961, Slichter, 1990)

$$(\frac{R_n}{R_e})^l \approx (10^{-5})^l, \tag{2.11}$$

where R_n (R_e) is the radius of the nuclear (electronic) charge distributions. We can estimate the order of the rapid drop of the interaction strength with increasing l between $l = 0$ and $l = 2$ as an example. The $l = 0$ interaction energy is of the order of 10 eV. While typical quadrupole resonant frequencies in NMR measurements are on the order of 10 MHz $\sim 10^{-8}$ eV, which is $\sim$ 10 orders of magnitude weaker.

In general, the nuclear quadrupole Hamiltonian $\mathcal{H}_Q$ can be expressed as (Abragam, 1961, Slichter, 1990),

$$\mathcal{H}_Q = \frac{\nu_Q^z h}{2}[I_z^2 - \frac{1}{3}I(I+1) + \frac{1}{6}\eta(I_+^2 + I_-^2)], \tag{2.12}$$

where I is the nuclear spin of the observed nuclei ($I = \frac{7}{2}$ for ^{59}Co, and $I = \frac{3}{2}$ for ^{75}As). ν_Q^z is given by,

$$\nu_Q^z = \frac{3e^2 q_z}{2hI(I+1)}Q, \tag{2.13}$$

where $eq_z = \frac{\partial^2 V}{\partial z^2}$ is the z-axis component of the electric field gradient (EFG) at the nuclear position, where V is the electrostatic potential. On the other hand, the Laplace equation for the electrostatic potential is,

$$\frac{\partial^2 V}{\partial x^2} + \frac{\partial^2 V}{\partial y^2} + \frac{\partial^2 V}{\partial z^2} = 0. \tag{2.14}$$

This implies that the three principle components of the quadrupole interaction will sum up to zero,

$$\nu_Q^x + \nu_Q^y + \nu_Q^z = 0. \tag{2.15}$$

The electric field gradient is axially symmetric and $\nu_Q^x = \nu_Q^y = -\nu_Q^z/2$ if the crystal symmetry is cubic or tetragonal. More generally, $\nu_Q^x \neq \nu_Q^y$, and we define the asymmetry η as,

$$\eta = |\frac{\nu_Q^x - \nu_Q^y}{\nu_Q^z}|, \tag{2.16}$$

where we take $|\nu_Q^z| \geq |\nu_Q^y| \geq |\nu_Q^x|$ by choosing the coordinate directions appropriately.

2.4 The Spin-Lattice Relaxation Rate, $1/T_1$

The spin-lattice relaxation time T_1 represents a time scale of how quickly a nuclear spin ensemble returns to thermal equilibrium after we excite it by irradiating with r.f. pulses. We describe the T_1 process schematically in Fig. 2.3.

Since the recovery of the nuclear spin system to equilibrium is accompanied by the dissipation of the excess energy to the lattice, the theoretical derivation of the formula of $1/T_1$ relies on the fluctuation-dissipation theorem (White, 1970),

$$\frac{1}{T_1} = \frac{1}{2}\gamma_n^2 \int_{-\infty}^{+\infty} cos(\omega_0 t)\langle\{\delta B^+(t)\delta B^-(0)\}\rangle dt, \tag{2.17}$$

where $B^{\pm} = B_x \pm iB_y$ represents the transverse component of the magnetic field seen by nuclear spins. This equation tells us that if there is a large Fourier component at

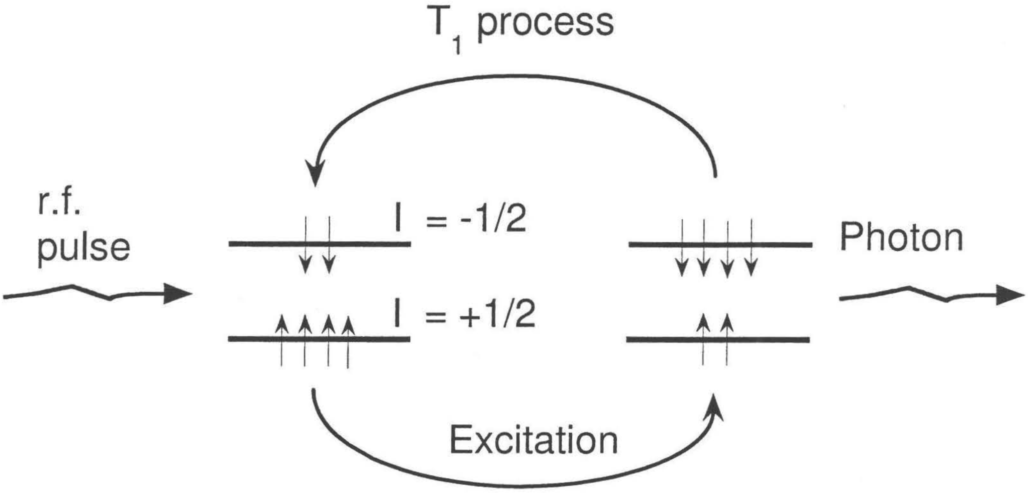

Figure 2.3 T_1 process. The nuclei is excited to a higher energy state by radiation by r.f. pulse at the NMR frequency, then relaxes back to its thermal equilibrium at a relaxation rate, $1/T_1$.

the NMR frequency ω_0 of the auto correlation function of the fluctuating transverse magnetic field, T_1 becomes shorter (i.e., $1/T_1$ becomes larger). Recall that electron spins yield hyperfine magnetic fields through

$$B^{\pm} = A_{hf}(S_x \pm iS_y). \tag{2.18}$$

Accordingly, $1/T_1$ can probe the frequency ω_0 component of spin-fluctuations. Moriya introduced the wavevector dependent hyperfine form factor $A(\mathbf{q}) = \sum_i A_i e^{i\mathbf{q}\cdot\mathbf{r}_i}$, where the summations is over all electron spins i at position $\mathbf{r}_i$ relative to the nucleus, and A_i represents the hyperfine coupling with the ith electron spin. By rewriting the electron spin-spin correlation function $S(\mathbf{r}, t) =< S(0,0)S(\mathbf{r}, t) >$ with it space-time Fourier component (Moriya, 1963)

$$S(\mathbf{q},\omega_0) = \frac{1}{2\pi}\sum_{\mathbf{r}_i}\int_{-\infty}^{+\infty} < S(0,0)S(\mathbf{r}_i,t) > exp[i(\mathbf{q}\cdot\mathbf{r}_i - \omega_0 t)], \tag{2.19}$$

$1/T_1$ may be rewritten as

$$\frac{1}{T_1} = \frac{\gamma_n^2}{2}\sum_q (|A(\mathbf{q})_a|^2 + |A(\mathbf{q})_b|^2)S(\mathbf{q},\omega_0), \tag{2.20}$$

where ω_0 is the NMR resonance frequency, and A($\mathbf{q}$) represents the wave vector dependent hyperfine form factor perpendicular to the applied external magnetic field. If $B \parallel$ Z, we can choose a = X and b = Y. Notice that $S(\mathbf{q},\omega_0)$ is what neutron scatters measure with inelastic measurements. In the low frequency limit, using

$$S(\mathbf{q},\omega_0) = \frac{2k_BT}{N_A\mu_B^2}\frac{\chi''(\mathbf{q},\omega_0)}{\omega_0}, \tag{2.21}$$

Eq. (2.20) can be also written as

$$\frac{1}{T_1T} = \frac{\gamma_n^2 k_B}{2\mu_B^2}\sum_q |A(\mathbf{q})|^2\frac{\chi"(\mathbf{q},\omega_0)}{\omega_0}, \tag{2.22}$$

Eq. (2.22) indicates that $1/T_1T$ probes the weighted average in $\mathbf{q}$-space of the low frequency electron spin fluctuations at the NMR frequency.

In simple metals, one can also calculate $1/T_1$ using Fermi's "golden rule" as (Slichter, 1990),

$$\frac{1}{T_1} = \int_0^\infty | < i|V_{e-n}|f > |^2\rho^2(\varepsilon)f(\varepsilon)[1-f(\varepsilon)]d\varepsilon, \tag{2.23}$$

where $f(\varepsilon)$ is the Fermi-Dirac distribution function, ρ is the electron density of states

(DOS), and $| < i|V_{e-n}|f > |^2$ is an averaged effective matrix element for the electron nuclear hyperfine scattering. $\rho(\varepsilon)f(\varepsilon)$ and $\rho(\varepsilon)[1-f(\varepsilon)]$ represent the occupied states and the unoccupied states, respectively.

The Fermi contact interaction with s-electrons is dominant in the hyperfine interaction of some simple metals, such as aluminum. Then $1/T_1$ for noninteracting electrons is given by,

$$\frac{1}{T_1 T} = \frac{64}{9}\pi^3\hbar^3\gamma_e^2\gamma_n^2[< |\psi(0)|^2 >_{E_F}]^2\rho^2(E_F), \tag{2.24}$$

where γ_e and γ_n are the gyromagnetic ratios of the electron and nucleus, $< |\psi(0)|^2 >_{E_F}$ is the square magnitude of the wavefunction averaged over the Fermi surface and evaluated at the site of the nucleus. That is, $1/T_1T$ = constant, or $1/T_1 \propto$ T. The underlying origin of this result is that the function $\rho(\varepsilon)[1-f(\varepsilon)]$ changes its value from $\sim \rho(\varepsilon)$ to $\sim$0 in the energy width of approximately k_BT for a Fermi degenerate system. This is known as the Korringa law (Korringa, 1950). Combining Eq. 2.24 with Eq. 2.4, we obtain the so-called "Korringa relation",

$$T_1T(K_s)^2 = (\frac{\hbar}{4\pi k_B})\frac{\gamma_e^2}{\gamma_n^2}\beta. \tag{2.25}$$

β is a phenomenological parameter that characterizes the importance of electron-electron interactions. For example, $\beta = 1$ for noninteracting s-electrons, and $\beta \sim 1.2$ for Al metal (Slichter, 1990), but $\beta = 0.07$ for the planar ^{63}Cu in the high-T_c superconductor $YBa_2Cu_3O_7$, where strong antiferromagnetic spin fluctuations enhance $1/T_1T$ (Millis et al., 1990).

2.5 Spin Echo and $1/T_1$ Measurement

To obtain the NMR data, we can use the so-called "spin echo" method. The procedure to create spin echo is depicted in Fig. 2.4 (a). First, we polarize the nuclear spin by a magnetic field $B_{ext} \parallel z$, and the nuclear magnetization M_0 is along the z-axis in thermal equilibrium. Next, we apply an alternating magnetic field H_1, or equivalently, r.f. pulses, tuned at the NMR frequency ω_0, perpendicular to B_{ext}. If the length of the r.f. pulse, t_{90°, and the strength of H_1 satisfy $\alpha\gamma_n H_1 t_{90^\circ} = \pi/2$, M_0 will be flipped by 90° to the xy-plane. α is a constant which depends on the transition we excite, e.g., $\alpha = 1$ for $I = 1/2$, but $\alpha = \sqrt{2}$ for the central transition of $I = 3/2$ (Fukushima and Roeder, 1981). This r.f. pulse is called the 90° pulse. After the 90° pulse, M_0 begins to undergo Larmour precession within the xy-plane. Some elements of M_0 precess faster or slower than the average precession frequency $\omega_0 = \gamma_n B_{ext}$ due to the distribution in the magnitude of B_{ext}. Accordingly, nuclear spins "dephase" within the xy-plane, and M_0 decays with a certain time constant $\mathrm{T_2}^*$. The precession of nuclear magnetization in the NMR coil induces a voltage across the NMR coil, i.e., free induction decay (FID) signal. However, if we apply a 180° pulse after time τ, dephased nuclear spins are refocused within the xy-plane at time 2τ. This phenomenon is called "spin echo". Spin echo is essentially two FID signals appearing back to back, as shown in Fig. 2.4. This procedure is called the 90°-180° pulse sequence.

The procedure to measure $1/T_1$ is described in Fig. 2.4(b). Before applying the 90°-180° pulse sequence, we invert M_0 by a 180° pulse to $-\mathrm{M}_0$ first, then wait for a certain "delay time", t. We collect the spin echo signal as a function of t, and obtain the recovery data. This method is called "inversion recovery". The recovery data are then fitted to the theoretical recovery functions which can be calculated for observed transitions of specific nuclear spin numbers. We show an example of $1/T_1$ recovery data for the ^{75}As nucleus in the superconductor Ba(Fe$_{0.918}$Co$_{0.082}$)$_2$As$_2$ in Fig. 2.4 (c).

2.6 NMR Electronics

I conducted all the NMR measurements presented in this thesis using the spectrometers constructed by previous group members at M.I.T. (Kent Thurber and Allen Hunt) using commercially available components. The electronics, shown in the block diagram in Figure 2.5 (Hunt, 2001), are required to accomplish two major tasks, as described by Hunt (Hunt, 2001). First, it provides the pulsed R.F. that excites the nuclear spins in the sample, and then the spin echo occurs. This requires careful timing and a pulse amplifier that provides peak to peak voltage of up to $\sim$ 300 V. Secondly, it needs to collect the extremely weak induced voltage signal from the spin echo (on the order of μ V), which requires a high gain system of amplifiers that connect to an analog to digital converter. The general flow of the electronics is outlined in the block diagram and is as follows.

1. The radio frequency (R.F.) sources (PTS 310 or 500) produce continuous R.F. from 1 - 500 MHz, which is gated into pulses by the TTL signals from the Aries spectrometer. The Aries is a product of TecMag company and controls all experimental timing and data acquisition, and is controlled by a Macintosh computer. These R.F. pulses pass through a homemade protection circuit and are amplified by the power amplifier (Kalmus LP 1000, 1kW). The homemade protection circuit contains simple logic elements and monitors several TTL lines to control the trigger line to the amplifier. The amplifier is engaged only for a brief time around the pulses and only when the logic of the protection circuit is satisfied. This prevents the accidental amplification of a large input signal, such as a continuous R.F., which could destroy the amplifier and fry precious samples. The amplified R.F. pulses are fed through

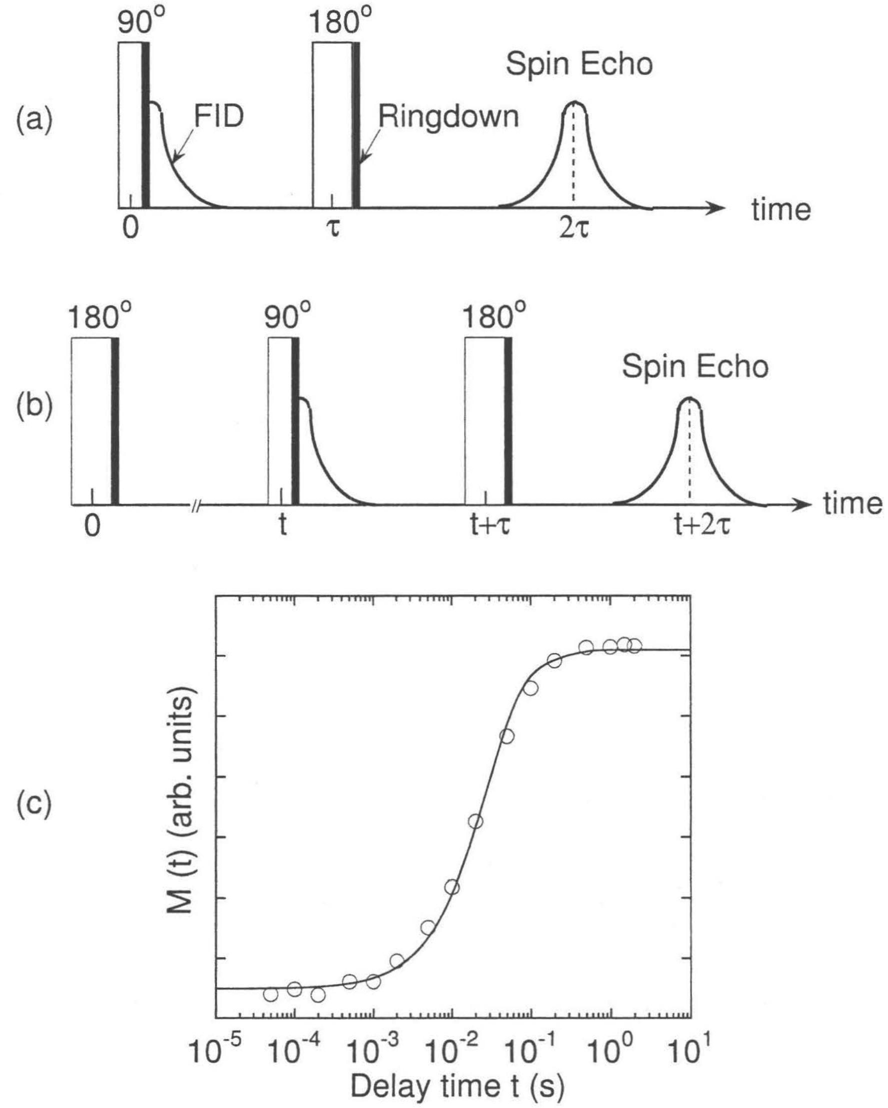

Figure 2.4 (a) The 90°-180° r.f. pulse sequence used for observing the spin echo. The separation between 90° and 180° pulse is typically $\tau = 15 \sim 25$ μs for all the data presented in this thesis. (b) The r.f. pulse sequence used for measuring $1/T_1$ where the time-integral of the spin-echo (the magnetization M(t)), is measured as a function of the delay time t. (c) An example of the ^{75}As nuclear spin recovery of M(t) for the central transition for $Ba(Fe_{0.918}Co_{0.082})_2As_2$ at 100 K. We obtain $^{75}(1/T_1) = 5.9785$ (1/s) from the fit to the theoretical expression, $M(t) = M_0 - a[0.1exp(-\frac{t}{T_1}) + 0.9exp(-\frac{6t}{T_1})]$, shown by a solid curve. M_0, a, and T_1 are the free parameters of the fit.

paired diodes into the NMR probe. The NMR probe consists of two adjustable capacitors and an inductive coil. This allows the circuit to be tuned to the chosen R.F. frequency and also matched to a 50 Ω impedance. The sample is placed inside a coil and is subjected to the oscillating magnetic field H_1 created by the R.F. pulses, which manipulate the nuclear spins. The coil also detects the induced voltage from the spin echo.

2. The signals from spin echo need to be amplified, and not influenced by the strong R.F. pulses or the ringdown that comes from the probe following the pulses, so a quarter wavelength cable and a pair of grounded crossed diodes are used. The voltage, which can be high at the probe, is at a minimum at the input side of the preamplifiers due to the standing wave in the quarter wavelength cable. The crossed diodes short any large voltage higher than the threshold $\sim$ 0.6 V to ground. Since the NMR signal is small, it does not turn the diodes on, and passes through without seeing the diodes. These precautions are necessary to prevent the saturation of the signal amplifiers by the R.F. pulses, which would render the amplifiers useless when the actual signal arrives. The signal is then amplified by the cascaded signal amplifiers (LN-2M or LN-2L by Doty, or ZFL-500LN by Mini-Circuits). Generally, we have two Doty amplifiers which are separated by a pair of R.F. mixers (Mini-circuit ZAY-1B) which are used as switches. The switches are only turned on when we want to acquire the signal to avoid unnecessary saturation of the amplifiers. The signal is split and mixed with two copies of the original R.F. for the phase sensitive detection. One branch has been delayed by 90° by a phase splitter such as Mini-Circuits ZSQ-180B or by an appropriate length of added cable called a delay line. We monitor both phases with and without the 90° delay. This is referred to, in the NMR literature, as *quadrature detection.* Mixing with the two different phases essentially allows us to get both the cosine and sine components of the signal at the chosen frequency (or

equivalently the real and imaginary parts). After mixing with the original R.F., the signal is close to DC (we say it is DC because its frequency is much smaller than that of R.F.). We amplify the signal once more with an op-amp (AD521) based circuit with a gain of 100 and a complementary bandwidth of ~100 kHz. This final signal can be viewed on an oscilloscope and is digitized by the analog to digital converter within the Aries. The analog to digital converter takes an input signal of -5 to +5 V, which is digitized into 2^{12} bins. To take full advantage of this number of bins, we try to amplify the signal so that the noise is as big as a few volts. Less amplification results in a step problem between bins, which are now too large compared to the size of the noise and signal, while too much amplification would exceed the capabilities of the analog to digital converter. An additional NMR technique that is crucial for separation of the small spin echo signal from the decay (ringdown) of the R.F. pulses is phase cycling. In our resonant circuit (Q ~ 40-100), the R.F. pulses require some time to decay and can obscure the spin echo signal. The pulse sequence is repeated with different phases for the R.F. pulses in order to cancel the decay of the R.F. pulse. For example, for the spin echo sequence, we use four different phases and add or subtract the resulting signals based on the sign of the echo, as shown in the following array.

90_x	τ	180_x	τ	$echo_y$	*Add*
90_{-x}	τ	180_x	τ	$echo_{-y}$	*Subtract*
90_{-x}	τ	180_y	τ	$echo_y$	*Add*
90_x	τ	180_y	τ	$echo_{-y}$	*Subtract*

Where 90 and 180 refer to the 90° and 180° pulses with the subscript indicating the phase of the R.F. pulse. In this sequence, any ringdown of the 90° or 180° pulses is canceled. The phase cycling technique dramatically helps us to measure the spin echo at short τ.

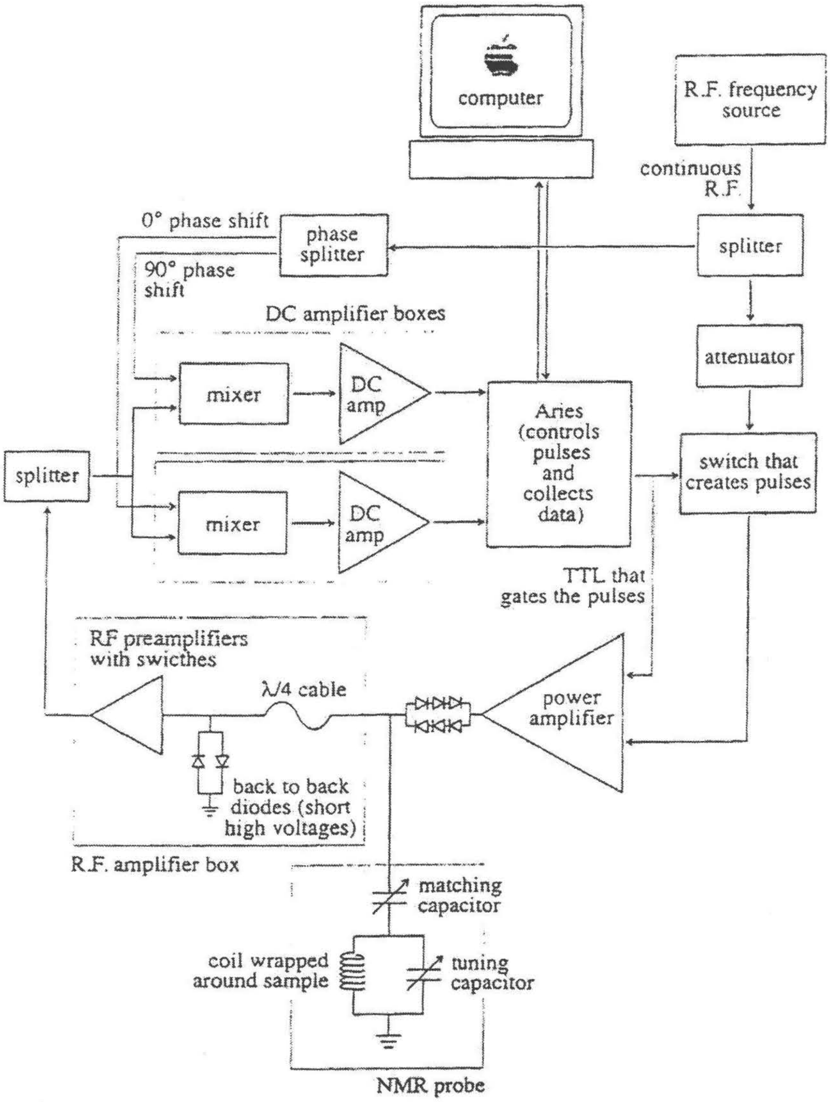

Figure 2.5 Schematic of electronics for NMR spectrometer at Imai labs (Hunt, 2001).

Chapter 3

NMR LineShapes

3.1 ^{75}As Lineshapes

In Fig. 3.1, we present the typical field swept ^{75}As NMR lineshapes at a fixed frequency of $f = 43.503$ MHz with the external field B_{ext} applied along the c-axis ($B_{ext} \parallel c$). As introduced in chapter 2, the nuclear spin Hamiltonian can be expressed as a summation of the Zeeman and nuclear quadrupole interaction terms,

$$\mathcal{H} = -\gamma_n h B \cdot (1+K) \cdot I + \frac{h\nu_Q^c}{6}\{3I_z^2 - I(I+1) + \frac{1}{2}\eta(I_+^2 + I_-^2)\}, \tag{3.1}$$

where h is Planck's constant, and $B = B_{ext} + B_{hf}$ is the magnetic field at the observed nuclear spin, where B_{ext} and B_{hf} represent the external field and the hyperfine field from the ordered moments, respectively. K is the Knight shift, and I is the nuclear spin number. The nuclear quadrupole interaction ν_Q^c is proportional to the Electric Field Gradient (EFG) at the observed ^{75}As site, and η is the asymmetry parameter of the EFG, $\eta = |\nu_Q^a - \nu_Q^b|/\nu_Q^c$. ^{75}As has nuclear spin $I = 3/2$ and nuclear gyromagnetic ratio $\gamma_n/2\pi = 7.2919$ MHz/Tesla. If the Zeeman term is much larger than the quadrupole term (i.e., the high field limit), each ^{75}As site gives rise to three transitions from $I_z = \frac{2m+1}{2}$ to $\frac{2m-1}{2}$ (where m = -1, 0, 1) in the paramagnetic state.

First, we briefly discuss the ^{75}As NMR results in undoped $BaFe_2As_2$ ($x = 0$, T_{SDW} = 135 K). Fig. 3.1(a) shows the ^{75}As lineshape with $B_{ext} \parallel c$. In Fig. 3.2(a), B_{ext} is applied within the ab-plane ($B_{ext} \parallel ab$). We observe only one set of ^{75}As NMR signals above T_{SDW}. This suggests that there is only one type of As site in the undoped parent compound as expected from the crystal structure in Fig. 1.1. From the split between the main peak (central transition, $m = 0$) and the satellite peaks (m = -1, 1) in Fig. 3.1(a), ΔB $\sim$ 0.316 Tesla, we estimate $^{75}\nu_Q^c = {}^{75}\gamma_n \Delta \mathrm{B}$ = 2.3 MHz. From the split in Fig. 3.2(a), ΔB $\sim$ 0.162 Tesla, we estimate $^{75}\nu_Q^a = {}^{75}\nu_Q^b$ = 1.188 MHz. Thus $\eta \cong 0$ at 145 K for ^{75}As, as expected for the tetragonal symmetry. The satellite transitions are somewhat broader than the central peak, but are still fairly sharp, implying that ν_Q^c has a well defined value. At 77 K ($< T_{SDW}$), the ^{75}As NMR lines with $B_{ext} \parallel c$ split into two sets as shown in Fig. 3.4(a). This implies that the hyperfine field at the ^{75}As site from the ordered moments, B_{hf}, is along the c-axis. For $B_{ext} \parallel ab$, the ^{75}As line only shifts to the lower field side, as shown in Fig. 3.2(b), because the resonance condition is satisfied as $^{75}\gamma_n\sqrt{B_{ext}^2 + B_{hf}^2} = f$, hence requires smaller B_{ext} when $B_{hf} \neq 0$. These results confirm that the hyperfine field at the ^{75}As site is along the c-axis (Kitagawa et al., 2008, Fukazawa et al., 2008). The relatively sharp peaks at 77 K in the ordered state indicate that the ordered moments are commensurate with the lattice and the hyperfine field has only two discrete values, $B_{hf}^c = \pm$ 1.32 Tesla at 77 K. This is also consistent with an earlier report (Kitagawa et al., 2008).

We show the influence of Co doping on As lineshapes in the paramagnetic state above T_{SDW} for x = 0.02, 0.04, 0.082 in Fig. 3.1(b), (c) and (d), respectively. The lineshapes for the doped samples are very similar to the undoped case, except

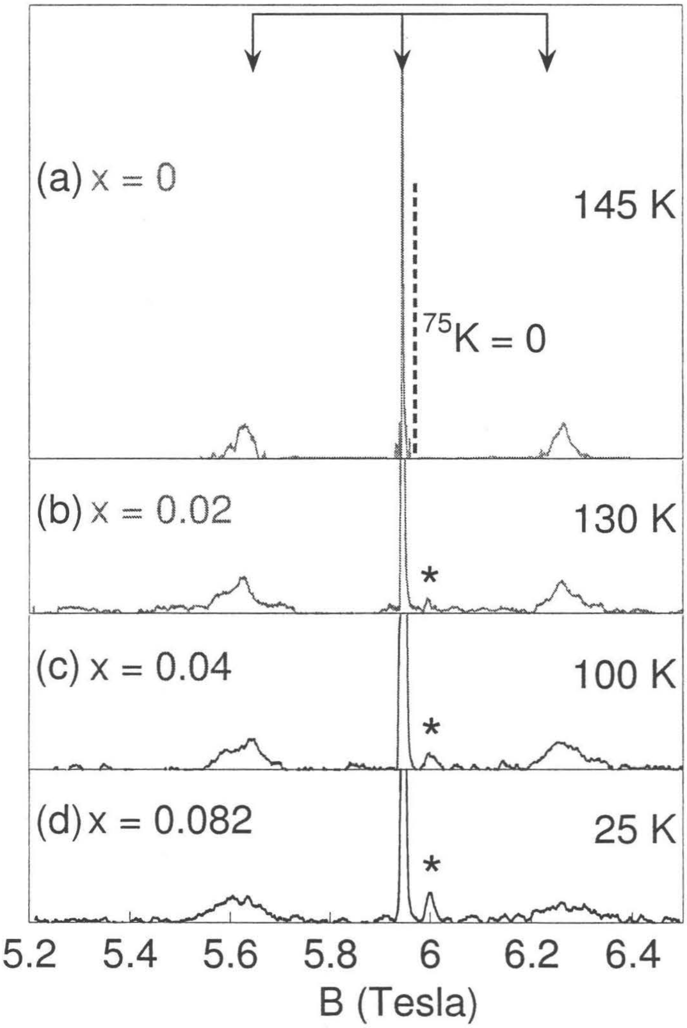

Figure 3.1 ^{75}As field swept NMR lineshapes of Ba(Fe$_{1-x}$Co$_x$)$_2$As$_2$ in the paramagnetic state, measured at f = 43.503 MHz with $B_{ext} \parallel c$, for (a) $x = 0$ at 145 K (above T_{SDW} = 135 K), (b) $x = 0.02$ at 130 K (above T_{SDW} = 100 K), (c) $x = 0.04$ at 100 K (above T_{SDW} = 66 K) and (d) $x = 0.082$ at 25 K (T_c = 22 K). Black arrows identify the three allowed transitions for m = -1, 0, 1. The vertical dashed line in (a) marks the location of the $m = 0$ central transition if $^{75}K = 0$. The $*$ marks the $m = 0$ central transition of the As(1) site, see main text for details.

that the satellite transitions become broader due to an additional distribution of ${}^{75}\nu_Q^c$ caused by the disorder in the lattice environment. We note that the magnitude of ${}^{75}\nu_Q^c$ is ~ 2.3 MHz in all compounds including the superconductor $Ba(Fe_{0.918}Co_{0.082})_2As_2$, and this value is smaller by a factor of ~ 5 than the case of $LaFeAsO_{1-\delta}$ (Mukuda et al., 2008). This is presumably because the ${}^{75}As$ ions are surrounded only by 2+ ions (Fe^{2+} and Ba^{2+}) in the present case, while ${}^{75}As$ ions in $LaFeAsO_{1-\delta}$ have La^{3+}

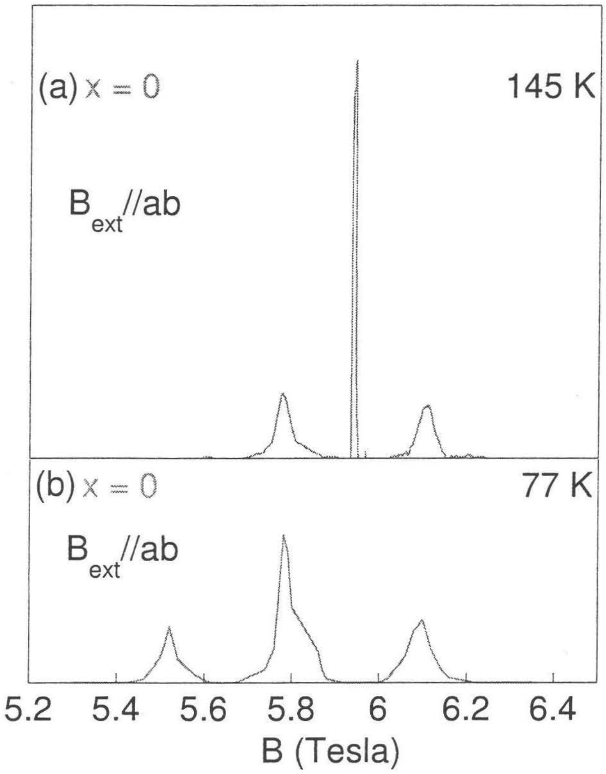

Figure 3.2 ${}^{75}As$ field swept NMR lineshapes of the undoped compound ($x = 0$) with $B_{ext} \parallel ab$, at (a) 145 K (in the paramagnetic state) and (b) 77 K ($<T_{SDW}$). Notice that the positions of the NMR lines in the paramagnetic state only shift from 145 K to 77 K because the hyperfine magnetic field B_{hf} is along the c-axis. If there is $B_{hf} \parallel ab$ component below T_{SDW}, the lineshape in (b) would split.

and O^{2-} ions nearby, in addition to Fe^{2+} ions; the charge disparity would enhance the EFG, hence ${}^{75}\nu_Q^c$ in $LaFeAsO_{1-\delta}$. Close inspection of Fig. 3.1 reveals that the linewidth and the position of the center transition changes slightly with Co doping. We can rule out the possibility that the broadening of the center transitions is from the second order quadrupole correction (Fig. 4.2), because ${}^{75}\nu_Q^c \sim 2.3$ MHz is nearly independent of Co concentrations. Thus these changes are primarily from the magnitude of the Knight shift and its distribution, the significance of which will be discussed in the next chapter.

We can also gain valuable insight on the effect of Co doping on the FeAs square lattice. If we assume that Co atoms substitute into Fe sites randomly in the $Fe_{1-x}Co_x$ with equal probability, the theoretical probabilities for each As atom to have N = 0 to 4 Co atoms at N.N. sites are $P(N) = C_4^N(x)^N(1-x)^{4-N}$. We tabulate the calculated probabilities for each As site, named as As(N) in Table. 3.1. With this definition, all the peaks observed for $BaFe_2As_2$ in Fig. 3.1(a) are from As(0) site.

Table 3.1 Theoretical probabilities for each As site with N Co atoms at N.N. sites in $Ba(Fe_{1-x}Co_x)_2As_2$ (x = 0, 0.02, 0.04, 0.082).

x of $Fe_{1-x}Co_x$	As(0) (N = 0)	As(1) (N = 1)	As(2) (N = 2)	As(3) (N = 3)	As(4) (N = 4)
0	100.0	–	–	–	–
0.02	92.24	7.53	0.23	0.003	0
0.04	84.93	14.16	0.88	0.02	0
0.082	71.64	24.92	3.25	0.19	0.004

For Co doped samples, however, we expect to observe separate NMR signals in different environment. We indeed observe a small additional peak for Co doped samples as marked by * in Fig. 3.1. The small peak is absent in the undoped compound, but its intensity grows with increasing Co concentration. We carefully measured the

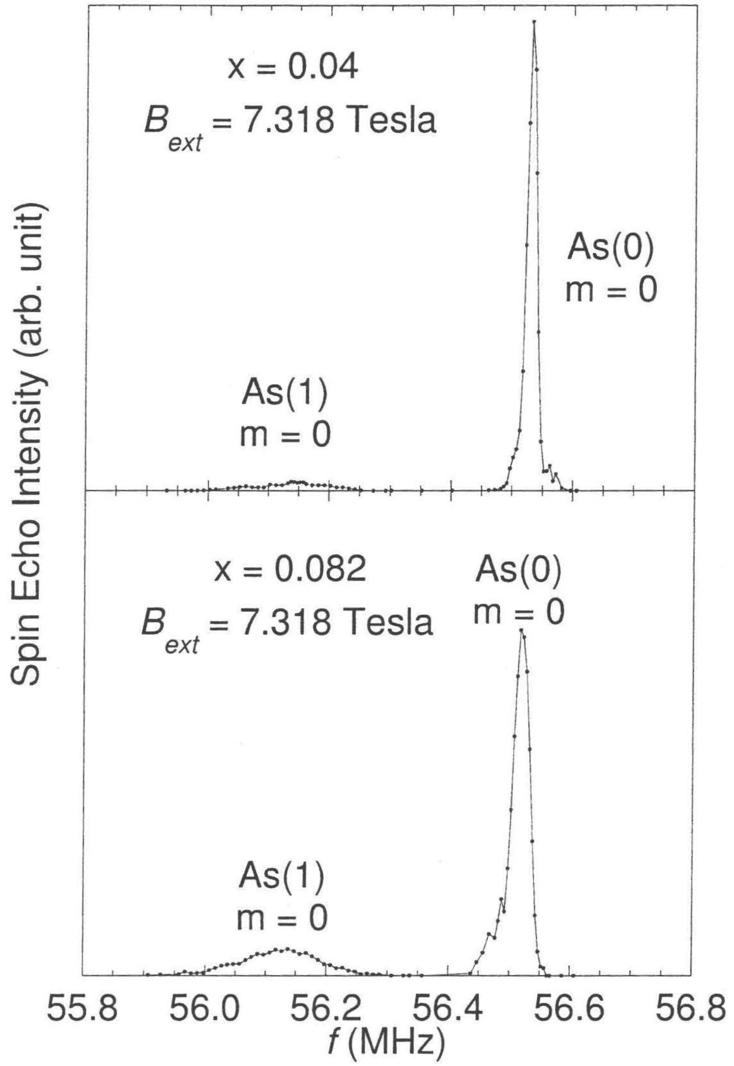

Figure 3.3 Spin echo intensity as a function of frequency measured at $B_{ext} = 7.318$ Tesla for the $m = 0$ central transition of As(0) and As(1) (marked by $*$ in Fig. 3.1) sites of $x = 0.04$ and 0.082 samples (The same As(1) peak appears on the right hand side of the As(0) peak in Fig. 3.1(c) and (d) because the lineshapes in Fig. 3.1 were measured as a function of magnetic field). The ratio of the integrated intensity between As(0) to As(1) is 85:12 for $x =$ 0.04 and 72:23 for $x = 0.082$, consistent with the theoretical calculations in Table 3.1.

spin echo intensity of the $m = 0$ central transition of the As(0) site and the $*$ peak for $x = 0.04$ and 0.082 samples, and present the results in Fig. 3.3. The integrated intensity ratio is 85:12 for $x = 0.04$ and 71:22 for $x = 0.082$ respectively. These ratios are very close to the theoretically expected values for As(0) to As(1) as shown in the 5th row in Table. 3.1. Therefore, we identify the peak marked by $*$ as the central transition from the As(1) site, which has one Co atom at N.N. sites. Unfortunately, the search for the $m = \pm 1$ satellite transitions of the As(1) site has not been successful for $x = 0.02$, 0.04 and 0.082. A possible reason behind the difficulty in observing the satellites is that for the As(1) site, with one Co^{2+} atom and three Fe^{2+} atoms at its N.N. sites, the disparity of the charge distribution is heavily enhanced, hence the EFG and its distribution must be large. Considering that the satellite peaks of the As(0) site are already broad and weak, the satellite peaks of the As(1) site might be even broader and weaker. This makes the measurement of satellite peaks very difficult for As(1). In fact, we confirmed that the large linewidth of As(1) central peak in $Ba(Fe_{0.918}Co_{0.082})_2As_2$ is inversely proportional to the external magnetic field. This implies that the quadrupole contribution $\nu_Q^z(2)$ is the dominant factor of the large linewidth. Furthermore, the actual Knight shift of the As(1) site is identical to that of the As(0) site after we subtract the second order quadrupole term $\nu_Q^z(2)$ as shown in Fig. 4.2(b). These results strongly suggest that the As(1) peak is split off from the As(0) peak due primarily to the structural effects. Therefore we will focus on the As(0) site in the following.

Next, we turn our attention to the ^{75}As lineshapes in the ordered state of the Co doped samples below T_{SDW}. We found that the lineshape is qualitatively different between the undoped and doped samples below T_{SDW} for $x = 0.02$ and 0.04, as shown in Fig. 3.4(b) and (c). Unexpectedly, the ^{75}As lines do not split in 2 % and 4 % Co doped samples. Instead, the ^{75}As NMR lines broaden, and become almost

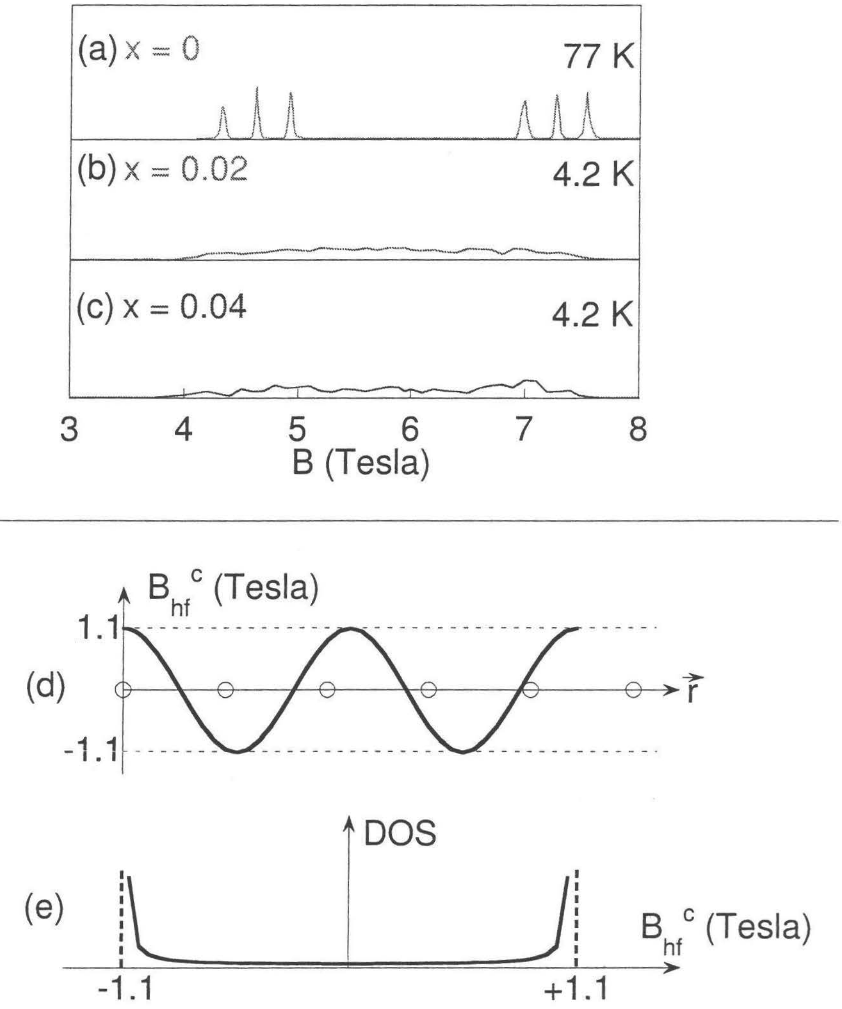

Figure 3.4 ^{75}As field swept NMR lineshapes of $\mathrm{Ba(Fe_{1-x}Co_x)_2As_2}$ in the SDW ordered state below T_{SDW}, measured at f = 43.503 MHz with $B_{ext} \parallel c$ for (a) $x = 0$ at 77 K, (b) $x = 0.02$, and (c) $x = 0.04$ at 4.2 K. Note that the trio of paramagnetic NMR lines shown in Fig. 3.1 split into two sets for x = 0, but only broaden for x = 0.02 and 0.04. (d) Schematic distribution of B^c_{hf} along the position vector $\vec{r}$ within the ab-plane for IC-SDW. (e) Schematic ^{75}As lineshape expected from (d).

featureless. The spin echo signal could be detected everywhere between 4 and 7.5 Tesla. This means that $|B^c_{hf}|$ at ^{75}As sites has a continuous distribution from 0 to $\lesssim$ 1.1 Tesla. The significance of the featureless lineshape and the distribution of $|B^c_{hf}|$ will be discussed in the next section together with the ^{59}Co NMR results.

3.2 ^{59}Co Lineshapes for $x = 0.02$ and 0.04

In Fig. 3.5 and Fig. 3.6, we present the typical field swept ^{59}Co lineshapes with $B_{ext} \parallel c$ or $B_{ext} \parallel ab$ for $Ba(Fe_{1-x}Co_x)_2As_2$ with $x = 0.02$ and 0.04. ^{59}Co has nuclear spin $= 7/2$ and nuclear gyromagnetic ratio $\gamma_n/2\pi = 10.054$ MHz/Tesla. One ^{59}Co site gives rise to seven transitions from $I_z = \frac{2m+1}{2}$ to $\frac{2m-1}{2}$ (where m = -3, -2, -1, 0, 1, 2, 3) in the paramagnetic state. Similar to the case of As sites, each Co atom may have N = 0 to 4 Co atoms at N.N. sites. If we assume that Co atoms substitute Fe atoms randomly with equal probability $x \times 100\%$, the probability for each Co atom to have N = 0 to 4 Co atoms at N.N. sites is given by $P(N) = C_4^N(x)^N(1-x)^{4-N}$. We tabulate the calculated probability for each case in Table. 3.2.

Table 3.2 Theoretical probabilities for each Co site with N Co atoms at N.N. sites in $Ba(Fe_{1-x}Co_x)_2As_2$ (x = 0, 0.02, 0.04, 0.082).

x of $Fe_{1-x}Co_x$	Co(0) (N = 0)	Co(1) (N = 1)	Co(2) (N = 2)	Co(3) (N = 3)	Co(4) (N = 4)
0	100.0	—	—	—	—
0.02	92.24	7.53	0.23	0.003	0
0.04	84.93	14.16	0.88	0.02	0
0.082	71.64	24.92	3.25	0.19	0.004

The probability for a Co site to have four Fe at N.N. sites is 92.2 % for x = 0.02 and 84.9 % for x = 0.04, respectively. Thus the Co NMR lineshape is dominated

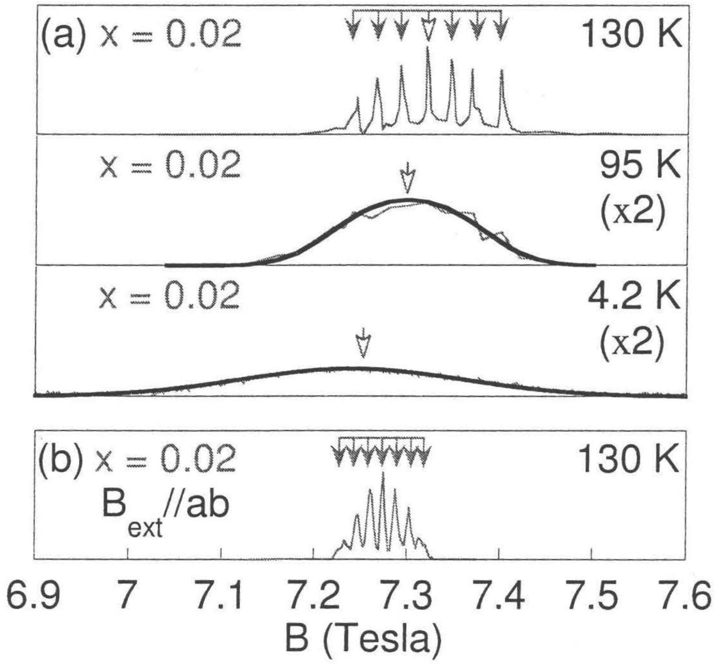

Figure 3.5 ^{59}Co field swept NMR lineshapes of Ba(Fe$_{1-x}$Co$_x$)$_2$As$_2$ measured at a fixed frequency of $f = 74.103$ MHz for $x = 0.02$. (a) B_{ext} was applied along the c-axis at 130 K (paramagnetic), 95 K and 4.2 K (SDW); The overall intensities in the SDW state have been amplified by a factor of 2 compared with that in the paramagnetic state. Solid curves represent a fit to the data using convoluted Gaussian peaks as described in the main text. (b) B_{ext} was applied within the ab-plane. Open arrows mark where T_1 was measured.

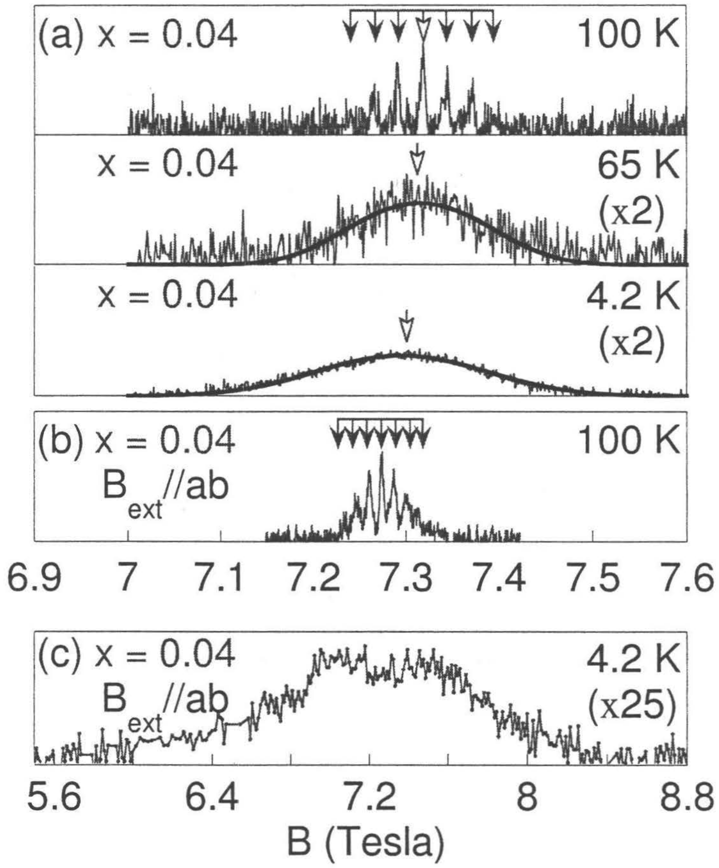

Figure 3.6 ^{59}Co field swept NMR lineshapes of $Ba(Fe_{1-x}Co_x)_2As_2$ measured at f = 74.103 MHz for x = 0.04. (a) B_{ext} was applied along the c-axis at 100 K (paramagnetic), 65 K and 4.2 K(SDW). The overall intensities in the SDW state have been amplified by a factor of 2 compared with that in the paramagnetic state. Solid curves represent a fit to the data using convoluted Gaussian peaks. (b) and (c) B_{ext} was applied within the ab-plane. Notice the scale of the horizontal axis in panel (c) is expanded to show the details clearly. The overall intensity in (c) has been amplified by 25 times compared with (b). Open arrows mark where T_1 were measured.

by NMR signals from the Co with zero N.N. Co (Co(0) site). As mentioned above, however, each Co site has seven allowed transitions. Therefore the paramagnetic Co NMR line splits into seven peaks separated by ${}^{59}\nu_Q^c$ (${}^{59}\nu_Q^{ab}$) when we apply the external magnetic field B_{ext} along the c (ab) axis. From Fig. 3.5(a) and Fig. 3.6(a), we estimate ${}^{59}\nu_Q^c \sim 0.26$ MHz for both $x = 0.02$ and 0.04. From Fig. 3.5(b) and Fig. 3.6(b), we also estimate ${}^{59}\nu_Q^{ab} \sim 0.13$ MHz, thus a symmetry parameter for the EFG tensor at the Co site is $\eta = 0$ for both x =0.02 and 0.04 within experimental uncertainties. $\eta = 0$ is consistent with the tetragonal symmetry of the crystal structure ($|\nu_Q^a| = |\nu_Q^b| = |\frac{1}{2}\nu_Q^c|$).

Below T_{SDW}, the ^{59}Co NMR lines become broader as shown in the second and third panels of Fig. 3.5(a) and Fig. 3.6(a); the seven discrete peaks caused by the quadrupole split are smeared out, and the whole NMR line becomes completely featureless at low temperatures. We observe no signature of residual sharp paramagnetic NMR peaks below T_{SDW}, hence all ^{59}Co nuclear spins are under the influence of magnetic ordering. The integrated intensity at 4.2 K corrected for the Boltzmann factor is unchanged between 100 K and 4.2 K, hence we observe all ^{59}Co nuclear spins at 4.2 K. This conservation of the total intensity rules out any possibility of phase separation or *macroscopic* inhomogeneity in the $x = 0.02$ and 0.04 samples. In other words, the successive phase transitions from paramagnetic to SDW to superconductivity are not caused by a macroscopic domain which remains paramagnetic below T_{SDW}. If that was the case, sharp paramagnetic NMR signals would be superposed on the broad lines below T_{SDW}.

Close inspection of the line positions in Fig. 3.5(a) and 3.6(b) reveals that the center of the broad line (as marked by open arrows) progressively shifts to the lower field side with decreasing temperature when we apply B_{ext} along the c-axis. For example, the central transition of $x = 0.02$ located at $B_{ext} \sim 7.320$ Tesla at 100 K shifts by 0.068 Tesla to $B_{resonance} = 7.252$ Tesla at 4.2 K, as shown in Fig.

3.5(a). Similarly, the central transition for $x = 0.04$ is at $B_{ext} \sim 7.318$ Tesla at 100 K, and shifts by 0.023 Tesla to $B_{resonance} = 7.295$ Tesla at 4.2 K, as shown in Fig. 3.6(a). These shifts of the center transitions imply that sizable hyperfine field B_{hf} has developed below T_{SDW} for both $x = 0.02$ and 0.04.

On the other hand, when B_{ext} is applied along the *ab*-plane instead, the ^{59}Co NMR lines for $x = 0.04$ split into two broad humps as shown in Fig. 3.6(c). We assume that $^{59}\nu_Q^{ab}$ will not change with temperature, and fit the two broad humps by two sets of seven Gaussian functions. Each set of the seven Gaussian functions represents seven quadrupole transitions of one Co site separated by $^{59}\nu_Q^{ab}$. The fit in Fig. 3.7 is reasonable. The separation between the center of the two humps is ~ 0.6 Tesla, which is much larger than the small shift, 0.023 Tesla, observed along $B_{ext} \parallel c$. This implies that the hyperfine field B_{hf} at the ^{59}Co site is primarily within the *ab*-plane. We emphasize, however, that our successful fit of the Co lineshape in Fig. 3.7 does not necessarily mean that the hyperfine magnetic field within the *ab*-plane is bi-modal with $B_{hf}^{ab} = \pm\ 0.3$ Tesla. Continuously distributed B_{hf}^{ab} between $|B_{hf}^{ab}| \sim 0$ to ~ 0.3 Tesla would also be consistent with the data. We have not been able to repeat the measurement of the $x = 0.02$ crystal with B_{ext} applied along the *ab*-plane due to the very limited ^{59}Co NMR signal intensity caused by the small size of the sample and the lower Co concentration.

We recall that ^{75}As lines below T_{SDW} are dramatically different between the undoped parent compound ($x = 0$) and lightly Co doped samples ($x = 0.02$, 0.04), i.e., ^{75}As lines exhibit bi-modal splitting for $x = 0$ but not for $x = 0.02$, 0.04 with $B_{ext} \parallel c$ as shown in Fig. 3.4. Combined with the Co NMR data, we conclude that the commensurate SDW (C-SDW) ground state observed for undoped $BaFe_2As_2$ is no longer the ground state of the $x = 0.02$ and 0.04 systems. Two possible scenarios exist. First, the ordered moments of lightly Co doped samples are incommensurate with the

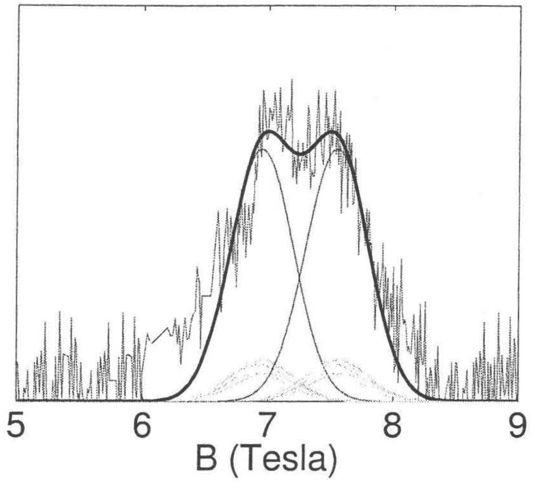

Figure 3.7 Convoluted Gaussian fit of the Co NMR line of 4 % Co doped sample at 4.2 K with $B_{ext} \parallel ab$. We assume that $^{59}\nu_Q^{ab}$ does not change with temperature. The thick solid line represents the fit. Two thin dotted lines represent two sets of the summation of seven Gaussian functions (dashed lines). Each dashed line is a Gaussian function representing a quadrupole peak separated by $^{59}\nu_Q^{ab}$.

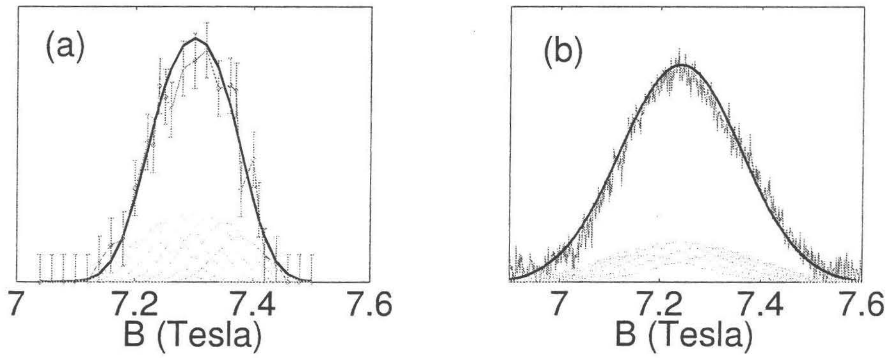

Figure 3.8 Convoluted Gaussian fit of the Co NMR line of 2 % Co doped sample at (a) 95 K and (b) 4.2 K with $B_{ext} \parallel c$ with temperature independent $^{59}\nu_Q^{c}$. The solid line represents the fit, which is a summation of the seven Gaussian functions. Each dashed line is a Gaussian function representing a quadrupole peak separated by $^{59}\nu_Q^{c}$.

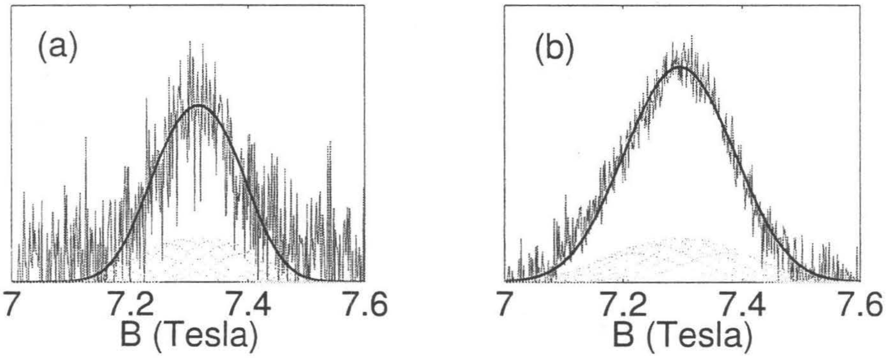

Figure 3.9 Convoluted Gaussian fit of the Co NMR line of the 4 % Co doped sample at (a) 65 K and (b) 4.2 K with $B_{ext} \parallel c$. We assume that $^{59}\nu_Q^c$ does not change with temperature. The solid line represents the fit, which is a summation of seven Gaussian functions. Each dashed line is a Gaussian function representing a quadrupole peak separated by $^{59}\nu_Q^c$.

lattice. The continuous distribution of $|B_{hf}|$ from 0 to $\sim$ 1.1 Tesla is consistent with an IC-SDW scenario. For example, if $B_{hf}^c = 1.1cos(\vec{Q}_{SDW} \cdot \vec{r})$, where $\vec{Q}_{SDW}$ is the SDW ordering vector and $\vec{r}$ is the position vector within the ab-plane, we expect to observe the ^{75}As lineshape as shown in Fig. 3.4(e). However, our results in Fig. 3.4(b) and (c) do not exhibit singularities in the ^{75}As lineshape at $|B_{hf}| = \sim 1.1$ Tesla expected for a clean IC-SDW system. The second possible scenario to explain the featureless lineshapes below T_{SDW} for lightly Co doped samples is that the spin structure is still commensurate, but there exists a continuous distribution of B_{hf}^{ab} from $|B_{hf}^{ab}| \sim 0$ to $\sim$ 1.1 Tesla. Our NMR results do not allow us to discern these two scenarios.

Next, we turn our attention to the temperature dependence of the ^{59}Co NMR line broadening below T_{SDW}. Our goal is to deduce information on the temperature dependence of the magnitude of the ordered moments. To achieve that goal, we fit the broad, featureless ^{59}Co NMR lineshapes with $B_{ext} \parallel c$ in Fig. 3.5 and 3.6 by assuming that the quadrupole splitting does not depend on temperature. We represent each quadrupole split transition by a Gaussian function, and broaden each peak by an identical Gaussian distribution of the hyperfine fields ΔB^c_{hf} below T_{SDW}. We show representative fits in Fig. 3.8 and Fig. 3.9. The fits are reasonable for both $x = 0.02$ and 0.04, and we deduce the Gaussian width ΔB^c_{hf} as a function of temperature. The results are summarized in Fig. 3.10. ΔB^c_{hf} continuously increases below T_{SDW} and finally saturates at base temperature for both $x = 0.02$ and 0.04. Also shown in Fig. 3.10 is the temperature dependence of $d\rho_{ab}/dT$, the temperature derivative of the in-plane resistivity data shown in Fig. 1.6. The minimum of $d\rho_{ab}/dT$ is observed

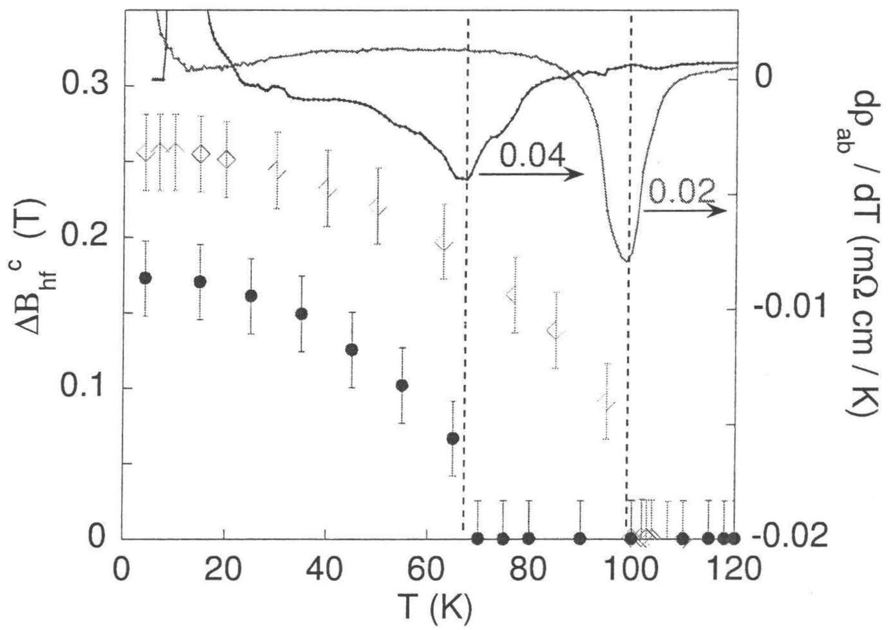

Figure 3.10 The temperature dependence of the magnetic broadening ΔB^c_{hf} of ^{59}Co NMR lines for $x = 0.02$ (◇) and $x = 0.04$(•). The temperature dependence of the derivative of ρ_{ab} for $x = 0.02$ and 0.04, $d\rho_{ab}/dT$, is also shown on the right axis. Dashed lines mark T_{SDW}, which is defined as the minimum of $d\rho_{ab}/dT$. ΔB^c_{hf} starts to increase below T_{SDW}, due to the growth of the ordered moment below T_{SDW}.

exactly at the onset temperature of the ^{59}Co NMR line broadening induced by the SDW ordering.

In Fig. 3.10, we notice that the magnitude of ΔB^{c}_{hf} for x = 0.02 is larger than that for x = 0.04. Since ΔB^{c}_{hf} is proportional to the typical magnitude of the ordered moments, μ_{eff}, this implies that Co doping suppresses the magnitude of μ_{eff}. Additional pieces of evidence support this argument. First, the static hyperfine field B_{hf} = ± 1.32 Tesla at ^{75}As site in the parent compound is suppressed to $|B_{hf}|$ = 0 ~ 1.1 Tesla for lightly Co doped samples (Fig. 3.4). Furthermore, the overall shift of the ^{59}Co lineshapes to lower magnetic field side below T_{SDW} for x = 0.04 (i.e., 0.023 Tesla at 4.2 K in Fig. 3.6) is smaller than that for x = 0.02 (i.e., 0.068 Tesla at 4.2 K in Fig. 3.5).

We can roughly estimate the magnitude of the ordered moments in x = 0.02 and 0.04 as follows. Using f = 74.103 MHz $= \gamma_n B_{resonance} = \sqrt{(B_{ext})^2 + (B^{ab}_{hf})^2}$, we estimate the hyperfine magnetic field B^{ab}_{hf} = 1.0 Tesla and 0.58 Tesla for x = 0.02 and 0.04 respectively. Since $B^{ab}_{hf} = A_{hf} \cdot \mu_{eff}$, and $A_{hf} = 1.6 \pm 0.4$ Tesla/μ_B from the ^{59}K vs. χ plot (chapter 4), we obtain μ_{eff} = 0.55 ± 0.1 μ_B for x = 0.02 and 0.3 ± 0.1 μ_B for x = 0.04, respectively. Neutron scattering experiments showed that μ_{eff} = 0.35 ± 0.1 μ_B for x = 0.025 (Lester et al., 2009), and μ_{eff} = 0.2 ± 0.1 μ_B for x = 0.047 (Pratt et al., 2009). These results are in good agreement with ours.

3.3 ^{59}Co Lineshape for x = 0.082

We present the field swept ^{59}Co NMR lineshape for the optimally doped superconducting sample x = 0.082 with $B_{ext} \parallel c$ or $B_{ext} \parallel ab$ at f = 74.103 MHz in Fig. 3.11. Theoretically, depending on the number of Co atoms occupying the N.N. Fe sites of the observed ^{59}Co site, we would expect up to five different types of Co sites with different probabilities as listed in Table. 3.2. the results in Fig. 3.11(a) show that we observed at least three Co sites with $B_{ext} \parallel c$. We use different types of arrows to identify three different Co sites: 7 solid arrows mark the Co(0) site, which dominates the total intensity; 2 dotted arrows mark $m = \pm 3$ transitions for the Co(1) site; the dashed arrow marks the possible m = -1 transition for the Co(2) site.

Table 3.3 Parameters for Co sites in the superconductor $Ba(Fe_{0.918}Co_{0.082})_2As_2$.

	Co(0)	Co(1)	Co(2)	Co(3)	Co(4)
N.N. Co Ions (No.)	0	1	2	3	4
Theory (%)	71.64	24.92	3.25	0.19	0.004
Experimental (%)	67±5	26±5	7±5	0	0
$^{59}\nu_Q$ (Tesla)	0.026	0.034	0.015	N/A	N/A
^{59}K (%)	0.714	0.714	0.714	N/A	N/A

We simulate the ^{59}Co NMR lineshape by taking into account these 3 dominant Co sites (N = 0, 1, 2). The ^{59}Co NMR line of each Co site consists of 7 quadrupole split peaks, and we approximate the latter with Gaussian functions. The simulated result is shown in Fig. 3.12 with deconvolution into N = 0, 1, 2 sites. We find that the summation of the 3 sets of 7 Gaussian functions reproduce the experimental lineshape well. We list the fitting parameters in Table. 3.3 for comparison. The experimental values are consistent with the theoretical calculations within the uncertainties. $^{59}\nu_Q^c$ of the Co(0) site (N = 0) in $Ba(Fe_{0.918}Co_{0.082})_2As_2$ is $\sim$ 0.261 MHz ($= \gamma_n \times 0.026$ Tesla), which is identical to $^{59}\nu_Q^c$ of Co(0) sites in 2 % and 4 % Co doped compounds.

Finally, we present the field swept ^{59}Co NMR lineshape with the external magnetic field B_{ext} applied within the *ab*-plane ($B_{ext} \parallel ab$) in Fig. 3.11(d). Unlike the case of $B_{ext} \parallel c$, we can resolve only the Co(0) site, as marked by 7 black arrows because the quadrupole splitting is smaller for $B_{ext} \parallel ab$; $^{59}\nu_Q^{ab}$ is estimated to be $\sim$ 0.013 Tesla $\sim$ 0.131 MHz for Co(0) sites. Thus the symmetry parameter of ν_Q, $\eta \sim$

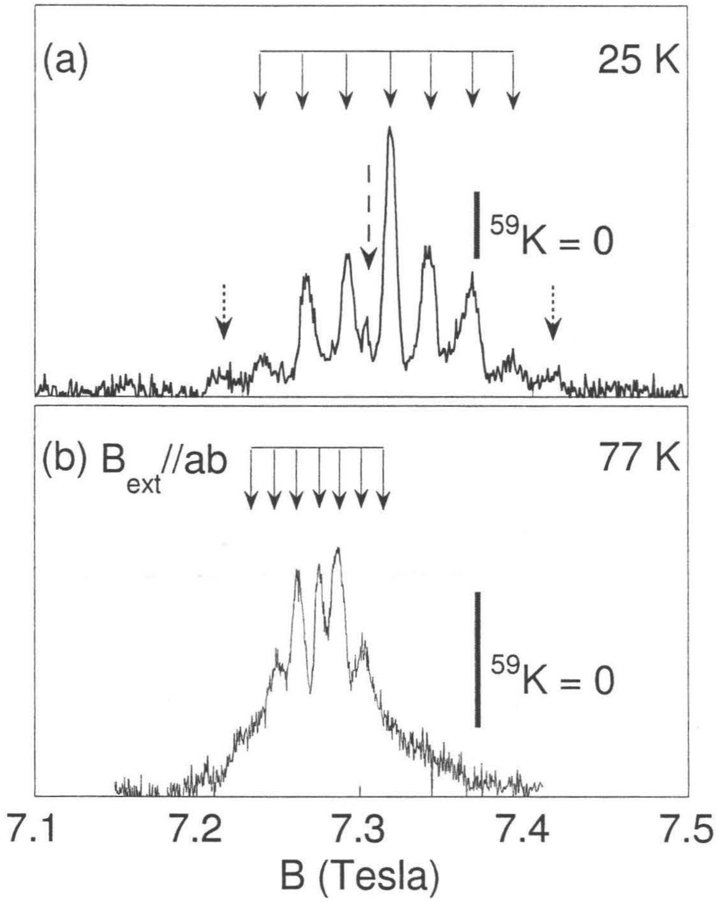

Figure 3.11 (a): ^{59}Co field swept NMR lineshape of the superconductor $Ba(Fe_{0.918}Co_{0.082})_2As_2$ measured at $f = 74.103$ MHz observed with $B_{ext} \parallel c$. Solid, dotted and dashed arrows identify the Co sites with N = 0, 1, and 2 Co atoms at N.N. sites, respectively (see main text). Vertical thick line marks the location of the $m = 0$ central transition if $^{59}K = 0$. (b): Field swept ^{59}Co NMR lineshape observed at 77 K ($B_{ext} \parallel ab$). Black arrows identify the 7 transitions of the Co(0) site (N = 0). The vertical thick line marks the location of the $m = 0$ central transition if $^{59}K = 0$.

0. This is again consistent with the high symmetry of the tetragonal phase, where Co atoms are located at the geometrical center of four N.N. Fe atoms.

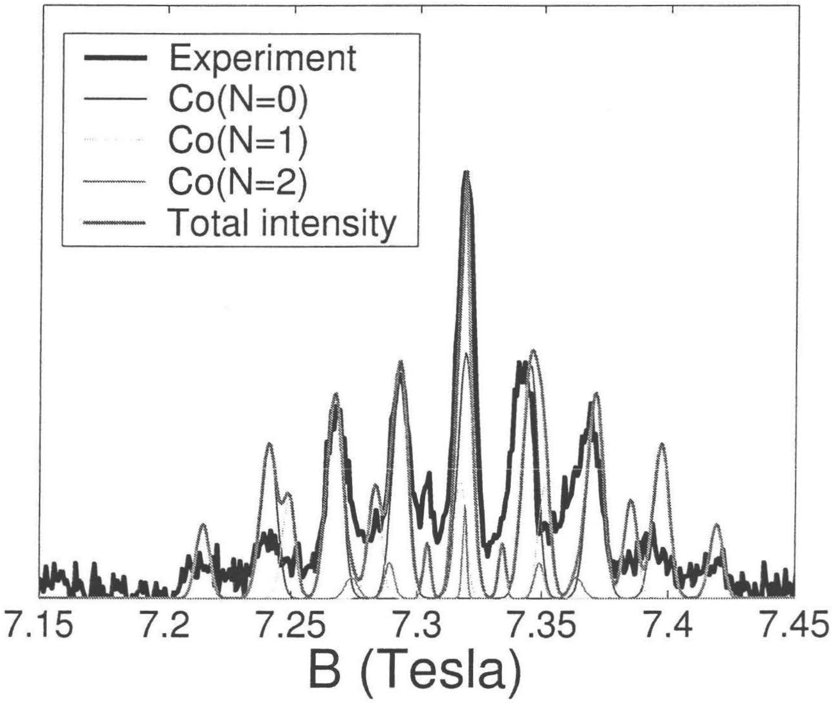

Figure 3.12 Deconvolution of the ^{59}Co NMR lineshape of the superconductor $Ba(Fe_{0.918}Co_{0.082})_2As_2$ by taking into account the presence of three dominant Co sites, Co(0), Co(1) and Co(2) sites. The black line is the experimental data; The red line is the summation of the three sets of deconvoluted line for N = 0 (blue), 1 (green), 2 (magenta). The parameter values used for deconvolution are summarized in Table 3.3.

3.4 Summary

We investigated the ^{75}As and ^{59}Co NMR lineshapes of the $Ba(Fe_{1-x}Co_x)_2As_2$ ($x = 0$, 0.02, 0.04 and 0.082) compound in both paramagnetic and SDW ordered states. We showed that only the As(0) site exists in the parent compound $BaFe_2As_2$. The lineshape of As(0) site changes little with Co doping, and each transition becomes broader with increasing Co concentration. As(1) sites emerge with Co doping, and the intensity increases with increasing Co concentration. We observed one Co site in the samples with $x = 0.02$ and 0.04, but identified three Co sites in the paramagnetic state of $x = 0.082$, in agreement with theoretical expectations. Below T_{SDW}, the ^{75}As line for $x = 0$ splits into two sets due to discrete values of hyperfine field $B^c_{hf} = \pm$ 1.32 Tesla. However the ^{75}As line becomes broad and featureless for $x = 0.02$ and 0.04 because of the wide distribution of B^c_{hf}. Furthermore, ^{59}Co lines become broad and featureless below T_{SDW} for $x = 0.02$ and 0.04 as well. The featureless lineshapes for both ^{75}As and ^{59}Co below T_{SDW} indicate that as little as 2 % Co doping transforms the nature of the ground state from the commensurate spin density wave ordered state observed in the parent compound $BaFe_2As_2$ to a different state, most likely an incommensurate spin density wave ordered state. Note that we cannot rule out the possibility that the spin structure is still governed by a commensurate spin density wave with a large distribution of μ_{eff}.

Chapter 4

Knight Shifts

4.1 ^{75}K of $\mathbf{Ba(Fe_{1-x}Co_x)_2As_2}$

We presented the ^{75}As lineshapes of $Ba(Fe_{1-x}Co_x)_2As_2$ for various concentration x with $B_{ext} \parallel c$ in Fig. 3.1. We observed three transitions of the As(0) site in all samples, but only the central transition ($m = 0$) of As(1) site in the Co doped samples. It is straightforward to deduce the temperature dependence of ^{75}K from the position of the central transition. Using Eq. 2.2,

$$f = \gamma_n B_{ext}(1 + K) + \nu_Q^c(2) = f_0(1 + K) + \nu_Q^c(2), \tag{4.1}$$

where $f \sim 43.5$ MHz is the NMR resonance frequency, γ_n is the nuclear gyromagnetic ratio, and B_{ext} is the external magnetic field applied along the c-axis where the $m =$ 0 central transition occurs. $f_0 = \gamma_n B_{ext}$ is the resonance frequency for a bare nucleus. We denote the superscript "z" in eq. 2.2 as "c", because the principal axis of the ν_Q tensor coincides with the crystalline c-axis. $\nu_Q^c(2)$ is the second order perturbation from the nuclear quadrupole interaction, and inversely proportional to B_{ext}.

In Fig. 4.1, we present the typical ^{75}As NMR lineshapes of the central transition ($m = 0$) of the As(0) site at 175 K obtained by FFT (Fast Fourier Transform) of the spin echo envelope measured in a fixed magetic field of $B_{ext} \sim 7.7$ Tesla applied along the crystalline c-axis. These peaks are the same ones as the $m = 0$ central transitions in Fig. 3.1 but on an expanded scale. For clarity, we also converted the horizontal axis of the NMR resonance frequency f to the apparent NMR Knight shift,

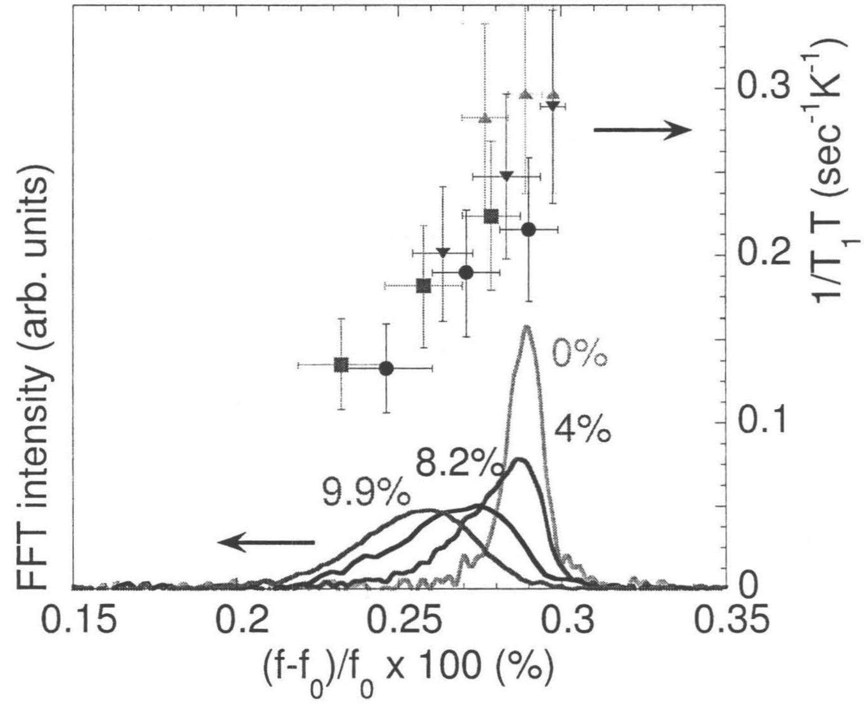

Figure 4.1 Representative ^{75}As NMR lineshapes obtained by FFT at 175 K. We converted the horizontal frequency axis to the apparent Knight shift, $(f - f_0)/f_0$. Also plotted is $1/T_1T$ measured at various points within each FFT line. The horizontal bars specify the range of $(f - f_0)/f_0$ in which the FFT intensity was integrated for $1/T_1T$ measurements.

$(f - f_0)/f_0$. We can see from the figure that the NMR line for $x = 0$ is very sharp and nearly symmetrical, and the linewidth at the half maximum is only $\sim$ 0.018 %, or equivalently, $\sim$ 8 KHz. With increasing Co concentrations, the NMR line becomes broader and tails toward the lower frequency side. The NMR line is rather asymmetric for $x = 0.04$ and 0.082.

Eq. 4.1 indicates that we need to subtract the contribution of $\nu_Q^c(2)$ to obtain the actual Knight shift. By far, the most reliable method to separate the effect of $\nu_Q^c(2)$ is to measure the apparent Knight shift, $(f - f_0)/f_0$, for several different values of magnetic field B_{ext}. Then we use the fact that the contribution of the second order perturbation is inversely proportional to the Zeeman term, hence $\nu_Q^c(2) \propto 1/\mathrm{B}_{ext}$. This means that $(f - f_0)/f_0 = K + \nu_Q^c(2)/\gamma_n B_{ext} \rightarrow K$ in the limit of large B_{ext} (Takigawa et al., 1989). A plot of $(f - f_0)/f_0$ vs. $1/B_{ext}^2$ gives rise to a straight line, and the extrapolation to $1/B_{ext}^2 = 0$ gives the actual K.

We plot $(f - f_0)/f_0$ vs. $1/B_{ext}^2$ of the As(0) site of $x = 0.04$ in Fig. 4.2(a), and As(0) and As(1) sites of $x = 0.082$ in Fig. 4.2(b). The slope of the linear fit for As(0) site is close to zero for both $x = 0.04$ and 0.082. This implies that the effect of $\nu_Q^c(2)$ to K is negligibly small. Therefore, the apparent Knight shift $(f - f_0)/f_0$ of As(0) site is the actual Knight shift K. On the other hand, the effect of $\nu_Q^c(2)$ is quite large for As(1) site at $B_{ext} \sim 6.5$ Tesla; the apparent shift $(f - f_0)/f_0$ is not equal to K. However, by extrapolating the data in Fig. 4.2(b) linearly to the high field limit, $1/B_{ext}^2 = 0$, we find that the actual K of the As(1) site is nearly identical to that of As(0) site within uncertainties. This means that the splitting of the As(0) and As(1) lines is not caused by site-to-site variations of the Knight shift K, but by the structural effects through $\nu_Q^c(2)$. Accordingly, we will focus our attention on K of the As(0) site.

The systematic line broadening of the central NMR peak with doping in Fig.

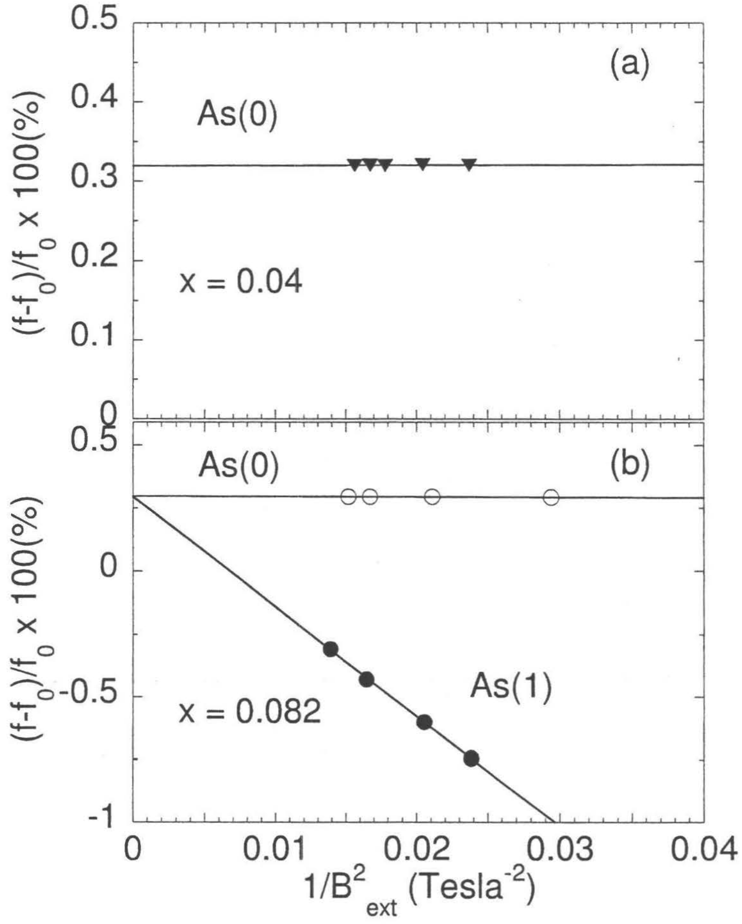

Figure 4.2 Apparent Knight shift $(f - f_0)/f_0$, plotted as a function of $1/B_{ext}^2$ for (a) $x = 0.04$ and (b) 0.082 at 295 K. The extrapolation to $1/B_{ext}^2 = 0$ gives the actual K. The effect of $\nu_Q^c(2)$ for As(0) site is negligibly small for both $x = 0.04$ and 0.082. The effect of $\nu_Q^c(2)$ is the dominant cause for the apparent NMR frequency shift $(f - f_0)/f_0$ at $B_{ext} \sim 6.5$ Tesla for the As(1) site of $x = 0.082$. However, notice that the actual $K = 0.29 \pm 0.10$ % for the As(1) site is nearly identical to $K = 0.298$ % observed for the As(0) site.

4.1 implies the presence of a distribution of ^{75}K. For example, some parts of the $x = 0.082$ sample have ^{75}K as large (small) as that of the $x = 0.04$ ($x = 0.099$) sample, i.e. the local electronic properties are inherently inhomogeneous at a microscopic level. We emphasize that one cannot attribute the present finding to macroscopic inhomogeneity of the Co concentrations. As shown in Fig. 1.6, the electrical resistivity ρ_{ab} is very sensitive to phase transitions at T_{SDW} and T_c. If the $x = 0.082$ crystal had a

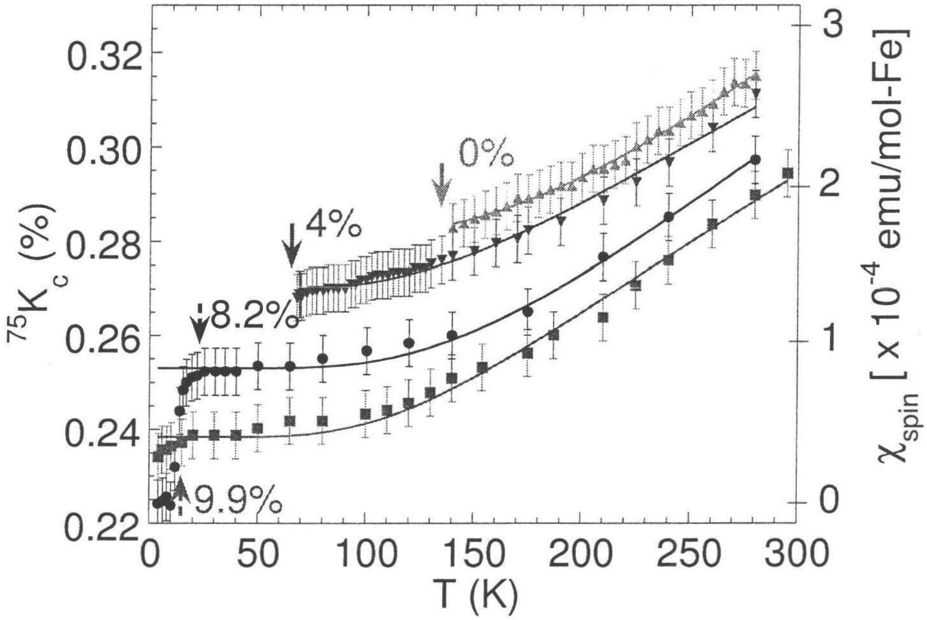

Figure 4.3 The center of gravity of the ^{75}As NMR Knight shift K measured along the crystalline c-axis. $K = 0.224$ % corresponds to the background arising from the chemical shift K_{chem} for $x = 0.082$. The conversion to spin susceptibility χ_s based on Eq. 4.2 is shown on the right vertical axis. Vertical solid and dashed arrows mark T_{SDW} and T_c, respectively. Solid curves are a fit to an activation formula with $\Delta_{PG}/k_B = 711$ K ($x = 0$), 570 K ($x = 0.04$), 520 K ($x = 0.082$), and 490 K ($x = 0.099$).

macroscopic domain with Co 4 % doping, for example, we would observe an additional SDW anomaly at ~ 66 K in the ρ_{ab} data. Therefore, the distribution of ^{75}K should be attributed to microscopic inhomogeneity of the doped electron concentration. A very similar situation was encountered in the case of the hole-doped high T_c cuprate $La_{2-x}Sr_xCuO_4$ (Singer et al., 2002, 2005).

Since the NMR Knight shift for the Co doped samples has a sizable distribution, we define the Knight shift at the center of gravity of each line instead of the apparent peak position. We summarize the T and x dependence of the center of gravity of K in Fig. 4.3. We can clearly see from the figure that the T dependence of ^{75}K is qualitatively similar in the paramagenetic state of all samples from the undoped SDW system ($x = 0$) to the slightly overdoped superconductor ($x = 0.099$); ^{75}K decreases almost linearly below 300 K, and then begins to level off below ~ 100 K. ^{75}K is almost temperature independent near T_c in the superconducting samples with $x = 0.082$ and 0.099, but decreases abruptly below $T_c(7.7 \text{ Tesla}) = 16$ K for $x = 0.082$. Furthermore, we notice that ^{75}K are continuously suppressed with Co doping from $x = 0$ to $x = 0.099$.

4.2 ^{75}K vs. χ Plot

In order to understand the significance of the suppression of ^{75}K by Co doping, we will have to use the knowledge introduced in chapter 2. We have shown that the Knight shift ^{75}K consists of two separate contributions, K_s and K_{chem}. K_s is the paramagnetic spin shift and proportional to the local spin susceptibility, χ_s, as defined in Eq. 2.8. We rewrite it here for convenience,

$$K_s = \frac{A_{hf}(q=0)}{N_A \mu_B} \chi_s, \tag{4.2}$$

where $A_{hf}(q = 0)$ is the hyperfine coupling between the nuclear spin and the electron spin at wave vector $q = 0$, N_A is Avogadro's number, μ_B is the Bohr magneton, χ_s is the local spin susceptibility, and A_{hf} is the hyperfine coupling constant along the c-axis between the observed ^{75}As nuclear spin and electron spins. K_{chem} is the temperature-independent chemical shift, and is not related to χ_s.

We present an example of the ^{75}K vs. χ analysis for the $x = 0.04$ sample in Fig. 4.4. We compare the magnetic susceptibility χ measured by SQUID and ^{75}K in Fig. 4.4(a). χ displays the same temperature dependence as ^{75}K above $T_{SDW} = 66$ K, thus the ^{75}K vs. χ plot in Fig. 4.4(b) yields a straight line. The slope of the linear fit in Fig. 4.4(b) is the hyperfine coupling A_{hf}, which is $\sim 20 \pm 4$ kOe/μ_B. This value is comparable to $A_{hf} = 18.8$ kOe/μ_B of the parent compound $BaFe_2As_2$ (Kitagawa et al., 2008). We repeated the ^{75}K vs. χ analysis for $x = 0.02$ and 0.082 as well, and plot the results in Fig. 4.4(b). Our results indicate that the hyperfine coupling A_{hf} is identical within experimental uncertainties for $x = 0.02$, 0.04 and 0.082. We also note that the ^{75}K vs. χ plots for three concentrations are superposed on top of each other. This implies that the chemical shift K_{chem} is nearly concentration independent as well, although we can not completely rule out the possibility that both A_{hf} and $^{75}K_{chem}$ changes slightly with Co concentration. We tentatively assume $^{75}K_{chem} = 0.224$ % along the c-axis for all compounds from the measurement at 4.2 K in the superconducting state below T_c of the $x = 0.082$ sample. We note that this is equivalent to assume that χ_s diminishes to zero at 4.2 K (see Fig. 4.11).

4.3 Implications of the T and x dependences of χ_s

We already showed that hyperfine coupling $A_{hf} \sim 20 \pm 4$ kOe/μ_B is nearly independent of the Co concentrations. If we assume that $^{75}K_{chem} = 0.224\%$ is identical

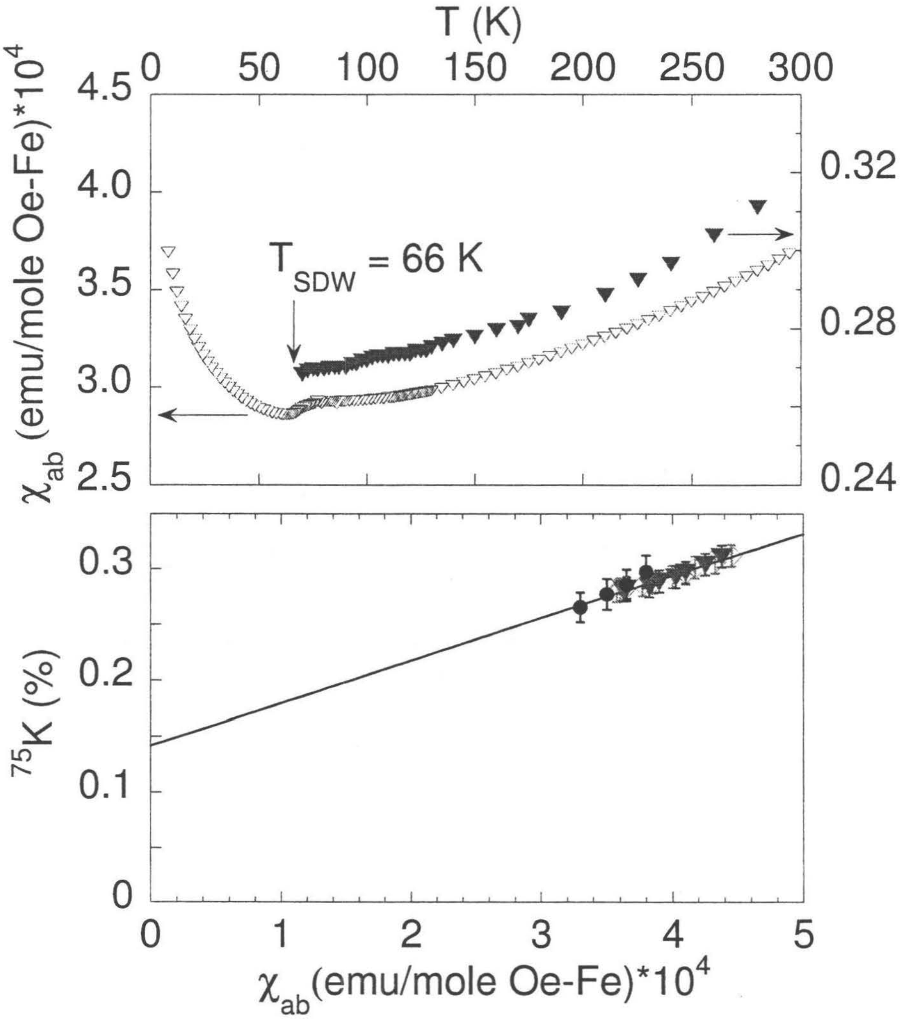

Figure 4.4 (a) Left axis: the bulk magnetic susceptibility χ_{ab} of $x = 0.04$ sample measured by SQUID with $B_{ext} = 1$ Tesla applied along the ab-plane (T-dependence of χ_{ab} is identical to that of χ_c (Wang et al., 2009a), hence we can use χ_{ab}); right axis: $^{75}K_c$. (b) $^{75}K_c$ vs. χ_{ab} plot for $x = 0.02$ ($\diamond$), 0.04 ($\blacktriangledown$), 0.082 ($\bullet$). Solid line is a linear fit.

for all samples with different Co concentration below $x = 0.099$, the suppression of $^{75}K_c$ with increasing Co concentrations may be attributed to that of the spin part, $^{75}K_s$. We convert the values of $^{75}K_s$ to χ_s according to Eq. (4.2), and show χ_s in the right axis in Fig. 4.3. Notice that the origin on the right axis, $\chi_s = 0$, is matched with the temperature independent background contribution $^{75}K_{chem} = 0.224$ %. We can see that a change of the spin contribution to the Knight shift by the amount of $\Delta K_s = 0.0339$ % corresponds to that of $\chi_s = 1 \times 10^{-4}$ emu/mol-Fe along the c-axis.

Since the undoped parent compound exhibits antiferromagnetic long-range order (AFLRO) below $T_{SDW} = 135$ K, it is natural to speculate that the growth of antiferromagnetic short-range order (AFSRO) suppresses χ_s with decreasing T toward T_{SDW} for $x = 0$, 0.02 and 0.04. However, AFSRO alone can't explain the systematic suppression of χ_s with increasing Co concentration, because χ_s is even smaller for the $x = 0.082$ and 0.099 samples which do not show AFLRO. In other words, if we attribute AFSRO as the only mechanism controlling the T and x dependencies of χ_s in $\mathrm{Ba(Fe_{1-x}Co_x)_2As_2}$, we would be led to an unphysical conclusion that the antiferromagnetic spin-spin correlation is stronger in the Co doped superconducting phase than in the undoped phase with AFLRO.

While AFSRO is very likely to play a significant role in controlling the behavior of χ_s, there must be an additional mechanism which suppresses χ_s with decreasing T and increasing x. We note that we can fit the temperature dependence of K by assuming an empirical activation formula, $K = A + B \times exp(-\Delta_{PG}/k_B T)$, where A and B are constants. The best fit yields $\Delta_{PG}/k_B \simeq 710$ K, 570 K, 520 K, and 490 K for $x = 0$, 0.04, 0.082, and 0.099, as shown by the solid lines in the Fig. 4.3. The fits are reasonably good for all samples with different Co concentrations. We recall that for $\mathrm{LaFeAsO_{1-x}F_x}$, an analogous fit of K yields $\Delta_{PG}/k_B \sim 160$ K for $x \geqslant 0.10$, and this was interpreted as spin pseudo-gap behavior (Imai et al., 2008, Nakai et al., 2008). Spin pseudo-gap behavior has been suggested also for high T_c cuprates (Takigawa et al., 1991, Ishida et al., 1998, Johnston, 1989, Timusk and Statt, 1999). We reproduce the Knight shift measured at ^{63}Cu and ^{17}O sites for the underdoped $YBa_2Cu_3O_{6.63}$ (T_c = 62 K) (Takigawa et al., 1991) in Fig. 4.5, and the Knight shift measured at ^{63}Cu sites for the underdoped (T_c = 79 K) and the overdoped (T_c = 77.3 K) $Bi_2Sr_2CaCu_2O_{8+\delta}$ (Ishida et al., 1998) in Fig. 4.6. For both $YBa_2Cu_3O_{6.63}$ and $Bi_2Sr_2CaCu_2O_{8+\delta}$, Knight shift in the underdoped region continuously decreases below ~300 K down to T_c. This type of behavior is interpreted as the evidence for the spin pseudo-gap behavior in high T_c cuprates. The mechanism behind this behavior is still under intense debate. In the pseudo-gap regime, $^{17,63}1/T_1T$ also decrease with temperature below the characteristic pseudo-gap temperature, T^*.

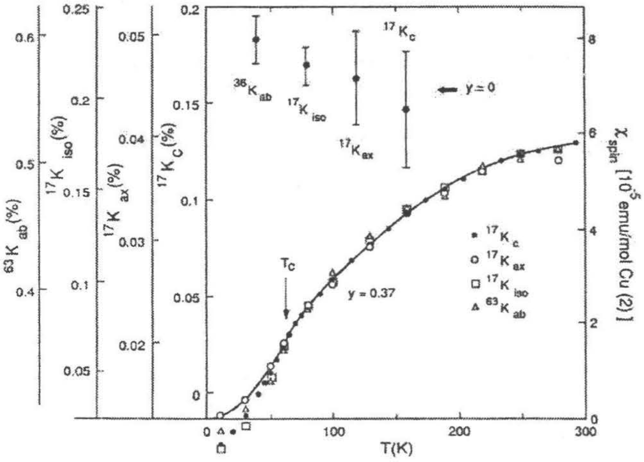

Figure 4.5 T dependence of ^{63}Cu and ^{17}O Knight shift for $YBa_2Cu_3O_{6.63}$ (T_c = 62 K) with different vertical scales and origins (Takigawa et al., 1991).

Our present results for $Ba(Fe_{1-x}Co_x)_2As_2$ compounds indicate that analogous spin pseudo-gap behavior may exist in a broad range of Co concentrations. We cannot definitely conclude that Δ_{PG}/k_B decreases systematically with increasing~ T^2. Co

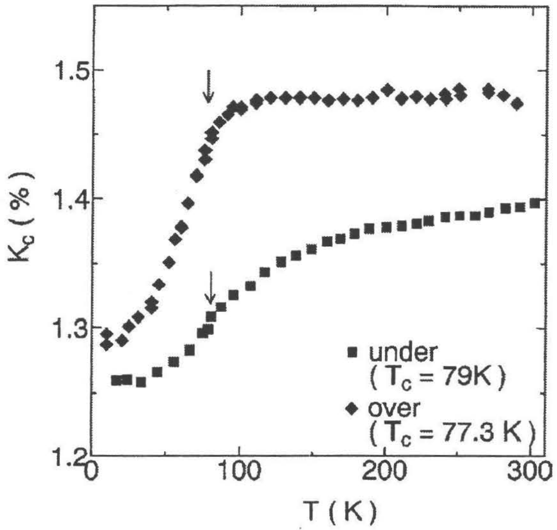

Figure 4.6 T dependence of ^{63}Cu Knight shift with $B_{ext} \parallel c$ for the underdoped and the overdoped $Bi_2Sr_2CaCu_2O_{8+\delta}$ (Ishida et al., 1998).

concentration because the fit is extremely sensitive to the choice of the constant term A, and the uncertainty of Δ_{PG} is as large as $\sim$ 30 %. However, we notice that in the $x = 0.082$ superconducting sample, χ_s becomes constant below $\sim$ 100 K after χ_s is suppressed. We recall that ρ_{ab} shows a T-linear behavior in the temperature regime below $\sim$ 100 K, as initially reported for $x = 0.082$ (Sefat et al., 2008b, Ahilan et al., 2008a). That is, the high T_c superconductivity of iron-pnictides arises from a novel electronic state with $\chi_s \sim$ constant and $\rho_{ab} \sim$ T after χ_s is suppressed. This is not consistent with a canonical Fermi-liquid behavior, where ρ

4.4 ^{59}K of $Ba(Fe_{1-x}Co_x)_2As_2$ for $x = 0.02, 0.04, 0.082$

In Fig. 4.7, we present the temperature dependence of the static spin susceptibility, χ_s, for $x = 0.02$, 0.04 and 0.082 as measured by ^{59}Co NMR Knight shift, ^{59}K

with $B_{ext} \parallel c$. Our results indicate that χ_s gradually decreases below $\sim$ 300 K, and begins to level off below $\sim$ 100 K. This behavior is consistent with that of χ_s deduced by ^{75}As, i.e. spin pseudo-gap behavior. Unlike the very sharp ^{75}As central peaks, the ^{59}Co central transition is broad, as shown in Fig. 3.5, 3.6 and 3.11. Accordingly, the experimental uncertainties of ^{59}K are very large, and did not allow us to determine the concentration dependence of ^{59}K accurately. The error bars in the inset of Fig. 4.7 represent the full width at half maximum (FWHM) of ^{59}Co line at 295K.

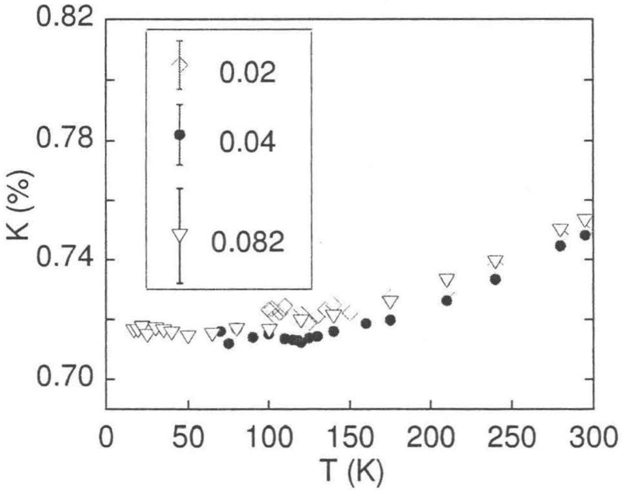

Figure 4.7 ^{59}Co Knight shift for $x = 0.02$ ($\diamond$), 0.04 ($\bullet$) and 0.082 ($\triangledown$). The error bars in the legend represent the FWHM (Full Width at Half Maximum) of Co center transition at 295 K.

4.5 ^{59}K vs. χ Plot

We plot ^{59}K vs. χ for x = 0.02, 0.04 and 0.082 in Fig. 4.8 with a linear fit. The slope of the solid line represents the hyperfine coupling constant $^{59}A_{hf}$ between the Co nuclear spin and the electrons. We discussed in Chapter 2 that $^{59}A_{hf}$ has two contributions: one is the on-site hyperfine coupling $A_{on-site}$, which is between

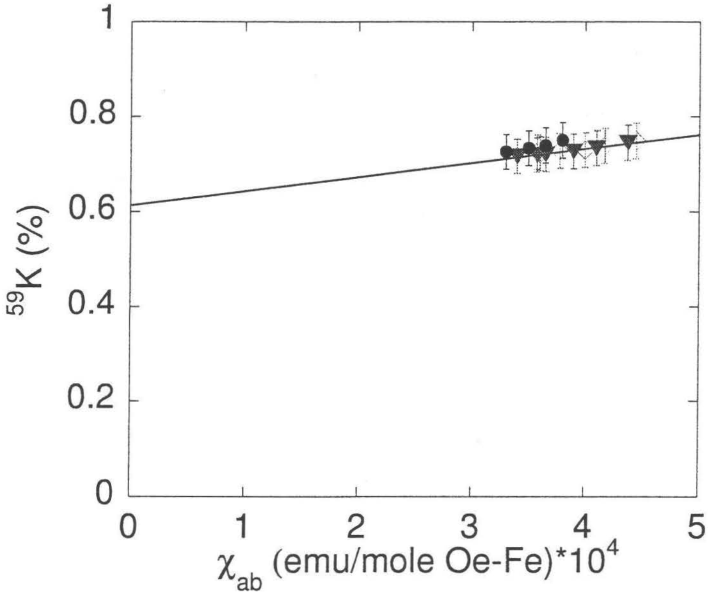

Figure 4.8 $^{59}K_c$ vs. χ plot for $x = 0.02$ (◇), 0.04 (▼), 0.082 (●), solid line is a linear fit to the data.

the nuclear spin and the electrons at the same ^{59}Co site; the other is the transferred hyperfine coupling $B_{transfer}$ arising from the interaction between the nuclear spin and the electrons at nearest neighbor Fe/Co sites via Fermi's contact interaction. We find from the linear fit in Fig. 4.8 that $A_{hf}(\mathbf{q} = 0) = A_{on-site} + 4B_{transfer} = 16 \pm 3$ kOe/μ_B is identical for $x = 0.02$, 0.04 and 0.082 from the ^{59}K vs. χ plot. It is difficult to separate $A_{on-site}$ and $B_{transfer}$ since we do not know the value of $A_{on-site}$. If we assume $A_{on-site}$ for Co ions are comparable to that of Fe^{2+} ions, which is ~ -139 kOe/μ_B (Freeman and Watson, 1965), we obtain $B_{transfer} = 40 \pm 2$ kOe/μ_B. These numbers will be used in the calculation of the hyperfine form factor $A(\mathbf{q})$ in the analysis of $1/T_1T$ in chapter 5.

4.6 Anisotropy of ^{75}K and ^{59}K of Ba(Fe$_{0.918}$Co$_{0.082}$)$_2$As$_2$

In this section, we will focus on the possible anisotropy of χ_s in the superconductor Ba(Fe$_{0.918}$Co$_{0.082}$)$_2$As$_2$ with the optimized $T_c = 22$ K in $B_{ext} = 0$. We plot $^{75}K_{ab}$ measured with $B_{ext} \parallel ab$ in Fig. 4.9, and compare the results with $^{75}K_c$. The magnitude of $^{75}K_{ab}$ is ~ 25 % larger than that of $^{75}K_c$. To compare the temperature

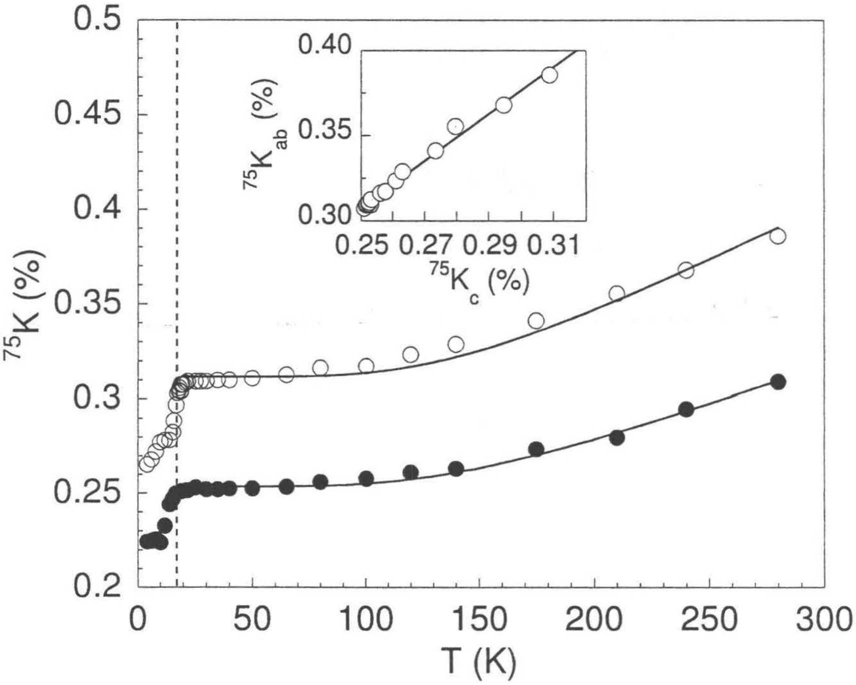

Figure 4.9 Temperature dependence of the ^{75}As NMR Knight shifts, $^{75}K_c$ (●), and $^{75}K_{ab}$ (■) in an external magnetic field $B_{ext} = 7.7$ Tesla applied along the c-axis or ab-plane. The black solid curves are the fit to an activation form above T_c, $^{75}K = A + B \times exp(-\Delta_{PG}/k_B T)$ with $A = 0.253\%$, $B = 0.415\%$, and the pseudo gap $\Delta_{PG}/k_B = 415 \pm 150$ K for $^{75}K_c$; and $A = 0.312\%$, $B = 0.581\%$, and the pseudo gap $\Delta_{PG}/k_B = 580 \pm 100$ K for $^{75}K_{ab}$. The dashed line marks T_c. The inset is the plot of $^{75}K_{ab}$ vs. $^{75}K_c$ above T_c; the solid line represents a linear fit.

dependence of ${}^{75}K_c$ and ${}^{75}K_{ab}$ above T_c, we plot ${}^{75}K_{ab}$ vs. ${}^{75}K_c$ in the inset of Fig. 4.9 by choosing temperature as the implicit parameter. The plot gives a straight line with a slope of 1.4. The linear relation indicates that ${}^{75}K_{ab}$ and ${}^{75}K_c$, hence χ_{ab} and χ_c at the ^{75}As site have an identical temperature dependence above T_c.

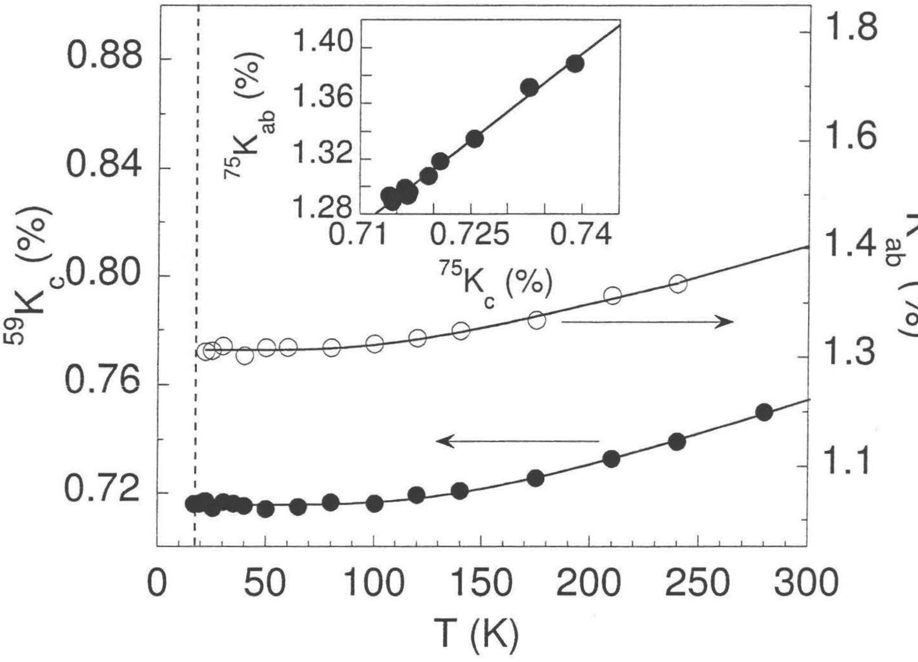

Figure 4.10 Temperature dependence of the ^{59}Co Knight shifts, ${}^{59}K_c$ (●), and ${}^{59}K_{ab}$ (■) in an external magnetic field $B = 7.7$ Tesla applied along the c-axis or ab-plane. The black solid curves are the fit to an activation form above T_c, ${}^{59}K = A + B \times exp(-\Delta_{PG}/k_B T)$ with $A = 0.715\%$, $B = 0.244\%$, and the pseudo gap $\Delta_{PG}/k_B = 560 \pm 150$ K for ${}^{59}K_c$; and $A = 1.290\%$, $B = 0.619\%$, and the pseudo gap $\Delta_{PG}/k_B = 440 \pm 150$ K for ${}^{59}K_{ab}$. The dashed line marks T_c. The inset is a plot of ${}^{59}K_{ab}$ vs. ${}^{59}K_c$ above T_c; the solid line represents a linear fit.

We also compare the temperature dependence of $^{59}K_{ab}$ and $^{59}K_c$ in Fig. 4.10. Similar to the case of ^{75}K, $^{59}K_c$ scales linearly with $^{59}K_{ab}$, as shown in the inset of Fig. 4.10. Therefore $^{59}K_c$ and $^{59}K_{ab}$ have an identical temperature dependence as well. We emphasize that both ^{75}K and ^{59}K represent the intrinsic temperature dependence of the magnetic susceptibility, and none of our results in Fig. 4.3 and Fig. 4.7 exhibit T-linear temperature dependence between T_c and ~ 300 K, in disagreement with the theoretical predictions (Zhang et al., 2009). Instead, both ^{75}K and ^{59}K level off below ~ 100 K. We also note that we find no hint of Curie behavior in ^{75}K and ^{59}K. This is in remarkable contrast with the case of high-T_c cuprates. When one substitutes Cu^{2+} ions with Li^+, Zn^{2+}, or Al^{3+} cations in CuO_2 planes of the high-T_c cuprates, the NMR Knight shifts observed at cation sites, as well as at nearby ^{17}O and ^{89}Y sites, exhibit a Curie behavior, $K \sim 1/T$ (Ishida et al., 1996, Bobroff et al., 1999). Such a Curie behavior arises because substituted ions induce localized magnetic moments at Cu sites in their vicinity because the CuO_2 planes are antiferromagnetic Mott insulators without doping. In contrast, our results imply that in $Ba(Fe_{1-x}Co_x)_2As_2$ compounds (i) Fe and Co sites carry comparable electron spin susceptibility (i.e. $\chi_{Co} \sim \chi_{Fe}$), (ii) Co substitution into Fe sites does not induce localized magnetic moments in the vicinity of Co sites, and hence (iii) the spatial variation of local spin susceptibility χ_s is relatively small. This inevitably leads us to suggest that the underlying physics of the iron-pnictide superconductors is quite different from that of antiferromagnetic Mott insulators which is generally believed to describe high-T_c cuprates.

4.6.1 ^{75}K below T_c

In this section, we discuss our preliminary measurements of superconducting properties below T_c. We plot $^{75}K_c$ and $^{75}K_{ab}$ below T_c in an expanded scale in Fig.

4.11. It is worth noting that Fig. 4.11 (Ning et al., 2008) was the first measurement of the temperature dependence of the spin susceptibility below T_c for both $\parallel c$ and $\parallel ab$ directions in any iron-based superconductors. Our results show, for the first time, that both $^{75}K_c$ and $^{75}K_{ab}$ decrease below T_c. This finding is consistent with a singlet pairing of the superconducting Cooper pairs, but is in conflict with the p-wave triplet superconductivity model. In the latter scenario, spin susceptibility should remain constant below T_c at least along one orientation, hence either $^{75}K_c$ or $^{75}K_{ab}$ should remain constant across T_c. In earlier reports for (La,Pr)FeAsO$_{1-\delta}$F$_\delta$ (Grafe et al., 2008, Matano et al., 2008), the authors erraneously claimed that they ruled out the spin triplet superconductivity scenario, but they showed only the decrease of $^{75}K_{ab}$ below T_c.

In principle, the temperature dependence of K_s below T_c can provide crucial information to differentiate the symmetry of the superconducting order parameter, such as s-wave and d-wave. To determine K_s accurately, we need to determine the magnetic field strength inside the sample precisely, because 1) the presence of the superconducting diamagnetic screening current changes the applied external magnetic field B_{ext} inside the sample; 2) the superconducting vortices induce a distribution of local magnetic field inside the sample. In the superconductor Ba(Fe$_{0.918}$Co$_{0.082}$)$_2$As$_2$, a possible way to determine the actual magnetic field seen by ^{75}As below T_c is to use ^{139}Ba NMR as an internal field marker, since $^{139}K_s$ at ^{139}Ba site is very small compared to that at the ^{75}As site. An analogous approach was successfully employed for the high T_c cuprate YBa$_2$Cu$_3$O$_7$, where ^{89}Y NMR was used as a field marker for ^{63}Cu NMR (Barrett et al., 1990). Unfortunately, we found that the ^{139}Ba NMR signal was very weak, and the ^{139}Ba lineshape is very broad because of the structural disorder caused by Co doping. Therefore the precise calibration of the magnetic field inside the sample below T_c has not been successful. In this sense, ^{75}K results in Fig.

4.11 should be considered somewhat preliminary.

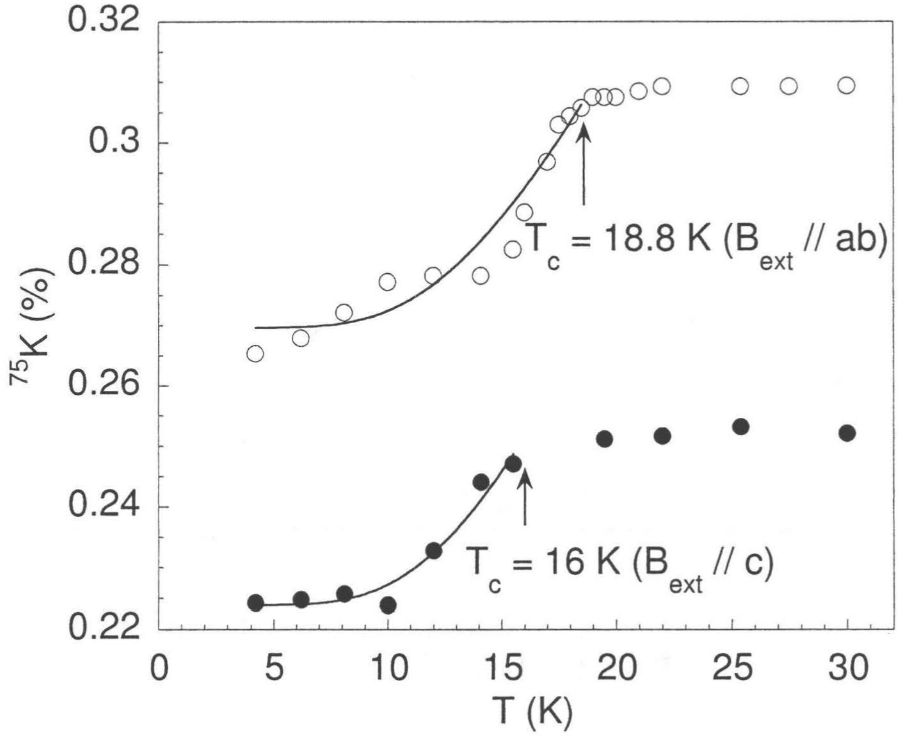

Figure 4.11 ^{75}K measured in $B_{ext} = 7.7$ Tesla below T_c in an expanded scale. Solid lines are fits of ^{75}K to $^{75}K = A + B \times exp(-\Delta/k_BT)$ with $A = 0.224\%$, $B = 0.930\%$, and the gap $\Delta/k_B = 56 \pm 10$ K for $^{75}K_c$; and $A = 0.270\%$, $B = 0.753\%$, and the gap $\Delta/k_B = 55 \pm 10$ K for $^{75}K_{ab}$. Arrows mark T_c at $B_{ext} = 7.7$ Tesla.

By fitting ^{75}K below T_c to $^{75}K = A + B \times exp(-\Delta/k_BT)$, as shown in Fig. 4.11, we can estimate the magnitude of the superconducting gap. The best fit yields the superconducting gap $\Delta/k_B = 56 \pm 10$ K for both $^{75}K_c$ and $^{75}K_{ab}$, respectively. Combined with T$_c$(7.7 Tesla) $\approx$ 17.5 K, we obtain $\Delta/k_BT_c = 3.2$. If we assume χ_s

diminishes to zero (Yosida, 1958) at the base temperature, $A = 0.224$ % is the chemical shift. This value of $^{75}K^{c}_{chem}$ is what we have been using in previous section.

4.7 Summary

In this chapter, we investigated the intrinsic static magnetic susceptibilities by measuring the Knight shift at the ^{75}As and ^{59}Co sites in Ba(Fe$_{1-x}$Co$_x$)$_2$As$_2$ compounds. We demonstrated that ^{75}K and ^{59}K exhibit qualitatively the same temperature dependence in the paramagnetic state for both $B_{ext} \parallel c$ and $B_{ext} \parallel ab$, i.e., K decreases continuously with temperature below 300 K down to ~100 K, but levels off below ~ 100 K. We showed that Ba(Fe$_{1-x}$Co$_x$)$_2$As$_2$ exhibits spin pseudo-gap behavior for a broad Co concentration range. We also established that Co doping does not induce localized magnetic moments. Through the measurement of Co concentration dependence, we also demonstrated that Co doping continuously suppresses ^{75}K. For the superconductor Ba(Fe$_{0.918}$Co$_{0.082}$)$_2$As$_2$ with optimized $T_c = 22$ K, we showed that the superconductivity arises from a novel electronic state with $\chi_s \sim$ constant and $\rho_{ab} \sim$ T after χ_s is suppressed, which is not consistent with canonical Fermi-liquid behavior, where $\rho \sim \mathrm{T}^2$. In chapter 5, we will also demonstrate that spin fluctuations are strongly enhanced near T_c. We also demonstrated that both $^{75}K_c$ and $^{75}K_{ab}$ decrease below T_c, and ruled out the p-wave superconductivity scenario.

Chapter 5

Dynamic Spin Susceptibility

In this chapter, we will discuss the dynamic spin susceptibility of $\mathrm{Ba(Fe_{1-x}Co_x)_2As_2}$ compounds deduced from the measurement of the nuclear spin-lattice relaxation rate ${}^{75,59}(1/T_1)$ at ^{75}As and ^{59}Co sites. As we have introduced in chapter 2, the temperature dependence of the nuclear spin-lattice relaxation rate divided by temperature, ${}^{75,59}(1/T_1T)$, can be expressed by Eq. 2.22,

$$ {}^{75,59}(\frac{1}{T_1T}) = \frac{\gamma_n^2 k_B}{2\mu_B^2} \sum_q |{}^{75,59}A(\mathbf{q})|^2 \frac{\chi\text{''}(\mathbf{q}, f)}{f}, \tag{5.1} $$

where $|{}^{75,59}A(\mathbf{q})|^2$ is the wave-vector $\mathbf{q}$-dependent hyperfine form factor, and $\chi\text{''}(\mathbf{q}, f)$ is the imaginary part of the dynamical electron spin susceptibility. f is the NMR frequency used for $1/T_1$ measurements, and in general, $f \lesssim 10^2$ MHz. $\chi\text{''}(\mathbf{q}, f)$ represents the strength of spin fluctuations for the Fourier component of $\mathbf{q}$ and f. One can, in principle, measure the $\mathbf{q}$ and f dependence of $\chi\text{''}(\mathbf{q}, f)$ by an inelastic neutron scattering measurement. Since $hf \sim 0.4$ μeV for $f = 100$ MHz, $1/T_1T$ corresponds to the slope at the low energy limit, $\frac{\chi\text{''}(\mathbf{q},f)}{f}$. While $1/T_1T$ data lack the information on $\mathbf{q}$ and f dependences, our major advantage is that $1/T_1T$ can probe spin excitations even if the $\mathbf{q}$ dependence of $\chi"(\mathbf{q}, f)$ is very weak in, e.g., weakly correlated metals, and hence neutron scattering cannot even detect spin excitations at low energies. This was indeed the case in $YBa_2Cu_3O_7$, and it also turns out that is the case for the overdoped non-superconducting $Ba(Fe_{1-x}Co_x)_2As_2$ with $x \sim 0.26$ (Ning et al., 2009d).

5.1 Hyperfine Form Factor $|^{75}A(\mathbf{q})|^2$ at ^{75}As sites

Assuming that the spin density resides primarily in the $3d$ orbitals at Fe and Co sites, we may represent the hyperfine form factor at ^{75}As sites as,

$$|^{75}A(\mathbf{q})|^2 = |4C_{transfer}cos(q_x a^*/2)cos(q_y a^*/2)|^2, \tag{5.2}$$

where a^* is the distance between Fe sites (the Fe-Fe bond length). a^* is $\sim \frac{1}{\sqrt{2}}$ of the a-axis lattice constant. $C_{transfer}$ is the transferred hyperfine coupling between the ^{75}As nuclear spin and $3d$ electrons at four nearest neighbor Fe or Co sites. For simplicity, we ignore the small anisotropy of $C_{transfer}$, and use the unfolded Brillouin Zone with only one As site in each unit cell. In chapter 4, we obtained $A_{hf} = 4C_{transfer} \sim 20 \pm 4$ kOe/μ_B from the ^{75}K vs. χ plot. Therefore we use $C_{transfer} = 5 \pm 1$ kOe/μ_B to calculate $|^{75}A(\mathbf{q})|^2$. We plot $|^{75}A(\mathbf{q})|^2$ in the unfolded first Brillouin Zone (B. Z.) in Fig. 5.1. We can see from the figure that $|^{75}A(\mathbf{q})|^2$ peaks at the zone center $\mathbf{q} = (0, 0)$, and continuously decreases to zero toward the zone boundary, i.e. $\mathbf{q} = (\pi/a, 0)$ or $\mathbf{q} = (\pi/a, \pi/a)$. The $\mathbf{q}$ dependent $|^{75}A(\mathbf{q})|^2$ has important implications in the analysis of $^{75}(1/T_1T)$ in the next section.

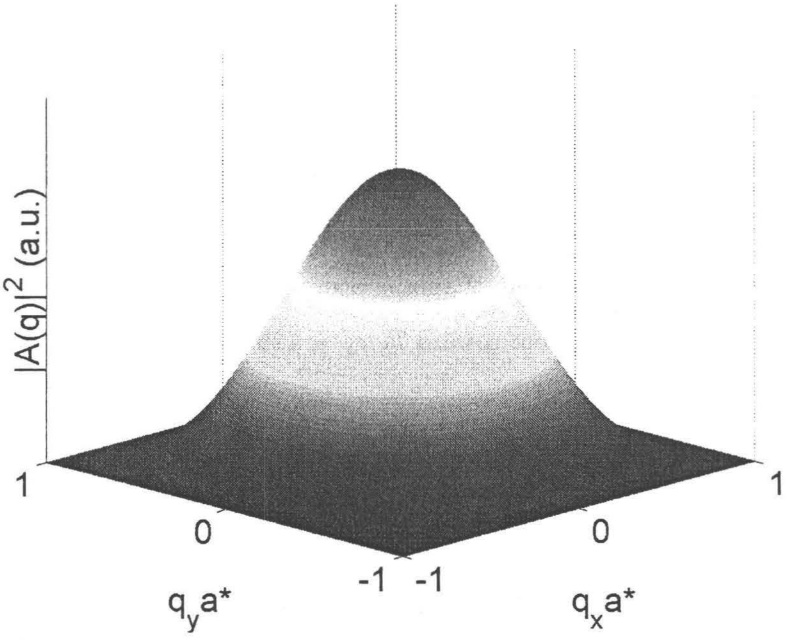

Figure 5.1 Hyperfine form factor $|^{75}A(\mathbf{q})|^2$ at ^{75}As sites in the FeAs layer plotted in the unfolded first Brillouin Zone.

5.2 $^{75}(1/T_1T)$ for $x = 0, 0.02, 0.04, 0.082, 0.099$

We presented the ^{75}As lineshapes of $Ba(Fe_{1-x}Co_x)_2As_2$ for various concentration x with $B_{ext} \parallel c$ in Fig. 3.1. Utilizing the technique introduced in chapter 2, we measure $^{75}(1/T_1)$ at the frequency of the central transition (m = 0) of the As(0) site. We fit the recovery curve of the ^{75}As nuclear magnetization to a theoretical function for the central transition of the nuclear spin $I = 3/2$,

$$\frac{M_0 - M(t)}{M_0} = 0.1exp(-\frac{t}{T_1}) + 0.9exp(-\frac{6t}{T_1}). \tag{5.3}$$

where t is the delay time. In Fig. 5.2, we show the representative fits for the As(0) site of the $x = 0.082$ superconducting sample at different temperatures. The fits of $^{75}(1/T_1)$ are reasonable for all concentrations at the temperature range presented in this thesis. Data points at 12 K are somewhat scattered because the signal to noise ratio below T_c is limited by the shorter RF penetration depth and longer T_1.

We measured $^{75}(1/T_1)$ as a function of temperature for each concentration, and summarize the results of $^{75}(1/T_1T)$ in Fig. 5.3. $^{75}(1/T_1T)$ of the undoped $x = 0$ sample is almost independent of temperature below 300 K down to $\sim$ 200 K, then exhibits a small enhancement toward $T_{SDW} = 135$ K. The enhancement toward T_{SDW} is consistent with a critical slowing down of spin fluctuations toward $T_{SDW} = 135$ K due to the antiferromagnetic phase transition. However, the enhancement is small in the present case, and we do not observe a divergence of $^{75}(1/T_1T)$ at 135 K. We note that $1/T_1T$ would diverge at a typical second order phase transition into a magnetically ordered state. Two factors may contribute to the absence of divergence

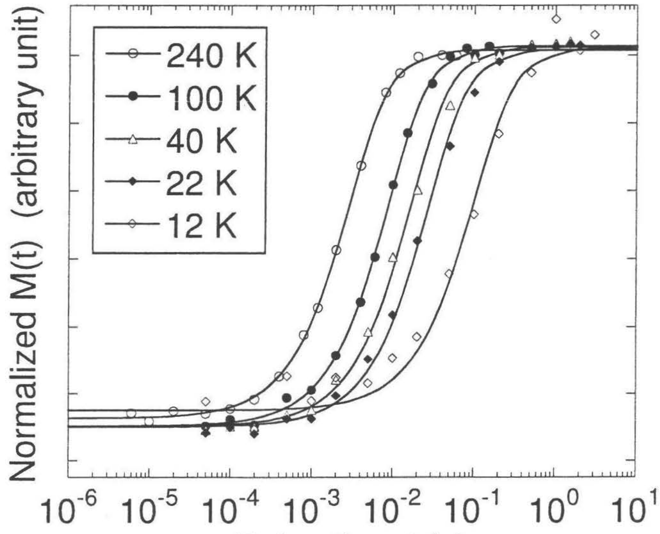

Figure 5.2 Typical nuclear spin recovery curves $M(t)$ after an inversion pulse for ^{75}As of $x = 0.082$ sample. Solid curves are appropriate fits to determine T_1 with the solution of master equation (Eq. 5.3) for $I = 3/2$.

at T_{SDW}: First, the antiferromagnetic long range order (AFLRO) is accompanied by a tetragonal to orthorhombic structural phase transition (Huang et al., 2008), and the simultaneous magnetic and structural phase transitions are weakly first order (Kitagawa et al., 2008). Second, we note that $^{75}(1/T_1T)$ at ^{75}As sites were measured with $B_{ext} \parallel c$-axis. In this geometry, $^{75}(1/T_1T)$ probes spin fluctuations within the *ab*-plane. We have shown in Fig. 5.1 that the ^{75}As hyperfine form factor satisfies $|^{75}A(\mathbf{q})|^2 = 0$ at the edge of the unfolded Brillouin Zone in this geometry. Since the spin correlations are commensurate with the lattice for $x = 0$ (Huang et al., 2008), $\chi"(\mathbf{q}, f)$ would be enhanced at $\mathbf{q} = (\pi/a,\ 0)$. Consequently, $^{75}(1/T_1T)$ would not diverge at T_{SDW} even if $\chi"(\mathbf{q}, f)$ diverges at T_{SDW}. Analogous absence of divergence of $1/T_1$ was previously seen in ^{17}O NMR measurements of the S = 1/2 2D-square-lattice $Sr_2CuO_2Cl_2$ (Thurber et al., 1997).

In contrast with $x = 0$, $1/T_1T$ of the underdoped $x = 0.02$ and 0.04 samples displays a strong divergent behavior toward $T_{SDW} = 100$ K and 66 K after an initial decrease below 300 K down to ~200 K. We confirmed that the paramagnetic NMR signals completely disappear below T_{SDW}, as shown in Fig. 3.4, hence all ^{75}As nuclear spins are under the influence of the magnetic phase transition at T_{SDW}. In view of the absence of divergence for the $x = 0$ sample, the divergence observed for $x = 0.02$ and 0.04 samples hints at two possible changes in the electronic properties caused by Co doping. First, the magnetic phase transition at T_{SDW} is no longer first order, because Co doping separates the magnetic phase transition from the first order structural phase transition. The separation of T_S and T_{SDW} with Co doping in $Ba(Fe_{1-x}Co_x)_2As_2$ compounds was initially reported by Fisher's group (Chu et al., 2009), and is shown in the phase diagram in Fig. 1.8. Second, the magnetically ordered moments may not be commensurate with the lattice any more. We recall that the commensurate spin fluctuations at $\mathbf{q} = (\pi/a,\ 0)$ would result in the cancelation of hyperfine fields at ^{75}As site for $x = 0.02$ and 0.04 samples, and the divergence of $\chi"(\mathbf{q}, f)$ at $\mathbf{q} = (\pi/a, 0)$ would be filtered out at ^{75}As sites. Therefore our observation of divergence of $1/T_1T$ toward T_{SDW} for $x = 0.02$ and 0.04 samples is consistent with the critical slowing down of incommensurate spin fluctuations toward a second order phase transition at T_{SDW}. Alternatively, if the spin structure remains commensurate, the q-width of $\chi"(\mathbf{q}, f)$ must remain broad at T_{SDW} (or, equivalently, the spin-spin correlation length ξ remains finite).

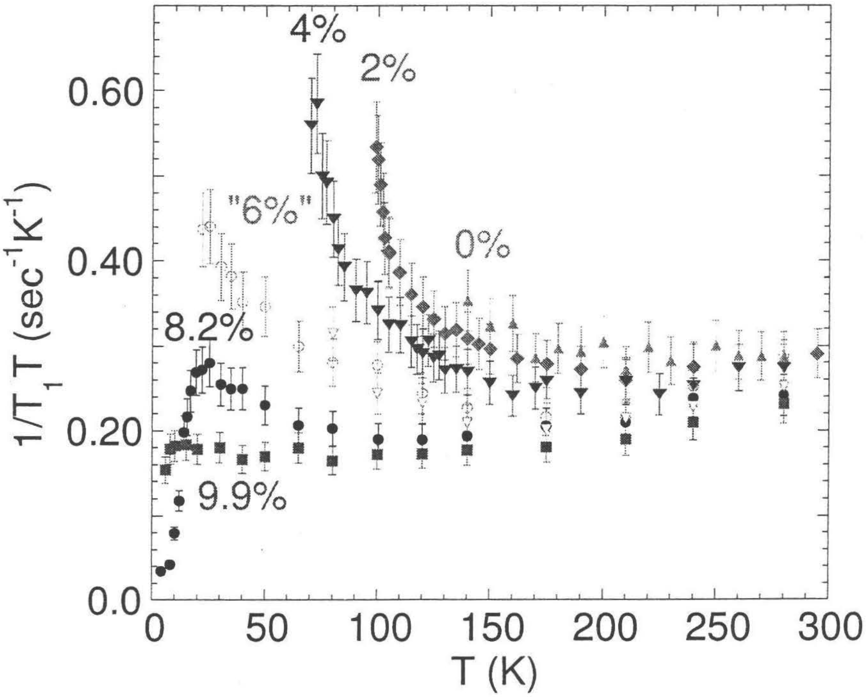

Figure 5.3 Filled symbols show $1/T_1T$ measured at the peak of the ^{75}As NMR lineshapes for $x = 0$, 0.02, 0.04, 0.082, and 0.099. Open circles (triangles) labeled as "6%" were deduced from the half intensity position of the FFT lineshape of the 8.2 % (4 %) doped sample on the higher (lower) frequency side. See the main text for details.

We have not conducted NMR measurements on the concentration $x = 0.06$ because the sample is not available. However, the NMR lineshapes of the $x = 0.04$ and 0.082 samples are significantly overlapped, which suggests that local electronic properties vary position by position in the Co-doped FeAs layers due to "patchy inhomogeneity" (Yin et al., 2009), as shown in Fig. 4.1. In fact, we found that $1/T_1T$ measured at the half-intensity position on the lower K side of the lineshape of the $x = 0.04$ is nearly the same as $1/T_1T$ measured at the half intensity position on the higher K side of the lineshape of the $x = 0.082$ crystal. We show examples of $1/T_1T$ measured at the off-peak positions in Fig. 4.1. The $1/T_1T$ measured in the off-peak position between the peaks of $x = 0.04$ and 0.082 is plotted in Fig. 5.3, labeled as the results for the effective concentration of "6%". $1/T_1T$ of "6%" initially decreases below 300 K, and then increases toward T_{SDW}.

Very recently, the gap of NMR data between $x = 0.04$ and 0.082 samples has been filled by two other research groups. Julien et al. reported $1/T_1T$ of a $x = 0.05$ sample with $T_{SDW} = 56$ K (Julien et al., 2009), and Laplace et al. reported $1/T_1T$ with $B_{ext} \parallel ab$-plane of $x = 0.06$ sample with $T_{SDW} = 31$ K (Laplace et al., 2009). Their results indicate that the divergent behavior of $1/T_1T$ toward T_{SDW} becomes less pronounced for $x = 0.05$ and 0.06, but the enhancement is still fairly strong. The temperature dependence of their $1/T_1T$ results quantitatively agree with what we estimated for the effective concentration of "6%", and thus support our estimation, and the physical picture of "patchy inhomogeneity".

When Co concentration reaches $x = 0.082$, the SDW order is completely suppressed, and the sample becomes superconducting below $T_c = 22$ K. $1/T_1T$ initially decreases with T below 300 K, but exhibits fairly large enhancement below ~100 K toward the superconducting transition temperature T_c. For the slightly overdoped $x = 0.099$ sample, the enhancement toward $T_c = 15$ K is weak but still exists, as shown in Fig. 5.3. In fact, our latest work on the overdoped region (Ning et al., 2009d) shows that the enhancement of $1/T_1T$ at low temperatures does not diminish until the superconducting transition is completely suppressed above $x = 0.12$. On the other hand, ARPES measurements in the $\mathrm{Ba(Fe_{1-x}Co_x)_2As_2}$ compounds showed that the hole Fermi surfaces around the Γ point (see Fig. 1.4) almost disappear when the doping level reaches $x = 0.15$ (Sekiba et al., 2009).

What is the implication of these experimental results on the evolution from the SDW to the superconducting state with the doping level x? In the undoped parent compound, the nesting of the Fermi surfaces between the hole and electron pockets is separated by a nesting wave vector $\vec{Q}_{AF} \cong (\pi/\mathrm{a},\ 0)$ or $(0,\ \pi/\mathrm{a})$, which leads to the commensurate spin density wave (C-SDW). When we dope Co into FeAs layers, doped electrons begin to fill the hole Fermi surfaces, and the hole pockets shrink. At the same time, doped electrons enlarge the electron Fermi surfaces near the X point. Consequently, the nesting deteriorates, and both the ordering temperature T_{SDW} and the magnitude of the ordered moments are suppressed. Either an incommensurate SDW or a commensurate but highly disordered C-SDW ground state appears at the light doping level $x \sim 0.02$, and the signature of superconductivity emerges at $x > 0.02$ in ρ_{ab}. When x increases up to ~ 0.08, the SDW is completely suppressed, but the enhancement of antiferromagnetic spin fluctuations toward T_c persists, and the superconducting transition temperature T_c is maximized at 22 K. When x increases to the overdoped region $x = 0.099$, the spin fluctuation is further suppressed and T_c starts to decrease. At the doping level of $x \geq 0.14$, the hole Fermi surface is completely filled with electrons, and the spin fluctuations is dramatically suppressed (Ning et al., 2009c). Consequently, the superconductivity disappears.

Combining all pieces together, we conclude that the inter-band spin excitations with $\vec{Q}_{AF} \sim (\pi/\mathrm{a},\ 0)$ or $(0,\ \pi/\mathrm{a})$ between the hole and electron Fermi surfaces play a crucial role in the superconducting mechanism of $Ba(Fe_{1-x}Co_x)_2As_2$ compounds. In fact, we recently found that $^{75}(1/T_1T)$ at 25 K, the strength of the antiferromagnetic spin fluctuations associated with the inter-band spin excitations, is closely correlated with the superconductivity (Ning et al., 2009d). To achieve the maximum T_c, the strength of the spin fluctuations have to be just right, neither too strong nor too weak.

Now let us reexamine another important aspect of Fig. 5.3. Notice that $1/T_1T$ initially *decreases* with T below 300 K before $1/T_1T$ begins to increase below ~ 100 K even in the underdoped $x = 0.02$ and 0.04 samples. In other words, before critical slowing down sets in toward T_{SDW}, the $\mathbf{q}$-integral of the low frequency spin fluctuations becomes smaller below 300 K. In the next section, we will show that $1/T_1T$ at the Co sites in $x = 0.02$, 0.04 and 0.082 shows qualitatively the same behavior below 300 K as at the ^{75}As sites, hence the present results are not the consequence of accidental cancelation of the hyperfine fields at the ^{75}As sites. We also recall that in chapter 4, the uniform (i.e. $\mathbf{q} = \mathbf{0}$) spin susceptibility χ_s measured as the Knight shift at both ^{75}As and ^{59}Co also decreases below 300 K for all concentrations. Therefore we conclude that low energy spin excitations for a broad range of wave vector $\mathbf{q}$ modes are suppressed below 300 K with decreasing T. We note that analogous suppression of spin excitations in iron-pnictides superconductors was first observed by our group in $LaFeAsO_{0.89}F_{0.11}$ ($T_c = 28$ K) using ^{19}F NMR (Ahilan et al., 2008b). The simultaneous suppression of χ_s and $1/T_1T$ was previously observed for underdoped high T_c cuprates (Takigawa et al., 1991), and is known as (spin) "pseudo gap". Although the mechanism behind the (spin) pseudo-gap behavior is unclear at this time, it is interesting to realize that the $J_1 - J_2$ Heisenberg model, which is considered a viable starting point for the theoretical description of iron-pnictides (Si and Abrahams, 2008), is indeed expected to exhibit a gapped behavior in NMR properties (Mila et al., 1991). On the other hand, if we consider Fe spins as localized moments described by the $J_1 - J_2$ Heisenberg model, we expect that the exchange narrowing effects lead to $1/T_1 \sim constant$ (Imai et al., 1993), hence $1/T_1T \sim 1/T$, in the intermediate temperature range $T \sim J_{1,2}/2$ or higher. We do not observe such localized moment behavior in Fig. 5.3 at least up to 300 K. Therefore, such a local moment description of $Ba(Fe_{1-x}Co_x)_2As_2$ may not be valid. Another interesting point to note is that the pseudo-gap like behavior persists up to the non-superconducting metallic phase with $x = 0.26$ (Ning et al., 2009d). Since only electron Fermi surfaces exist in $x = 0.26$, the pseudo-gap like behavior may be caused primarily by intra-band spin excitations for electron Fermi surfaces.

5.3 Hyperfine Form Factor $|^{59}A(\mathbf{q})|^2$ at ^{59}Co sites

We now turn our attention to $1/T_1$ at the ^{59}Co sites. Considering only the nearest neighbor Fe/Co sites, the hyperfine form factor $|^{59}A(\mathbf{q})|^2$ at the ^{59}Co sites can be expressed as,

$$|^{59}A(\mathbf{q})|^2 = |A_{on-site} + 2B_{transfer}(cos(q_x a^*) + cos(q_y a^*))|^2, \tag{5.4}$$

where a^* is the distance between Fe sites (Fe-Fe bond length), as defined in section 5.1. As introduced in chapter 2, $A_{on-site}$ represents the hyperfine coupling between the ^{59}Co nuclear spin and the Co electron spin at the same site, and $B_{transfer}$ is the transferred hyperfine interaction between the ^{59}Co nuclear spin and the electrons at the four nearest neighbor Fe or Co sites. $A_{on-site}$ for Co^{2+} ions is not known, and we substitute $A_{on-site}$ = -139 kOe/μ_B of Fe^{2+} ions (Freeman and Watson, 1965) for Co^{2+}. Using $A_{on-site} + 4B_{tranfer} = 16$ kOe/μ_B from the ^{59}K vs. χ analysis in chapter 4, we obtain $B_{tranfer}$ = 40 kOe/μ_B. We calculated the **q**-dependent $|^{59}A(\mathbf{q})|^2$ using $A_{on-site}$ = -139 kOe/μ_B and $B_{tranfer}$ = 40 kOe/μ_B, and present the result in the unfolded first Brillouin Zone in Fig. 5.4. In contrast with the case of $|^{75}A(\mathbf{q})|^2$ at the ^{75}As site in Fig. 5.1, the hyperfine form factor $|^{59}A(\mathbf{q})|^2$ at ^{59}Co site is very small around the zone center, i.e. near $\mathbf{q}$ = (0,0) and the surrounding region (0 < q $\ll \pi/a$). $|^{59}A(\mathbf{q})|^2$ is finite at $\mathbf{q} = (\pi/a, 0)$ and peaked at the zone corner $\mathbf{q} = (\pi/a, \pi/a)$. We also confirmed that $|^{59}A(\mathbf{q})|^2$ hardly changes even if we take into account the transferred hyperfine interaction from the second N.N. Fe/Co sites.

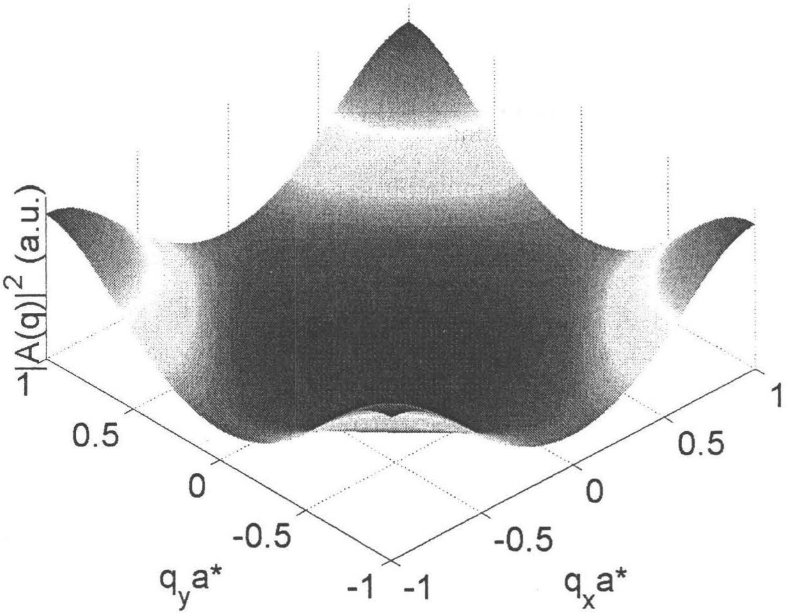

Figure 5.4 Hyperfine form factor $|^{59}A(\mathbf{q})|^2$ at ^{59}Fe sites in the FeAs layer plotted in the unfolded first Brillouin Zone.

5.4 $^{59}(1/T_1T)$ for $x = 0.02$, 0.04

We presented the ^{59}Co lineshapes of $Ba(Fe_{1-x}Co_x)_2As_2$ of $x = 0.02$, 0.04 and 0.082 in Fig. 3.5, Fig. 3.6 and Fig. 3.11, respectively. We measured $^{59}(1/T_1)$ of the ^{59}Co sites in the paramagnetic state at the frequency of the central transition ($m = 0$). The recovery curve of the ^{59}Co nuclear magnetization can be fit to the theoretical function for the central transition of nuclear spin $I = 7/2$,

$$\frac{M_0 - M(t)}{M_0} = \frac{1225}{1716} exp(-28\frac{t}{T_1}) + \frac{75}{364} exp(-15\frac{t}{T_1}) + \frac{3}{44} exp(-6\frac{t}{T_1}) + \frac{1}{84} exp(-\frac{t}{T_1}). \tag{5.5}$$

where t is the delay time. We show the representative nuclear spin recovery curves M(t) after an inversion pulse observed for $x = 0.082$ in Fig. 5.5. For the ordered state below T_{SDW} in $x = 0.02$ and 0.04 samples, we measure $^{59}(1/T_1)$ at the peak position of the broad hump, as marked by the arrows in Fig. 3.5 and 3.6. We show the appropriate fits at different temperatures for the $x = 0.04$ sample in Fig. 5.6. The fits are good even below T_{SDW}.

We summarize the temperature dependence of $^{59}(1/T_1T)$ for $x = 0.02$, 0.04 and 0.082 in Fig. 5.7. $^{59}(1/T_1T)$ decreases roughly linearly with temperature from 290 K down to $\sim$ 150 K for both $x = 0.02$ and 0.04, and shows qualitatively the same behavior as that of the superconducting $x = 0.082$ sample except near T_{SDW}. The continuous suppression of $^{59}(1/T_1T)$ with temperature is consistent with that observed for $^{75}(1/T_1T)$ at the ^{75}As site, i.e. pseudo-gap like behavior. On the other hand, $1/T_1T$ shows a divergent behavior at $T_{SDW} = 100$ K for $x = 0.02$, and 66 K for $x = 0.04$. As explained in Fig. 3.10, these temperatures agree well with the maximum negative slope observed for in-plane resistivity (Ning et al., 2009a), by which we defined the temperature of T_{SDW}. In the previous section, we already discussed the

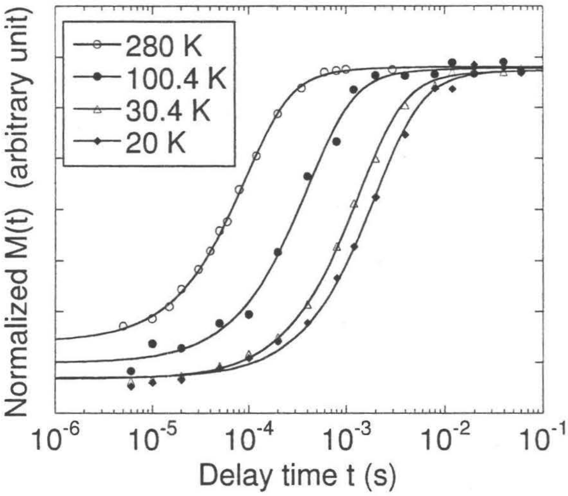

Figure 5.5 Typical ^{59}Co nuclear spin recovery curves $M(t)$ after an inversion pulse for the $x = 0.082$ sample. Solid curves are appropriate fits to determine T_1 with the solution of master equation, Eq. 5.5 for $I = 7/2$.

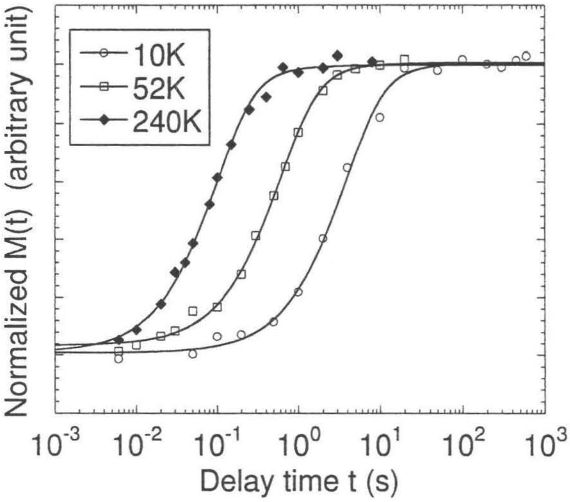

Figure 5.6 Typical ^{59}Co nuclear spin recovery curves $M(t)$ after an inversion pulse for the $x = 0.04$ sample. Solid curves are the best fits to determine T_1 with the solution of master equation, Eq. 5.5 for $I = 7/2$.

divergent behavior of ${}^{75}(1/T_1T)$ at ^{75}As sites with $B_{ext} \parallel c$-axis. Therefore, these $1/T_1T$ data at ^{59}Co and ^{75}As provides strong evidence for the critical slowing down of spin fluctuations toward a second order SDW transition at T_{SDW}.

Unlike the case of the ^{75}As site, the reliable measurement of ${}^{59}(1/T_1T)$ below T_{SDW} in lightly Co doped samples was feasible, thanks to the relatively narrow lineshape when we apply $B_{ext} \parallel c$. Therefore we can investigate the spin fluctuations below T_{SDW} for $x = 0.02$ and 0.04 through the measurement of ${}^{59}(1/T_1T)$. The results

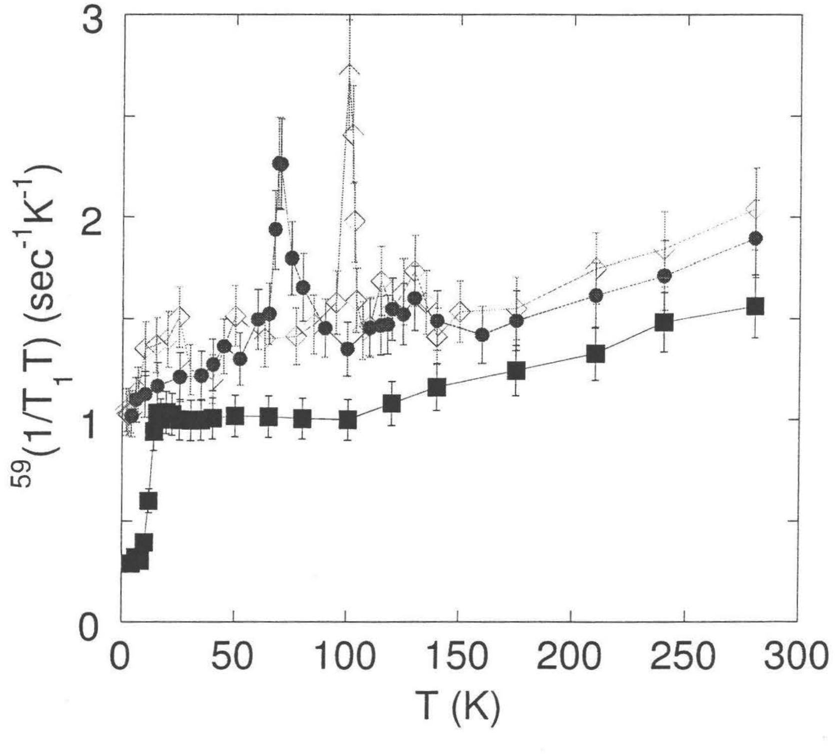

Figure 5.7 ${}^{59}(1/T_1T)_c$ at ^{59}Co sites for $x = 0.02$ (◇), 0.04 (●) and 0.082 (■). We measured T_1 at the central transition, as marked by the open arrows in Fig. 3.5 and Fig. 3.6.

below T_{SDW} in Fig 5.7 show that $^{59}(1/T_1T)$ is roughly temperature independent below ~ 50 K, and remains large. This is in remarkable contrast with the case of undoped parent compounds; We recall that $1/T_1T$ at ^{139}La sites in undoped LaFeAsO (Nakai et al., 2008) and ^{75}As sites in undoped $BaFe_2As_2$ (Kitagawa et al., 2008, Shirage et al., 2008) is suppressed below T_{SDW} by an order of magnitude or more. The fairly large values of $^{59}(1/T_1T)$ below T_{SDW} suggest that spin fluctuations remain strong even at the base temperature in the present case. This may be an indication that Fe *3d* spins in some *3d* orbitals remain paramagnetic below T_{SDW} as suggested by Singh et al (Singh, 2008, Sefat et al., 2008b) based on Fermiology. For example, some *3d* electrons belonging to electron (hole) Fermi surfaces may remain paramagnetic below T_{SDW}. Alternatively, if Co ions suppress the SDW order only in their vicinity, the large $^{59}(1/T_1T)$ below T_{SDW} may reflect the existence of paramagnetic Fe spins nearby. However, this scenario seems somewhat unlikely, because we would observe a large distribution of $^{59}(1/T_1)$ below T_{SDW}. As shown in Fig. 5.6, the fit is good even below T_{SDW} and there is no evidence for a large distribution of $^{59}(1/T_1)$. In passing, it is worth noting that the large in-plane resistivity below T_{SDW} in the Co-doped samples (Ahilan et al., 2008a, Ning et al., 2009a) is probably related to these strong spin fluctuations.

We also emphasize that we find no signature of additional spin freezing at low temperatures in either $1/T_1T$ or ΔB^c_{hf} below T_{SDW}. In the case of lightly doped $La_{2-x}Sr_xCuO_2$ with $x = 0.016$ (Chou et al., 1993, Cho et al., 1992), $1/T_1T$ at ^{139}La sites shows additional diverging behavior at a spin freezing temperature, $T_{sf} \sim 16$ K, much below $T_N \sim 120$ K, and the static hyperfine field B_{hf} shows additional enhancement below T_{sf} because the ordered moments grow. The spin freezing temperature T_{sf} turned out to be related to glassy freezing of spin and charge stripes. Our present observation is markedly different from the case of the lightly doped cuprates; we found no hint of analogous freezing of stripes.

5.5 $^{75}(1/T_1T)$ and $^{59}(1/T_1T)$ of $x = 0.082$

5.5.1 T-dependence of $1/T_1T$

We now focus our special attention on the dynamic spin susceptibility of the superconducting sample $x = 0.082$ with the optimized $T_c = 22$ K. We show the temperature dependence of the ^{59}Co and ^{75}As nuclear spin-lattice relaxation rate divided by T, $^{59}(1/T_1T)$ and $^{75}(1/T_1T)$ measured with $B_{ext} \parallel c$ for the $x = 0.082$ sample in Fig. 5.8, and $^{59}(1/T_1)$ and $^{75}(1/T_1)$ in Fig. 5.9. $^{75,59}(1/T_1T)$ continuously decreases from 300 K down to ~ 100 K, which is nearly identical to that of $^{75,59}K$ shown in chapter 4 as already discussed in section 5.4. The decrease of $^{59,75}(1/T_1T)$ and $^{59,75}K$ below 300 K signals the suppression of the low energy spin excitations with decreasing temperature, i.e. pseudo-gap behavior. We fit the temperature dependence of $^{59}(1/T_1T)$ with an activation type function, as shown in Fig. 5.8. The best fit yields the same magnitude of a gap $\Delta_{PG}/k_B = 560 \pm 150$ K as that of $^{59}K_c$ ($\Delta_{PG}/k_B = 560 \pm 150$ K).

A closer look at Fig. 5.8 reveals that $^{75}(1/T_1T)$ displays enhancement with decreasing temperature toward T_c, but $^{59}(1/T_1T)$ becomes constant below 100 K down to T_c. The different behavior between $^{75}(1/T_1)$ and $^{59}(1/T_1)$ just above T_c can be seen more clearly in Fig. 5.9, where $^{59}(1/T_1)$ scales with T, but $^{75}(1/T_1)$ does not. The origin of the enhancement toward T_c of $^{75}(1/T_1T)$ has been discussed in the previous section, and it is the residual antiferromagnetic spin fluctuations from the spin excitations between the hole and electron Fermi surfaces with momentum transfers, $\vec{Q} \sim (\pi/a,0)$. However, $^{59}(1/T_1T)$ at the ^{59}Co site is obviously insensitive to this residual antiferromagnetic spin fluctuations. There are several possibilities why ^{59}Co and ^{75}As show different behaviors.

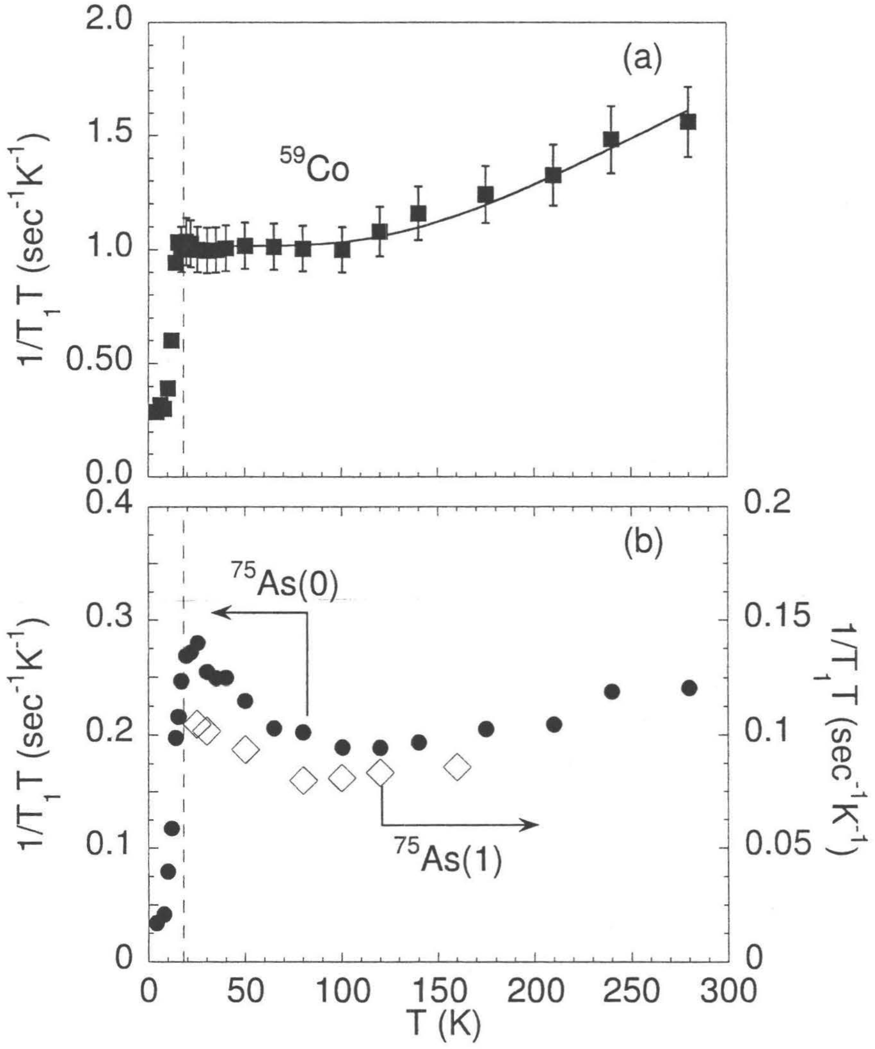

Figure 5.8 (a) $^{59}(1/T_1T)$ (■) measured with $B_{ext} \parallel c$. The dashed curve is a fit to an activation form, $^{59}(1/T_1T) = A + B \times exp(-\Delta_{PG}/k_BT)$ with $A = 1.0$ sec^{-1}K^{-1}, $B = 4.3$ sec^{-1}K^{-1}, and the magnitude of pseudo-gap $\Delta_{PG}/k_B = 560$ K. (b) Left axis: $^{75}(1/T_1T)$ of ^{75}As(0) site (•); Right axis: $^{75}(1/T_1T)$ of ^{75}As(1) site (◇). Notice that the temperature dependence of $^{75}(1/T_1T)$ are same for both As(0) and As(1) sites.

First, as we showed in Fig. 5.4, $|^{59}A(\mathbf{q})|^2$ is very small in the vicinity of $\mathbf{q} =$ (0,0) ($|\mathbf{q}| \ll \pi/a$). If spin fluctuations grow for these small wave vector modes toward T_c, $^{59}(1/T_1T)$ would be insensitive to their growth but $^{75}(1/T_1T)$ would grow toward T_c since $|^{75}A(\mathbf{q})|^2$ is relatively large for $|\mathbf{q}| \ll \pi/a$. However, we can safely rule out such a possibility of ferromagnetic enhancement, because both ^{75}K and ^{59}K are temperature independent below 100 K toward T_c. In other words, the difference in the $\mathbf{q}$-dependent hyperfine form factor $|^{59}A(\mathbf{q})|^2$ is highly unlikely to account for the distinctive T-

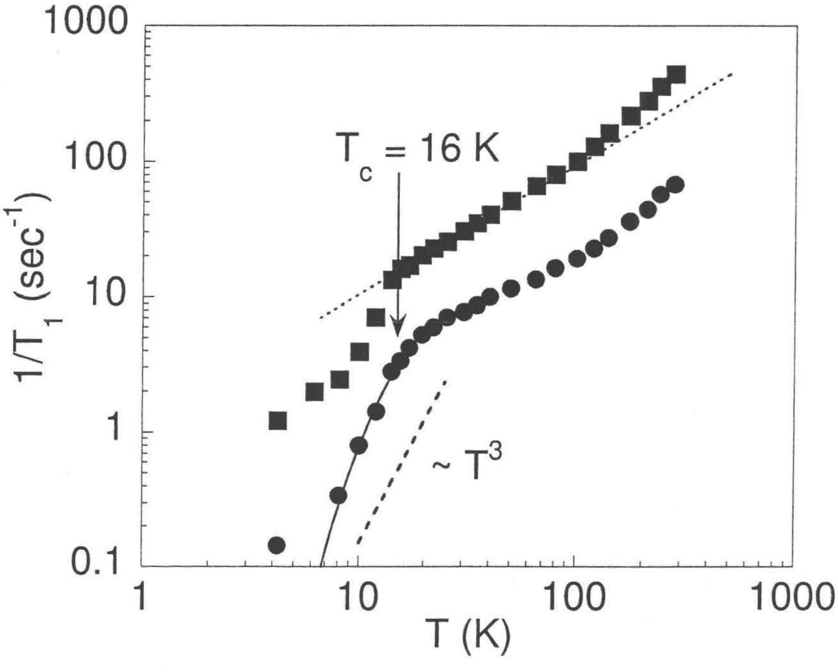

Figure 5.9 The temperature dependence of the ^{59}Co and ^{75}As nuclear spin lattice relaxation rate $^{59}(1/T_1)$(■) and $^{75}(1/T_1)$(•) measured with $B_{ext} \parallel c$. The dotted line represents a T-linear behavior of $^{59}(1/T_1)$. The solid line is a fit of $^{75}(1/T_1)$ to $exp(-\Delta/k_BT)$ with $\Delta/k_B = 42$ K. The arrow marks T_c = 16 K in $B_{ext} = 7.7$ Tesla.

dependence of $^{59}(1/T_1T)$ and $^{75}(1/T_1T)$ below 100 K. The second scenario is that Co doping suppresses the growth of antiferromagnetic spin fluctuations locally. However, this scenario also seems unlikely. In this scenario, $^{75}(1/T_1T)$ of As sites at N.N. site of Co atoms would be suppressed as well but we found that $^{75}(1/T_1T)$ of As(1) site displays identical enhancement toward T_c as that of As(0) site, as shown in Fig. 5.8. Third, we showed in Fig. 1.4 that hole Fermi surfaces are mainly contributed by electrons in d_{XZ} and d_{YZ} orbitals. We note that d_{XZ}/d_{YZ} orbitals may have zero contributions to the transferred hyperfine coupling, $B_{transfer}$, because d_{XZ}/d_{YZ} are orthogonal to 4s orbitals of Co. If antiferromagnetic spin fluctuations with $\vec{Q} \sim (\pi/a,0)$ rely on the excitations between the hole and electron Fermi surfaces, d_{XZ}/d_{YZ} like segments of the hole Fermi surfaces to the d_{XZ}/d_{YZ} like segments of the electron Fermi surfaces, they may not have a significant contribution to $^{59}(1/T_1T)$ toward T_c.

5.5.2 $1/T_1$ below T_c

Next, we turn our attention to the superconducting state below T_c. Our preliminary measurements in Fig. 5.9 show that $^{59,75}(1/T_1)$ continuously decreases below T_c down to 8 K and then levels off at $\sim$ 4 K. We can gain important information on the superconducting state from the temperature dependence of $^{59,75}(1/T_1)$. First, $^{59,75}(1/T_1)$ decreases immediately below T_c without any increase, i.e., we do not observe the Hebel-Slichter coherence peak. For a conventional BCS s-wave pairing superconductor, we would expect $1/T_1$ to show a coherence peak immediately below T_c, followed by an exponential temperature dependence at low temperature due to the full opening of the isotropic energy gap far below T_c. We tried to fit $^{75}(1/T_1)$ below T_c to $exp(-\Delta/k_BT)$ by assuming that the superconducting energy gap Δ is constant below T_c (this assumption is very crude because Δ itself has temperature dependence below T_c). The best fit yields $\Delta/k_B = 42$ K, as shown by the solid line in Fig. 5.9. This number is close to what we obtained from the fit of ^{75}K below T_c in chapter 4. $\Delta \sim 2.6\ k_BT_c$, and is larger than the weak coupling BCS result of $\Delta = 1.76\ k_BT_c$. On the other hand, we can see that $^{59,75}(1/T_1)$ follows T^3 below T_c down to ~ 8 K as well, as shown by the dashed line in Fig. 5.9. Our observation of the $^{59,75}(1/T_1) \propto \mathrm{T}^3$ behavior without a coherence peak just below T_c is consistent with earlier reports on other iron-pnictides superconductors (Nakai et al., 2008, Grafe et al., 2008, Matano et al., 2008, Mukuda et al., 2008), and is qualitatively analogous to that observed for high T_c cuprates with *d*-wave pairing symmetry (Imai et al., 1988). However, we should not consider our result in Fig. 5.9 as the evidence for the presence of nodes in the superconducting order parameter. In the case of $\mathrm{YBa_2Cu_3O_{6.91}}$, Imai et al demonstrated that $^{63}(1/T_1)$ follows T^3 behavior down to $\sim$20 K ($\sim 0.2\ T_c$). Our $1/\mathrm{T}_1$ data level off below $\sim$ 10 K, which corresponds to as high as $\sim$0.5 T_c. This is typical of disorder effects in superconductors. In order to discern exponential and power-law behaviors, we need to extend $1/\mathrm{T}_1$ measurements to as low temperature as possible ($\mathrm{T} \ll T_c$) for much cleaner samples. Finally, we should mention that some theoretical models (Parker et al., 2008, Chubukov et al., 2008) proposed that the extended *s*-wave symmetry ($\mathrm{s}_\pm$) could explain the absence of a coherence peak and T^3 behavior below T_c.

5.6 Summary

In this chapter, we presented the measurements of dynamic spin susceptibility based on $^{75,59}(1/T_1T)$ for various Co concentrations. We demonstrated that doped Co continuously suppresses the SDW ordering temperature T_{SDW} and the magnitude of $^{75,59}(1/T_1T)$ in the paramagnetic state. We also demonstrated that $^{75,59}(1/T_1T)$ for slightly doped $x = 0.02$ and 0.04 samples display divergent behavior toward T_{SDW} due to the second order SDW phase transition. At the Co doping level of $x = 0.082$, the SDW ordering is completely suppressed, but the residual antiferromagnetic spin fluctuations persist and are enhanced toward the superconducting transition temperature $T_c = 22$ K. Increasing the Co doping level to the overdoped region $x = 0.099$ suppresses this residual antiferromagnetic spin fluctuations, and T_c decreases. We suggest that the antiferromagnetic spin fluctuations arise from the inter-band spin excitations between the hole and electron Fermi surfaces, and they play an important role in the superconducting mechanism of $Ba(Fe_{1-x}Co_x)_2As_2$.

Chapter 6

Conclusions

The discovery of iron-based high T_c superconductors with T_c as high as 57 K broke down the monopoly of the high T_c cuprates. The knowledge of this new family of superconductors was very limited when we started our research on this topic in the spring of 2008. After one and half year of intense studies around the world, scientists already have a much better understanding of these materials, if not the superconducting mechanism. We undertook a systematic investigation of $Ba(Fe_{1-x}Co_x)_2As_2$ (x = 0, 0.02, 0.04, 0.082, 0.099) through the measurement of ^{75}As and ^{59}Co NMR lineshapes, Knight shift, K, and spin-lattice relaxation rate, $1/T_1$, immediately after the announcement of its discovery. Our group made significant contributions to the development of the research fields as reported recently in *Physics Today* (Day, 2009). In what follows, we summarize major discoveries and solid conclusions derived from this thesis.

The ^{75}As and ^{59}Co NMR lineshapes of $Ba(Fe_{1-x}Co_x)_2As_2$ (x = 0, 0.02, 0.04 and 0.082) in the paramagnetic state are consistent with the number of different types of ^{75}As and ^{59}Co sites expected from the binomial distribution of Co dopants. To be more specific, we observed one ^{75}As site, As(0), in the undoped parent compound, and two ^{75}As sites, As(0) and As(1), for x = 0.02, 0.04 and 0.082; we observed only one ^{59}Co site in x = 0.02 and 0.04, but at least three in x = 0.082.

Below T_{SDW}, the ^{75}As line splits into two sets due to discrete values of hyperfine field B_{hf}^{c} = ± 1.32 Tesla for x = 0, but become broad and featureless for lightly doped x = 0.02 and 0.04, indicating that as little as 2 % Co doping transforms the commensurate SDW ordered ground state of the parent compound into a different state, most likely an incommensurate SDW ordered state, or a commensurate state with a large distribution of the hyperfine field B_{hf}. Furthermore, from the analysis of the temperature dependent width of the ^{59}Co NMR lineshape below T_{SDW} for x = 0.02 and 0.04, we found that Co doping suppresses not only the magnetic ordering temperature T_{SDW}, but also the magnitude of the ordered magnetic moments from 0.87 μ_B in x = 0 to 0.55 ± 0.1 μ_B in x = 0.02 and 0.3 ± 0.1 μ_B in x = 0.04.

From the measurement of static magnetic susceptibility of $Ba(Fe_{1-x}Co_x)_2As_2$ by the Knight shift, we demonstrated that Co doping continuously suppresses ^{75}K, and hence the spin susceptibility χ_s, although we can not completely rule out the possibilities that $^{75}K_{chem}$ and/or the hyperfine coupling constant A_{hf} change with Co doping as well. K becomes constant below ~ 100 K down to T_c for the x = 0.082 superconducting sample, and we found no evidence for induced localized moments in the vicinity of Co dopants. This finding is in remarkable contrast with the case of Zn or Ni doped high T_c cuprates, and suggests that the fundamental physics of iron-based superconductors is different from that of cuprates. Combined with the resistivity measurement, we demonstrated that the superconductivity arises from a novel, non-Fermi liquid electronic state where $\chi_s \sim$ constant and $\rho_{ab} \sim$ T. We also demonstrated that both $^{75}K_c$ and $^{75}K_{ab}$ decrease below T_c, and ruled out the p-wave superconductivity scenario.

The measurement of the dynamic spin susceptibility from that of $^{75,59}(1/T_1T)$

at ^{75}As and ^{59}Co sites for various Co concentrations indicate that Co doping progressively suppresses the magnitude of $^{75,59}(1/T_1T)$ in the paramagnetic state, and is consistent with the analogous suppression of ^{75}K. Furthermore, the temperature dependence of $^{75,59}(1/T_1T)$ and $^{75,59}K$ at both ^{75}As and ^{59}Co sites shows that $\mathrm{Ba(Fe_{1-x}Co_x)_2As_2}$ exhibits spin pseudo-gap like behavior down to $\sim$ 100 K for a broad Co concentration range. We also demonstrated that $^{75,59}(1/T_1T)$ displays divergent behavior toward T_{SDW} for lightly doped $x = 0.02$ and 0.04 samples, indicating the second order magnetic phase transition. Further Co doping completely suppresses the SDW ordered state, and superconductivity with $T_c = 22$ K is optimized at the doping level of $x = 0.082$. We observe the enhancement of residual antiferromagnetic spin fluctuations below $\sim$ 100 K in $x = 0.082$, but the enhancement is suppressed in the overdoped $x = 0.099$, and T_c decreases. We suggest that the antiferromagnetic spin fluctuations are associated with the inter-band spin excitations between the hole and electron Fermi surfaces, and they play a crucial role in the superconducting mechanism of $\mathrm{Ba(Fe_{1-x}Co_x)_2As_2}$.

References

Abragam, A. (1961). *Principle of Nuclear Magnetism.* Oxford Univeristy Press, Oxford.

Ahilan, K., Balasubramaniam, J., Ning, F., Imai, T., Sefat, A. S., Jin, R., McGuire, M. A., Sales, B. C., and Mandrus, D. (2008a). *J. Phys.: Condens. Matter*, 20, 472201.

Ahilan, K., Balasubramaniam, J., Ning, F., Imai, T., Sefat, A. S., Jin, R., McGuire, M. A., Sales, B. C., and Mandrus, D. (2009). *Phys. Rev. B.*

Ahilan, K., Ning, F., Imai, T., Sefat, A. S., Jin, R., McGuire, M. A., Sales, B. C., and Mandrus, D. (2008b). *Phys. Rev. B(R)*, 78, 100501.

Allen, P. (1989). *Physical properties of high temperature superconductors I.* World Scientific, Singapore.

Aoki, H. (2008). *arxiv: cond-mat/0811.1656.*

Ashcroft, N. W. and Mermin, N. D. (1976). *Solid State Physics.* Harcourt Brace, Fort Worth.

Baek, S.-H., Klimczuk, T., Ronning, F., Bauer, E. D., Thompson, J. D., and Curro, N. J. (2008). *Phys. Rev. B*, 78, 212509.

Bardeen, J., Cooper, L. N., and Schrieffer, J. R. (1957). *Phys. Rev.*, 108, 1175.

Barrett, S. E., Durand, D. J., Pennington, C. H., Slichter, C. P., Friedmann, T. A., Rice, J. P., and Ginsberg, D. M. (1990). *Phys. Rev. B*, 41, 6283.

Baskaran, G. (2003). *Phys. Rev. Lett.*, 91, 097003.

Bednorz, J. G. and Müller, K. A. (1986). *Z. Phys. B*, 64, 189.

Bobroff, J., MacFarlane, W. A., Alloul, H., Mendels, P., Blanchard, N., Collin, G., and Marucco, J. F. (1999). *Phys. Rev. Lett.*, 83, 4381.

Chen, X. H., Wu, T., Wu, G., Liu, R. H., Chen, H., and Fang, D. F. (2008). *Nature*, 453, 761.

Cheng, P., Shen, B., Mu, G., Zhu, X. Y., Han, F., Zeng, B., and Wen, H.-H. (2009). *Europhys. Lett.*, 85, 67003.

Cho, J. H., Borsa, F., Johonston, D. C., and Torgeson, D. R. (1992). *Phys. Rev. B*, 46, 3179.

Chou, F. C., Borsa, F., Cho, J. H., Johonston, D. C., Lascialfari, A., Torgeson, D. R., and Ziolo, J. (1993). *Phys. Rev. Lett.*, 71, 2323.

Chu, J. H., Analytis, J. G., Kucharczyk, C., and Fisher, I. R. (2009). *Phys. Rev. B*, 79, 014506.

Chubukov, A., Efremov, D., and Eremin, I. (2008). *Phys. Rev. B*, 78, 134512.

Day, C. (2009). *Physics Today*, August, 36.

de la Cruz, C., Huang, Q., Lynn, J. W., Li, J., II, W. R., Zarestky, J. L., Mook, H. A., Chen, G. F., Luo, J. L., Wang, N. L., and Dai, P. (2008). *Nature*, 453, 899.

Dong, J., Zhang, H. J., Xu, G., Li, Z., Li, G., Hu, W. Z., Wu, D., Chen, G. F., Dai, X., Luo, J. L., Fang, Z., and Wang, N. L. (2008). *Euro. Phys. Lett.*, 83, 27006.

Freeman, A. J. and Watson, R. E. (1965). *Hyperfine Interaction in magnetic Materials, Magnetism IIA.* Edited by G. T. Rado and S. Suhl Academic, New York.

Fukazawa, H., Hirayama, K., Kondo, K., Yamazaki, T., Kohori, Y., Takeshita, N., Miyazawa, K., Kito, H., Eisaki, H., and Iyo, A. (2008). *J. Phys. Soc. Jpn.*, 77, 093706.

Fukushima, E. and Roeder, S. B. W. (1981). *Experimental Pulse NMR, a Nuts and Bolts Approach.* Addison-Wesley Publishing Company.

Fukuzumi, Y., Mizuhashi, K., Takenaka, K., and Uchida, S. (1996). *Phys. Rev. Lett.*, 76, 684.

Grafe, H. J., Paar, D., Lang, G., Curro, N. J., Behr, G., Werner, J., Hamann-Borrero, J., Hess, C., Leps, N., Klingeler, R., , and Buechner, B. (2008). *Phys. Rev. Lett.*, 101, 047003.

Huang, Q., Qiu, Y., Bao, W., Lynn, J. W., Green, M. A., Chen, Y., Wu, T., Wu, G., and Chen, X. (2008). *Phys. Rev. Lett.*, 101, 257003.

Hunt, A. W. (2001). *Ph.D Thesis, MIT.*

Imai, T., Ahilan, K., Ning, F., McGuire, M. A., Sefat, A. S., Jin, R., Sales, B. C., and Mandrus, D. (2008). *J. Phys. Soc. Jpn. Supplement C.*, 77, 47.

Imai, T., Ahilan, K., Ning, F., McQueen, T. M., and Cava, R. J. (2009). *Phys. Rev. Lett.*

Imai, T., Shimizu, T., Yasioka, H., Ueda, Y., and Kosuge., K. (1988). *J. Phys. Soc. Jpn.*, 57, 2280.

Imai, T., Slichter, C. P., Yoshimura, K., and Kosuge, K. (1993). *Phys. Rev. Lett.*, 70, 1002.

Ishida, K., Kitaoka, Y., Yamazoe, K., Asayama, K., and Yamada, Y. (1996). *Phys. Rev. Lett.*, 76, 531.

Ishida, K., Yoshida, K., Mito, T., Tokunaga, Y., Kitaoka, Y., Asayama, K., Nakayama, Y., Shimoyama, J., and Kishio, K. (1998). *Phys. Rev. B*, 58, R5960.

Jaccarino, V. (1966). *Proc. of Int. School of Physics, Enrico Fermi*, volume 37. Academic Press.

Jesche, A., Caroca-Canales, N., Rosner, H., Borrmann, H., Ormeci, A., Kasinathan, D., Kaneko, K., Klauss, H. H., Luetkens, H., Khasanov, R., Amato, A., Hoser, A., Krellner, C., and Geibel, C. (2008). *Phys. Rev. B*, 78, 180504(B).

Jishi, R. A. and Alyahyaei, H. M. (2008). *arxiv: cond-mat/0811.2716.*

Johnston, D. (1989). *Phys. Rev. Lett.*, 62, 957.

Julien, M.-H., Mayaffre, H., Horvatic, M., Berthier, C., Zhang, X. D., Wu, W., Chen, G. F., Wang, N. L., and Luo, J. L. (2009). *Euro. Phys. Lett.*, 87, 37001.

Kamihara, Y., Watanabe, T., Hirano, M., and Hosonno, H. (2008). *J. Am. Chem. Soc.*, 130, 3296.

Kano, M., Kohama, Y., Graf, D., Balakirev, F. F., Sefat, A. S., McGuire, M. A., Sales, B. C., Mandrus, D., and Tozer, S. W. (2009). *arxiv: cond-mat/0904.1418.*

Kitagawa, K., Katayama, N., Ohgushi, K., Yoshida, M., and Takigawa, M. (2008). *J. Phys. Soc. Jpn.*, 77, 114709.

Korringa, J. (1950). *Physica*, 16, 601.

Laplace, Y., Bobroff, J., Rullier-Albenque, F., Colson, D., and Forget, A. (2009). *arxiv: cond-mat/0906.2125.*

Lester, C., Chu, J.-H., Analytis, J. G., Capelli, S., Erickson, A. S., Condron, C. L., Toney, M. F., Fisher, I. R., and Hayden, S. M. (2009). *Phys. Rev. B*, 79, 144523.

Liu, C., Kondo, T., Ni, N., Palczewski, A. D., Bostwick, A., Samolyuk, G. D., Khasanov, R., Shi, M., Rotenberg, E., Budko, S. L., Canfield, P. C., and Kaminski, A. (2009a). *Phys. Rev. Lett.*, 102, 167004.

Liu, G. D., Liu, H. Y., Zhao, L., Zhang, W. T., Jia, X. W., Meng, J. Q., Dong, X. L., Chen, G. F., Wang, G. L., Zhou, Y., Zhu, Y., Wang, X. Y., Xu, Z. Y., Chen, C. T., and Zhou, X. J. (2009b). *arxiv: cond-mat/0904.0677.*

Luetkens, H., Klauss, H.-H., Kraken, M., Litterst, F. J., Dellmann, T., Klingeler, R., Hess, C., Khasanov, R., Amato, A., Baines, C., Hamann-Borrero, J., Leps, N., Kondrat, A., Behr, G., Werner, J., and Buechner, B. (2009). *Nature Materials*, 8, 305.

Ma, F., Lu, Z. Y., and Xiang, T. (2008). *arxiv: cond-mat/0806.3526.*

Maeno, Y., Hashimoto, H., Yoshida, K., Nishizaki, S., Fujita, T., Bednorz, J. G., and Lichtenberg, F. (1994). *Nature*, 372, 532.

Malaeb, W., Yoshida, T., Fujimori, A., Kubota, M., Ono, K., Kihou, K., Shirage, P. M., Kito, H., Iyo, A., Eisaki, H., Nakajima, Y., Tamegai, T., and Arita, R. (2009). *arxiv: cond-mat/0906.1846.*

Matano, K., Ren, Z. A., Dong, X. L., Sun, L. L., Zhao, Z. X., and q. Zheng., G. (2008). *Europhys. Lett.*, 83, 57001.

Mila, F., Poiblanc, D., and Bruder, C. (1991). *Phys. Rev. B*, 43, 7891.

Millis, A. J., Hartmut, M., and Pines, D. (1990). *Phys. Rev. B*, 42, 167.

Moriya, T. (1963). *J. Phys. Soc. Jpn.*, 18, 516.

Mukuda, H., Terasaki, N., Kinouchi, H., Yashima, M., Kitaoka, Y., Suzuki, S., Miyasaka, S., Tajima, S., Miyazawa, K., Shirage, P., Kito, H., Eisaki, H., and Iyo, A. (2008). *J. Phys. Soc. Jpn.*, 77, 093704.

Nagamatsu, J., Nakagawa, N., Muranaka, T., Zenitani, Y., and Akimitsu, J. (2001). *Nature*, 410, 63.

Nakai, Y., Ishida, K., Kamihara, Y., Hirano, M., and Hosono, H. (2008). *J. Phys. Soc. Jpn.*, 77, 073701.

Nekrasov, I. A., Pchelkina, Z. V., and Sadovskii, M. V. (2008). *JETP Letters*, 88, 144.

Ni, N., Tillman, M. E., Yan, J.-Q., Kracher, A., Hannahs, S. T., Bud'ko, S. L., and Canfield, P. C. (2008). *Phys. Rev. B*, 78, 214515.

Ning, F., Ahilan, K., Imai, T., Sefat, A. S., Jin, R., McGuire, M. A., Sales, B. C., and Mandrus, D. (2008). *J. Phys. Soc. Jpn.*, 77, 103705.

Ning, F., Ahilan, K., Imai, T., Sefat, A. S., Jin, R., McGuire, M. A., Sales, B. C., and Mandrus, D. (2009a). *J. Phys. Soc. Jpn.*, 78, 013711.

Ning, F., Ahilan, K., Imai, T., Sefat, A. S., Jin, R., McGuire, M. A., Sales, B. C., and Mandrus, D. (2009b). *Phys. Rev. B(R)*, 79, 140506.

Ning, F., Ahilan, K., Imai, T., Sefat, A. S., Jin, R., McGuire, M. A., Sales, B. C., and Mandrus, D. (2009c). *arxiv: cond-mat/0904.1571.*

Ning, F., Ahilan, K., Imai, T., Sefat, A. S., McGuire, M. A., Sales, B. C., Mandrus, D., Cheng, P., Shen, B., and Wen, H. H. (2009d). *arxiv: cond-mat/0907.3875.*

Ong, N. P. (1990). *Physical properties of high temperature superconductors II.* World Scientific, Singapore.

Parker, D., Dolgov, O., Korshunov, M., Golubov, A., and Mazin, I. (2008). *Phys. Rev. B*, 78, 134524.

Pratt, D. K., Tian, W., Kreyssig, A., Zarestky, J. L., Nandi, S., Ni, N., Bud'ko, S. L., Canfield, P. C., Goldman, A. I., and McQueeney, R. J. (2009). *arxiv: cond-mat/0903.2833.*

Ren, Z. A., Che, G. C., Dong, X. L., Yang, J., Lu, W., Yi, W., Shen, X. L., Li, Z. C., Sun, L. L., Zhou, F., and Zhao, Z. X. (2008a). *Europhys. Lett.*, 83, 17002.

Ren, Z. A., Lu, W., Yang, J., Yi, W., Shen, X. L., Li, Z. C., Che, G. C., Dong, X. L., Sun, L. L., Zhou, F., and Zhao, Z. X. (2008b). *Chin. Phys. Lett.*, 25, 2215.

Ren, Z. A., Yang, J., Lu, W., Yi, W., Che, G. C., Dong, X. L., Sun, L. L., and Zhao, Z. X. (2008c). *Materials Research Innovations*, 12, 105.

Rotter, M., Tegel, M., Schellenberg, I., Hermes, W., Pottgen, R., and Johrendt, D. (2008). *Phys. Rev. B(R)*, 78, 020503.

Sarrao, J. L., Morales, L. A., Thompson, J. D., Scott, B. L., Stewart, G. R., F, F. W., Rebizant, J., Boulet, P., Colineau, E., and Lander, G. H. (2002). *Nature*, 420, 297.

Sefat, A. S., Huq, A., McGuire, M. A., Jin, R. Y., Sales, B. C., and Mandrus, D. (2008a). *Phys. Rev. B*, 78, 104505.

Sefat, A. S., Jin, R. Y., McGuire, M. A., Sales, B. C., Singh, D. J., and Mandrus, D. (2008b). *Phys. Rev. Lett.*, 101, 117004.

Sekiba, Y., Sato, T., Nakayama, K., Terashima, K., Richard, P., Bowen, J. H., Ding, H., Xu, Y.-M., Li, L. J., Cao, G. H., Xu, Z.-A., and Takahashi, T. (2009). *New J. Phys.*, 11, 025020.

Shein, I. R. and Ivanovskii, A. L. (2008). *JETP LETTERS*, 88, 107.

Shirage, P. M., Miyazawa, K., Kito, H., Eisaki, H., and Iyo, A. (2008). *Phys. Rev. B*, 78, 172503.

Si, Q. M. and Abrahams, E. (2008). *Phys. Rev. Lett.*, 101, 076401.

Singer, P., Imai, T., He, T., Hayward, M. A., and Cava, R. J. (2001). *Phys. Rev. Lett.*, 87, 257601.

Singer, P. M., Hunt, A. W., and Imai, T. (2002). *Phys. Rev. Lett.*, 88, 047602.

Singer, P. M., Imai, T., Chou, F. C., Hirota, K., Takaba, M., Kakeshita, T., Eisaki, H., and Uchida, S. (2005). *Phys. Rev. B.*, 72, 014537.

Singh, D. J. (2008). *Phys. Rev. B*, 78, 094511.

Singh, D. J. and Du, M. H. (2008). *Phys. Rev. Lett.*, 100, 237003.

Slichter, C. P. (1990). *Principles of Magnetic Resonance*. Springer-Verlag, New York.

Takada, K., Sakurai, H., Takayama-Muromachi, E., Izumi, F., Dilanian, R. A., and Sasaki, T. (2003). *Nature*, 422, 53.

Takigawa, M., Hammel, P. C., Heffner, R. H., Fisk, Z., Smith, J. L., and Schwartz, R. (1989). *Phys. Rev. B*, 39, 300.

Takigawa, M., Reyes, A. P., Hammel, P. C., Thompson, J. D., Heffner, R. H., Fisk, Z., and Ott, K. C. (1991). *Phys. Rev. B*, 43, 247.

Tanatar, M. A., Ni, N., Martin, C., Gordon, R. T., Kim, H., Kogan, V. G., Samolyuk, G. D., Bud'ko, S. L., Canfield, P. C., and Prozorov, R. (2009). *Phys. Rev. B*, 79, 094507.

Terashima, K., Sekiba, Y., Bowen, J. H., Nakayama, K., Kawahara, T., Sato, T., Richard, P., Xu, Y.-M., Li, L. J., Cao, G. H., Xu, Z.-A., Ding, H., and Takahashi, T. (2008). *arxiv: cond-mat/0812.3704*.

Thurber, K. R., Hunt, A. W., Imai, T., Chou, F. C., and Lee, Y. S. (1997). *Phys. Rev. Lett.*, 79, 171.

Timusk, T. and Statt, B. W. (1999). *Rep. Prog. Phys.*, 62, 61.

Vilmercati, P., Fedorov, A., Vobornik, I., U., M., Panaccione, G., Goldoni, A., Sefat, A. S., McGuire, M. A., Sales, B. C., Jin, R., Mandrus, D., Singh, D. J., and Mannella, N. (2009). *Phys. Rev. B*, 79, 220503(R).

Wang, C., Li, L., Chi, S., Zhu, Z. W., Ren, Z., Li, Y. K., Wang, Y. T., Lin, X., Luo, Y. K., Jiang, S., Xu, X. F., Cao, G. H., and Xu, Z. A. (2008). *Europhys. Lett.*, 83, 67006.

Wang, X. F., Wu, T., Chen, H., Xie, Y. L., Ying, J. J., Liu, Y. J. Y. R. H., and Chen, X. H. (2009a). *Phys. Rev. Lett.*, 102, 117005.

Wang, X. F., Wu, T., Wu, G., Liu, R. H., Chen, H., Xie, Y. L., and Chen, X. H. (2009b). *New J. Phys.*, 11, 045003.

White, R. M. (1970). *Quantum Theory of Magnetism.* McGraw-Hill, New York.

Yang, L. X., Zhang, Y., Ou, H. W., Zhao, J. F., Shen, D. W., Zhou, B., Wei, J., Chen, F., Xu, M., He, C., Chen, Y., Wang, Z. D., Wang, X. F., Wu, T., Wu, G., Chen, X. H., Arita, M., Shimada, K., Taniguchi, M., Lu, Z. Y., Xiang, T., and Feng, D. L. (2009). *Phys. Rev. Lett.*, 102, 107002.

Yannoni, C. S., Johnson, R. D., Meijer, G., Bethune, D. S., and Salem, J. R. (1991). *J. Phys. Chem.*, 95, 9.

Yi, M., Lu, D. H., Analytis, J. G., Chu, J.-H., Mo, S.-K., He, R.-H., Zhou, X. J., Chen, G. F., Luo, J. L., Wang, N. L., Hussain, Z., Singh, D. J., Fisher, I. R., and Shen, Z.-X. (2009). *Phys. Rev. B*, 80, 024515.

Yildirim, T. (2008). *Phys. Rev. Letts.*, 101, 057010.

Yin, Y., Zech, M., Williams, T. L., Wang, X. F., Wu, G., Chen, X. H., and Hoffman, J. E. (2009). *Phys. Rev. Lett.*, 102, 097002.

Yosida, K. (1958). *Phys. Rev.*, 110, 769.

Zhang, G. M., Su, Y. H., Lu, Z. Y., Weng, Z. Y., Lee, D. H., and Xiang, T. (2009). *Europhys. Lett.*, 86, 37006.